THE UNIVERSITY OF CHICAGO

FIRST PRINCIPLES STUDIES OF AQUEOUS SYSTEMS AT AMBIENT AND EXTREME CONDITIONS

A DISSERTATION SUBMITTED TO
THE FACULTY OF THE PRITZKER SCHOOL OF MOLECULAR ENGINEERING
IN CANDIDACY FOR THE DEGREE OF
DOCTOR OF PHILOSOPHY

BY
VIKTOR FERENC ROZSA

CHICAGO, ILLINOIS
AUGUST 2020

To my parents, Frank and Szonja

"And the earth was without form, and void; and darkness was upon the face of the deep. And the Spirit of God moved upon the face of the waters."

Genesis 1:2

TABLE OF CONTENTS

LIST OF FIGURES

LIST OF TABLES

ACKNOWLEDGMENTS

Firstly, I thank my advisor, Prof. Giulia Galli for her support over the past years. I am indebted to Giulia's scientific mentorship as well as her personal support of me over several new phases of life during these years. I thank her for leading of an incredible research group and for all the exceptional resources and opportunities that she has made available to me during my time in the group.

I also thank several other mentors that helped guide and mentor me in my research. Thanks to Prof. Ding Pan for showing me the ropes with simulations and for fostering my interest in materials at extreme conditions. Thanks to Dr. Federico Giberti whose creativity and optimism helped me through numerous challenges along the way. Finally, thanks to Dr. Anh Pham for his mentorship and hospitality to me during my research practicum at Lawrence Livermore National Laboratory, and afterwards. I am deeply indebted to his kindness and assistance to me in charting the waters of nanoconfinement, while also offering advice on the day-to-day practice of research.

I would like to thank Prof. Francois Gygi, Dr. Alex Gaiduk, and Dr. Quan Wan for fruitful collaboration and discussions we had together. I also thank the entire Galli group for their help and encouragement at all levels along the way. I especially thank Arin Greenwood for all the companionship and encouragement in navigating grad school start to finish.

I thank my parents, Frank and Szonja for their steady love and support for me during these years. You have both motivated and believed in me from my earliest education to the completion of this thesis in your home under strange times. Thank you for your hospitality, humor, and love. I dedicate this thesis to you.

I thank my son, János, for the light and joy he has brought into our lives. Many a long day or night has been brightened by your dear laugh and twinkling eye. Lastly, I thank my wife, Hannah, for her unfailing love, encouragement, and prayers for me over these years. As has other times been the case, words fail me to sum up my gratitude for you.

ABSTRACT

Water is the quintessential hydrogen-bonded system, exhibiting exotic and anomalous properties with application in fields varying from biophysics to planetary science to molecular engineering for energy technologies. In this dissertation, we examine aqueous solutions of solvated ions in bulk water and "extreme conditions" corresponding to nanoconfinement and elevated pressure/temperature. We apply first principles molecular dynamics simulations based on density functional theory to analyze in detail both structural alterations to water at these conditions as well as more subtle and intrinsically quantum mechanical quantities, including Raman and infrared spectra, ionic conductivity, and molecular polarizabilities.

Understanding how water is modified by the presence of ions is crucial to the solvation properties involved in biophysical processes as well as a range of energy applications, for example photoelectrochemical cells. While the effect of ions on nearby water molecules is relatively well understood, alterations to water beyond the first solvation shell due to ion presence remains controversial, with disagreement in both computational and experimental literature. We present a systematic first-principles molecular dynamics study of alkali cations in water (Li^+, Na^+ and K^+). Our use of statistically robust sampling of trajectories allows constraint of error bars on several critical structural and dielectric properties. Our simulations support the view that the water structure is only modified locally by the presence of cations. We found that molecular polarizabilities are fingerprints of hydrogen bonding modifications, which occur at most up to the second solvation shell for all cations in bulk water. In addition, we apply our simulations of solvated K^+ to isotopic fractionation of potassium, finding that equilibrium fractionation between aqueous K^+ and K-bearing clay minerals is insufficient to explain the observed K heavy isotope enrichment in seawater or river waters.

Perturbations to aqueous solutions by confining media have been the focus of numerous studies, finding application in a wide range of green technologies. Yet several open questions remain, including the extent to which nanoconfinement modifies the structural and dielectric

properties of water, and what the additional effect of solvated ions is at these conditions. In this thesis we carried out a first-principles molecular dynamics study of pure water and LiCl and KCl solutions under confinement within carbon nanotubes (CNT) of small diameter (1.1-1.5 nm). Under confinement we found that the overall value of the molecular polarizability of water molecules near the surface is determined by the balance of two effects, that are quantitatively different in CNT of different radii: the presence of broken hydrogen bonds at the surface leads to a decrease of the polarizabilities of water molecules, while the interaction with the CNT enhances polarizabilities. Interestingly the reductions of dipole moments of interfacial water molecules under confinement is instead driven only by changes in the water structure and not by interfacial interactions. As expected, confinement effects on water molecular polarizabilities and dipole moments are more pronounced in the case of the 1.1 nm CNT.

The phase diagram of water at extreme conditions plays a critical role in earth and planetary science, yet remains poorly understood. We carried out a first principles investigation of the water at high temperature, between 11 and 20 GPa - a region where numerous controversial results have been reported over the past three decades. Our results are consistent with the recent estimates of the water melting line below 1000 K, and show that on the 1000 K isotherm the liquid is rapidly dissociating and recombining through a bi-molecular mechanism. We found that short-lived ionic species act as charge carriers giving rise to an ionic conductivity that at 11 and 20 GPa is six and seven orders of magnitude larger, respectively, than at ambient conditions. Conductivity calculations were performed entirely from first principles, with no a-priori assumptions on the nature of charge carriers. Despite frequent dissociative events, we observed that hydrogen bonding persists at high pressure, up to at least 20 GPa. Our computed Raman spectra, which are in excellent agreement with experiment, show no distinctive signatures of the hydronium and hydroxide ions present in our simulations. Instead, we found that infrared spectra are sensitive probes of molecular dissociation, exhibiting a broad band below the OH stretching mode ascribable to vibrations

of complex ions.

Given that most real geochemical fluids are mixtures of water and various impurities, we also studied the properties of ion solvation at high pressure and temperature. We employ first principles molecular dynamics to study the structure, diffusion, and vibrational properties of the solutions. We find that the solvation of ions at these conditions brings no new vibrational signatures in Raman and infrared spectra of the liquid despite considerable changes to solvation shells. We also compute the changes induced by ions to the dielectric constant of the liquid water, and find that pure water is an upper bound on the dielectric constant of the solutions. We compute the ionic conductivity at the same conditions, finding that there is a moderate increase in the conductivity of water due to the ions, despite no significant changes to global molecular dissociation. Furthermore, we employed state-of-the-art molecular cluster recognition patterning, and found no significant differences among various solutions with monovalent ions at these conditions. Our results indicate that the effect of monovalent ions over a broad range of size on the structure of water at these conditions is minimal. Dissociative water is remarkably resilient to the effect of ions solvation, even at relatively high concentrations.

CHAPTER 1

INTRODUCTION

1.1 Aims

Water is the essential building block of life, a key constituent of planetary interiors, and a crucial component of numerous energy technologies. Though it may appear simple on first glance as a ubiquitous binary compound, water is in no way typical. Its properties continue to surprise and confound across a range of disciplines. The quest to understand water has been a primary motivator and benchmark of numerous experimental apparatuses as well as theoretical and algorithmic methods [202, 95]. The hallmark of water is the intermolecular hydrogen bond. Hydrogen bonding in water leads to a local tetrahedrality in water molecules, and is believed to be fundamentally connected to most of water's anomalous and exceptional properties.

Water exhibits physical anomalies including unusually high viscosity and surface tension. It exhibits exceptional phase anomalies, being the most abundant substance on Earth and only material commonly found in solid, liquid, and gaseous phases. It exists in a broad variety of both crystalline and amorphous structures, with 18 known crystalline phases. Water has unusually high melting, boiling, and critical points. It exhibits numerous anomalies in its density. Gaseous water is extremely light, while liquid water is denser than expected, and solid water is less dense than the liquid. Many ecological and oceanographic processes are a result of ice's low density combined with water's density maximum, with contraction upon heating ice, and expansion on freezing water. Both the dielectric constant of water and its specific heat capacity are exceptionally high. There is a growing consensus that many low-temperature anomalies in water may be attributed to a highly unusual liquid-liquid critical point [59]. Several reviews have been written specifically to document water's unusual properties [12, 31].

While the characteristics even of pure water near ambient conditions are so anomalous

as to require active research, altering the chemical environment of water through ion solvation, confinement, or elevated pressure and temperature further complicates the properties of water. For decades, there has been debate about the effect of ions on the properties of water. Both experimental and computational studies have differed on whether ions have long or short range effect on the properties of water, as well as which quantities may manifest such effects [165, 108]. The large-scale disruption of water structure is much more certain in the case of nanoconfined water, where the hydrogen bond network of water is restrained by the "extreme condition" of physical confinement. While many recent studies have begun to describe the significant consequences of nanoconfinement, including novel exotic phases, alterations to diffusive properties, and anisotropies in dielectric properties, a comprehensive understanding of confined water is still lacking [42]. The combination of ion solvation and nanoconfinement is even less well understood, despite being crucial to the molecular engineering of technologies ranging from water desalination to supercapacitors [72, 254]. Finally, the effect of thermodynamic extreme conditions on the properties of water are still poorly understood. Water under pressure has critical roles in planetary physics. From a terrestrial viewpoint, ice VII is understood to exist in cold subducting tectonic slabs, bearing large reservoirs of water into the mantle, with immense impact geochemistry [24]. Recent studies have further developed our understanding of deep water in verifying stable hydrous minerals in the deep earth [182]. Of particular importance is the geochemical transport of dissolved carbon, with water as a transport medium [128]. The presence of water at extreme conditions is also crucial to understanding geochemistry and magnetic fields of other planets [117] [37]. Similar to the case of nanoconfinement, the understanding of the effect of ions on water at extreme thermodynamic conditions is particularly lacking, though it is crucial to any modeling of real geochemical systems.

Each of these perturbations to pure water at ambient pressure and temperature comes with its own unique challenges from an experimental point of view. Ion solvation in water is a complicated phenomenon that must be characterized to capture both the sensitive lo-

cal perturbations and potentially longer ranging effect. Nanoconfined systems raise obvious experimental challenges to *in situ* examination of water due to the presence of a confining barrier. At extreme thermodynamic conditions, experiments are very challenging due the difficulty of experiments capable of reaching both high pressure and temperature. Furthermore, at these conditions, aqueous solutions are highly corrosive and react harmfully with experimental apparatuses. The combination of the complicated behavior of water at these conditions and the difficulties of probing it naturally lends motivation to take up computer simulations, where many of the experimental difficulties may be overcome.

While an abundance of work has been performed to address these problems using classical simulations, the nature of sensitive changes to the electronic properties of water, complicated interfacial physics, and dissociative molecular properties all benefit from the use of first principles simulations, which is built up from fundamental quantum mechanical laws. In this thesis, we approach all of these problems with the tools of first principles simulations. While ion solvation, nanoconfinement, and thermodynamic extremes are very physically distinct scenarios, all are fundamentally connected to the question of how alterations to the hydrogen bond network of water affect the properties of water. The purpose of this thesis is to employ first principles simulations to understand the effects of these conditions and even draw comparisons across such various chemical and thermodynamic environments.

1.2 Structure of Thesis

• Chapter 2 presents an overview of the state of the art in understanding of water at the conditions explored in this thesis. It explores first the understanding of pure water at ambient conditions, with summaries of the current challenges both in experimental and computational approaches. The chapter will also explain broadly the strategies towards modelling the atomic interactions of water both from classical simulations and first-principles models. It will also summarize the current understanding and challenges in solvation of ions in water, water under nanoconfinement, and water at extreme thermodynamic conditions. The chapter

will motivate the necessity of first principles modeling to fully understand water at these extreme conditions.

• Chapter 3 presents the theoretical background on which this thesis rests. It introduces density functional theory and first-principles molecular dynamics, in addition to the various choices of approximation that are made in the theoretical framework. This chapter also includes theoretical background on various computational tools deployed in the paper, including calculation of Raman and Infrared spectra, molecular polarizabilities, and ionic conductivity.

• Chapter 4 presents the application of first-principles molecular dynamics simulations to study structural and dynamical properties of ambient water at ambient conditions with the solvation of various monovalent (Li^+, K^+, Cl^-) ions. In particular, we investigate the effect of ion solvation and hydrogen bonding. The chapter presents the effect of ion solvation on dielectric properties of water, including the dipole moment and molecular polarizabilities. The chapter also includes the application of the simulations of aqueous K^+ solution to the study of isotopic fractionation.

• Chapter 5 turns from the examination of ions in bulk water to study the effects of nanoconfinement. Water is studied under confinement at two carbon nanotube diameters (1.1 and 1.5 nm). In addition, the chapter also presents analysis on the effect of ion solvation combined with confinement in the 1.1 nm nanotube geometry. The effect of confinement and ion solvation under confinement is analyzed in terms of structure as well as dielectric properties and band gaps. Comparisons are made to the groundwork established in Chapter 4 for ion solutions in bulk water.

• Chapter 6 is devoted to the properties of pure water at extreme thermodynamic conditions. We present an analysis of structure and diffusion to characterize water behavior in three crucial and controversial areas of water's phase diagram corresponding to molecular liquid, ionic liquid, and quenched/amorphous solid phases. We compute vibrational spectra, including Raman and infrared spectra, of water at these conditions, and compare our first-

principles results to experimental data. Finally, we compute the ionic conductivity of water at these conditions using a fully first-principles method, and use our results to explain the molecular origins of experimentally measured conductivity increases.

• Chapter 7 presents an extension of the work on pure water to study the effects of ion solvation (Li^+, K^+, Cl^-, NaCl) on water at high pressure and temperature. Here we present detailed analysis of alterations of solvation shell properties due to high pressure/tempareture. We analyze the effects of ion solvation on dipole moments and molecular polarizability. In this chapter we also present results on the modifications to both the ionic conductivity and the dielectric constant of water due to ion solvation. We also compute free energies to further characterize the effect of ions on water at these conditions.

Finally the work is summarized in the Conclusion chapter, which also includes perspective on future work.

CHAPTER 2

STATE OF THE ART IN UNDERSTANDING WATER

2.1 Introduction

In this chapter, we present a broad overview of the understanding of water at the conditions relevant to this work. This chapter will include both experimental and computational results, with a focus on the understanding of the physics of water itself. We leave deeper discussions of simulation theory to the Chapter 3.

In section 2.2, we focus on the understanding of water at ambient conditions, with both pure water and simple solutions. We discuss the controversy in discerning the local vs. global properties of ion effects on water. In section 2.3, we describe water under nanoconfinement, and survey the current understanding. Finally, in section 2.4 we discuss aqueous solutions at extreme thermodynamic conditions.

2.2 Water at ambient conditions

We begin by introducing the current understanding of water at ambient conditions, including both pure water and simple aqueous ion solutions.

2.2.1 Pure water

Water is the essential to vast amounts of biological, geological, and technological processes. While in each of these processes water interacts with solutes and interfaces, the basis for studying these more complicated scenarios begins with an understanding of pure water. At stake in the study of pure water is the very broad question of how molecular structure affects macroscopic properties. Pure water exhibits many peculiar macroscopic properties, as has already been described. These include "universal solvent" characteristic, high surface tension, high boiling/melting points, high viscosity, increased density upon melting, decreased

viscosity under pressure, and a density maximum at 4°C, to name a few [30]. Most of the anomalous properties of water find their origin in the properties of hydrogen bonding in water.

The hydrogen bond is an attractive intermolecular interaction in which an electropositive hydrogen atom resides between two electronegative species (oxygen atoms, in the case of water), bringing them closer together. The hydrogen bond in water is a weak bond, being limited to roughly one twentieth the strength of the covalent O-H bond. Nevertheless, it persists with a lifetime of roughly 1 ps at ambient conditions despite thermal fluctuations of the liquid. On this timescale, hydrogen bonds of the liquid are constantly breaking and reforming according to the orientations of individual water molecules. The connection between this fluctuating hydrogen bond network and the extraordinary properties water at ambient conditions has been an active area of research for many years [136, 256]. However, to begin to unravel the macroscopic properties of the hydrogen-bonded liquid, we must begin at the molecular scale. The most fundamental understanding of the water molecule is quantum mechanical. An H_2O molecule may be understood by solving the Schrodinger equation for its 10 constituent electrons, which results in the covalent bonding of two hydrogen atoms and one oxygen atom. The molecular orbitals are sp^3 hybridized, leading to a tetrahedral structure with two bond pairs and two lone pairs [30]. The hallmark hydrogen bonds of the liquid phase form between positively charged hydrogen atoms, and the lone pair electrons of acceptor oxygen atoms.

Despite the conceptual simplicity, the understanding of the hydrogen bond, and even basic questions of water structure are still debated [202]. Recently, experimental methods including X-ray absorption and emission spectroscopy have challenged the view of water as a simple tetrahedral liquid [282, 269]. Such conclusions were disputed by various experimental studies [247, 210, 82] and several first principles studies have also weighed in on the interpretation [207, 190]. Additional experimental work in pure water is being driven by breakthroughs in neutron scattering and wide-angle X-ray diffraction, which now are able to shed light on

structure at the level of density inhomogeneity and fluctuations [246]. Furthermore, new methods in ultrafast nonlinear vibrational spectroscopy have pointed to interesting results that hydrogen bonding with OD are stronger than hydrogen bonding with OH [152], casting some uncertainty on studies that use isotopic substitution in water.

Major challenges lie in unambiguously characterizing atomic-scale fluctuations in water. Current experimental approaches such as time-resolved spectroscopy and diffraction measurements may be able to resolve picosecond scale changes, but often rely on interpretation through models that often cannot describe many details of liquid water with quantitative accuracy [47]. Thus there is still great need for development and synergy between experimental and computational studies on even basic properties of water.

2.2.2 Simple Aqueous Solutions

While the behavior of pure water is complex and controversial in its own right, the addition of solutes to water leads to further puzzles. We here examine the addition of simple ions or salts to water, which has been an active areas of research for decades [165, 108]. However, the effect of perturbations due to ions on the structure and electronic properties of water is not yet fully understood. While there is more agreement on the way that ions modify the structure of water within the first solvation shell of ions, the effect of ions outside the first solvation shell is more controversial [245, 197]. Here too, experiment has made great strides in deploying tools useful for characterizing such changes, including photoelectron spectroscopy, X-ray absorption spectroscopy, X-ray emission spectroscopy, resonant inelastic X-ray scattering, and X-ray Raman scattering [202, 240, 233]. Yet an unified understanding of water properties in ion solutions is still lacking, both from experimental and computational points of view.

Recently, several experiments concluded, contrary to previous studies [101, 138, 186, 165], that the effect of dissolved salts on the structure of water is rather weak, possibly just confined to the first solvation shells. For example, a femtosecond infrared (fs-IR) spectroscopy

study [188] established that the rotational dynamics of water molecules outside the first solvation shells of ions was unchanged compared to that of bulk water. These conclusions were supported by X-ray absorption spectroscopy and Raman scattering studies [181, 126] that found only local effect of ions even despite very high ion concentrations. These conclusions were bolstered by molecular dynamics simulations [248] that explained the changes of to the Raman spectra by a direct interaction of water molecules with ions that excluded long-range effects.

On the other hand, a recent terahertz dielectric relaxation study coupled to fs-IR spectroscopy, showed that in some cases, long-range effects of ions on water structure were present, due to cooperativity in ion solvation [267]. Specifically, they observed a slow down of the reorientational dynamics of the solvent in aqueous Na_2SO_4 and $MgSO_4$ solutions, arising due to locking of water molecules between the ions. These results were disputed by molecular dynamics studies by analyzing water reorientational dynamics [253]. They established that slowing down of water dynamics occurs in concentrated solutions regardless of the nature of the salt, although their findings failed to explain dielectric spectroscopy results [267]. Supporting these results, dielectric relaxation studies by Kondoh et al. [137] suggested that even monovalent salts may have an effect beyond the first solvation shell, based on analysis of fast-relaxation contribution to the dielectric spectrum. In particular, they found that cations, including Li^+, Na^+, and K^+, induced faster dynamics on water molecules outside the first solvation shell.

The dielectric relaxation studies [137] were consistent with the neutron diffraction studies by Soper and co-workers [249, 160, 161] on NaCl and KCl, who suggested that the effect of ions on water resembles that of applied pressure and extends well outside the first solvation shell. O'Brien et al. [189] arrived at a similar conclusion by analyzing the infrared photodissociation spectra of a series of ions in gas-phase water clusters. Finally, recent measurements of femtosecond elastic second harmonic scattering intensities from pure water and solutions of salts by Chen et. al [48] have shown that ions affect the orientational correlation of water

molecules in the range of > 5 nm even at micromolar concentrations.

Unfortunately, similar to experiments, computer simulations do not provide a fully consistent picture of the structure of solutions of salts. For example, simulations of Chandrasekhar and Jorgensen [43] found an increase in the number of hydrogen bonds in the second solvation shell of Na^+ but reverted the conclusion after revision of the empirical potential representing ion-water interactions [44]. Kim et al. [131, 130] determined that CsI salt slows down the diffusion of water molecules compared to pure water, hence drawing conclusions opposite to experiments [180]. These results were confirmed for several water models including polarizable SWM4-DP [143] and AMOEBA [219]. However, Kann and Skinner [127] argued that the empirical potential for ions adopted by Kim et al. is incorrect and proposed a simple force field which yields a diffusion coefficient in agreement with experiments [180]. Ding et al.[63] took a different approach, using ab initio molecular dynamics, and determined that simulations with the revPBE functional correctly predict faster diffusion of water in CsI solutions compared to pure water, although the numerical accuracy of diffusion coefficients determined with limited simulation data remains to be addressed. In Ref. [63], no change of the structure of water was reported, a result based on the analysis of dipole moments of water molecules, in agreement with that of Boero and co-workers [231, 123]. White et al. [283] arrived at a similar conclusion based on the analysis of hydrogen bonding and structure of water outside the first solvation shell of Na^+. A recent first-principles study by Gaiduk et al. [85], based on statistically robust molecular dynamics trajectories of NaCl solutions, found that while Cl^- anions have weak structure-breaking effects beyond the second solvation shell of water, the Na^+ cation has negligible structure-making effects beyond the first shell.

2.3 Water under nanoconfinement

While the extent of the perturbation of ions on water structure is controversial, there is little doubt that the nanoconfinement of water has significant disruption on the structure

of water. Given that water may be confined by geometries so small as to only fit a single water molecule, we may rightly regard nanoconfinement as a type of "extreme condition" on the properties of water. Here we deal primarily with phenomena of water in cylindrical confinement. Cylindrical confinement is generally interesting, as it is an ideal model system for the properties of inhomogeneous water in biological, geological, and even nanostructures designed and synthesized through molecular engineering [260]. The prototypical cylindrical confining medium is the carbon nanotube (CNT), first reported by Iijima in 1991 [120], which exhibit walls composed of a hexagonal lattice of carbon atoms and diameters ranging from less than one nanometer to several micrometers in length. Despite a certain degree of hydrophobicity of CNTs, it has been well established that CNTs spontaneously fill with water, and allow for uninterrupted flow [159, 71].

Many interesting and unusual behaviours of water have been reported under confinement, including enhanced diffusion[159, 14], elevated proton conductivity[163], the formation of one-dimensional water chains [278], square ice phases [133, 46], and diameter-dependent elevated phase transition temperatures [260, 214, 2]. Several recent studies of confined water have found anomalous and anisotropic dielectric properties [292, 289, 212, 220, 230, 83, 178]. The remarkable properties of confined water have led to proposals for using CNTs in water filtration and desalination technologies, as single molecule sensors, supercapacitors, and model biological systems [254, 42]. While many classical simulations have been employed [211, 109, 178] to better understand such phenomena, first-principles simulations of water confined at the nanoscale are still relatively rare [49, 278, 140, 241]. In particular, the effect of confinement on the molecular polarizability of water remains an open question, and it is crucial to understanding the behaviour of water at surfaces [284, 34, 134, 179].

Additionally, very few studies exist at the first principles level of theory that combine nanonconfinement of water with ion effects [204, 72]. Under nanoconfinement, the distinction between ion solvation shells and the rest of the fluid may become uncertain, increasing the likelihood of strong electro-osmotic and diffusio-osmotic coupling effects, which can become

dominant in narrow confinement geometries [28, 162]. Confined ion solvation properties are also crucial to engineering ion selectivity in nanofluidic devices [226, 227].

2.4 Water at High Pressure and Temperature

While nanoconfinement may be regarded as an extreme condition due to its distortion of water from bulk structure by means of physical confinement, the elevation of pressure and temperature (P=10-20 GPa, T=1000 K) also constitutes an extreme condition applied to bulk water. In such extreme thermodynamic conditions, liquid water exhibits significant molecular dissociation, the properties of which are still being understood. Furthermore, high temperatures and pressures transform water into a plethora of different phases that vary significantly in state, proton ordering, crystal structure, conductivity, and density. Establishing the phase diagram of water at extreme conditions and understanding its fundamental physics is essential to answering fundamental questions about our planet and other geophysical systems. Resolving these large gaps in our understanding of the phase diagram will determine if and how pure and mixed water may exist in reservoirs in our own planet as well as others. These questions directly impact our understanding of planetary formation, magnetic fields, volcanic activity, and the global carbon cycel.

Water under pressure has a critical role in planetary physics. From a terrestrial viewpoint, high pressure ice is thought to exist in cold, subducting tectonic slabs, bearing large reservoirs of water with immense impact on fields from geochemical transport of materials to seismicity and vulcanism [24]. Recent studies have further developed our understanding of deep water in verifying stable hydrous silicate minerals in the deep earth [182]. Of particular importance is the geochemical transport of dissolved carbon, with water as a transport medium [128]. Thus deep water and its properties have large effect on the global water and carbon cycles, critical for accurate climate modelling. The presence of water at extreme conditions is also crucial to understanding the planetary physics and consequent origin of strong magnetic fields of other planets such as Saturn, Uranus, and Neptune [117, 37]. On a more fundamental

level, studying water at high pressure and temperature amounts to studying the effect of extreme thermodynamics conditions on the quintessential hydrogen bonded system.

High pressure/temperature (P/T) conditions are extremely difficult to achieve experimentally, and even more so with water. Protons are too small to be probed with the usual tool of x-ray diffraction and neutron scattering has only very recently been developed to useful form at these conditions [102]. Most current understanding of water's phase diagram comes from a number of both static and shock high-pressure experimental studies focusing on various vibrational spectroscopies, conductivity measurements and a few classical simulations. Given the experimental challenges and theoretical shortcomings of classical simulations, ab initio simulations are a uniquely effective tool to study the many puzzles of high P/T water.

The phase diagram of water is both complicated and controversial. Melting lines of the ice VII phase differ by more than 600 K and several gigapascals between different experimental methods. "Plastic ice" phases have very recently been proposed in regions of the phase diagram that are debated to be either liquid or solid [261, 8]. Experimentalists have defended three markedly different locations for the triple point of liquid phase, ice VII, and superionic water [68]. Fig. 2.1 is reproduced from [175], and shows the a collection of literature on the phase diagram of water in this part of phase space. All lines in the figure come from digitizations of phase boundaries as defined in the listed reports, which are described in the caption along with the method used to establish the transition.

Due to its relevance to planetary science, much effort has gone into understanding the chemical behavior of water near the melting line of ice VII as well as the location of the melting line itself. Existing experimental research has utilized Raman spectra [98, 151, 150], Brillouin spectra [4], electrical conductivity, [187], and visual observation [235, 234]. Experimental studies focusing on Raman spectra of solid ice VII and other high pressure water phases have reported inconsistent conclusions as they track anomalous Raman peak activity [286, 112]. Indeed, the analysis of *in situ* Raman spectra has been a particular challenge,

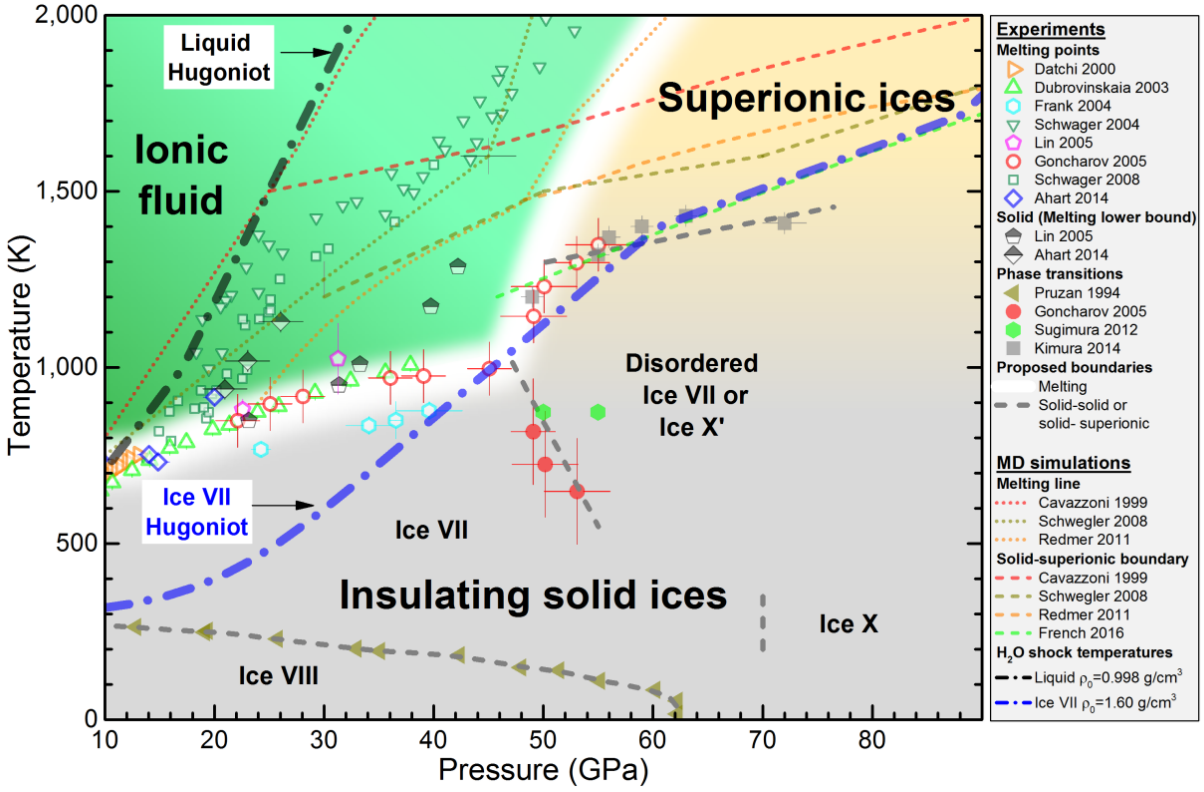

Figure 2.1: Water phase diagram near the predicted triple point between the ionic liquid, the insulating solid ice, and superionic ice; Figure reproduced from Millot. et al [175]. Static compression experiments used refractive index changes [56], x-ray diffraction [65, 74, 150], Raman spectroscopy [150, 98], Brillouin spectroscopy [4] or visual observations [235, 234] to identify melting. Ice phase boundaries from Raman spectroscopy [98, 208], x-ray diffraction [255] or laser-based calorimetry [132]. Molecular dynamics simulation predictions for melting and solid to superionic transitions [37, 238, 218, 81]. Shock-compressionstates (Hugoniot) starting with ambient liquid water lies within the ionic liquid field. Starting with ice VII allows us to reach the predicted stability domain of superionic ices at lower temperatures.

especially with the technical difficulties of laser heating and temperature gradients [99, 132]. Furthermore, within certain pressure ranges, the O-H stretching modes are obscured by Raman intensity coming from the diamond anvil apparatus itself [150].

Due to experimental challenges, there are a very limited number of experimental Raman spectra of high P/T water, even less of which are liquid phase. Pressures and temperatures in the ranges of hundreds of kelvin and several gigapascals cause disruptive reactions between gasket, water, and the metal used for laser heating. In view of the experimental challenges both in set-up and interpretation, simulations can prove vital to making sense of physics of the systems. While classical simulations, (MD simulations with empirical potentials), can certainly be powerful, they often miss out on key information only available from a full quantum treatment of electrons, available through the tools of density functional theory. The ab initio simulation studies of high P/T water so far have been few in number and ultimately inconclusive in their resolution of the experimental discrepancies [238, 237, 236]. A two-phase melting study was in close agreement with the higher melt lines, and in disagreement with the majority of Raman-based experiments [238]. A different study came in agreement with earlier experiments suggesting fluid water's change from hydrogen-bond dominated to dissociation-dominated near these conditions (P=12-30 GPa and T=600-2000 K), although it differed in dissociation mechanism [236, 114].

Applying first principles simulation to the computation of vibrational spectra is still quite rare, with just one notable study relating to water at extreme conditions, in which Raman spectra were computed from ab initio molecular dynamics for high P/T ice phases [209]. Our own studies involve longer simulations and focus on liquid phase vibrational spectra. We compute polarizabilities through density functional perturbation theory, in an implementation that has already been applied to water at ambient conditions [275]. A similar method was recently applied to ambient and supercritical water, albeit at much lower P/T conditions [121]. Our method allows the computation of valuable data that is impossible to isolate experimentally, such as intermolecular vs. intramolecular contributions

to spectra. Given that these molecular interactions may have cancelling effects, crucial information may be lost in one-shot experimental Raman spectra. Such decompositions are key to understanding the very vibrational modes whose interpretation causes discrepancies among experiments on the phase diagram.

2.5 Water at Thermodynamic Extremes with Ions

The properties of pure water at extreme thermodynamic conditions continue to be elusive, and the situation may be further complicated with the addition of solutes to water. Such mixed solutions at thermodynamic extremes are interesting firstly from a fundamental point of view. As discussed earlier, there exist significant controversies in the understanding of aqueous ion solutions even at ambient conditions. The effect of high pressure and temperature may significantly change the answers to the basic questions of local vs global effects due to ions, or which computable/measurable quantities might be fingerprints of ion effects. Furthermore, any real geochemical systems with water involve mixed aqueous fluids; pure water is rarely found in nature, much less in the interiors of planets. The addition of ions to water may affect mineral solubility at these conditions. Despite the need to understanding water/ion solutions at these conditions, many questions remain, and first principles simulations are rare.

One of the properties most crucial to geochemical modeling is the dielectric constant of water, which is the ratio of water's permititivity to that of vacuum. Until recently, a lack of experimental constraints on the dielectric constant of water even at lower-crustal conditions (above 0.5 GPa) had limited the study of water-rock interactions. Large differences existed in the extrapolation of models calibrated only at low pressures and temperatures[259]. A significant advance came recently from the study of Pan et al., who used first-principles molecular dynamics simulations to yield robust constraints on the dielectric constant of water at high pressure and temperature [193]. Nevertheless, the understanding of the effect

of ions on water's dielectric constant at these conditions remains poorly understood.

While there are no direct measurements of the dielectric constant in mixed fluids at conditions relevant to the lower crust and mantle, there are some computational studies that have predicted that the addition of components such as CO_2 and NaCl modifies the dielectric constant with moderate reductions. At deep crust conditions (0.5-1.5 GPa), Galvez et al. derive the dielectric constant of mixed C-O-H fluids from classical electrostatic modeling. The dielectric constant of the fluid mixture is about 22% lower than that of pure H2O at 0.5 GPa, but only 4% lower at 1.5 GPa [89]. Foustoukos et al., used a similar approach to study H2O-NaCl, using a simple empirical model based on the solubility of quartz in H2O-NaCl brines [73]. Their results indicate that, for a 22 wt% NaCl solution, the dielectric constant of the mixed fluid is similar to that in a graphite-saturated C–O–H fluid.

The distribution of aqueous fluids in the earth has been investigated using magnetotelluric measurements of electrical conductivity in the Earth's crust. Highly conductive zones have been reported in the middle portion of the Earth's crust, and subduction zones [173, 119, 164]. The understanding of these conductivity zones, however, must properly take into consideration the effects of elevated temperature and pressure on the fluid conductivity [228]. Nevertheless, atomistic modeling of water in these conditions is difficult due to dissociation, and we know of no first principles studies that have addressed the question of conductivity of mixed water-ion solutions at high pressure/temperature.

While the effect of ions in aqueous solutions on dielectric constants and conductivities may have the most implication for geochemical models, many other fundamental questions have not been explored at these conditions. Such questions begin with the basic properties of solvation structure of ions in a dissociative liquid. They also include the effect on more subtle properties like the molecular polarizability. Finally, they include questions of the nature of vibrational spectra of ions in dissociative water, and whether the addition of such ions at these conditions may show signatures that are neither present in bulk ion solutions or pure water at high pressure/temperature.

CHAPTER 3

THEORETICAL BACKGROUND AND MODELS

3.1 Introduction

In this chapter, we present the theoretical background on which this dissertation is based, including both the theories of modeling water as well as the strategy that we employed: first principles simulation.

In section 3.2, we focus on various structural models of water. Here we begin with describing general approaches to modelling water. We then discuss molecular dynamics and classical potentials for water. Afterwards, we introduce density functional theory and its application to first principles molecular dynamics. In section 3.3, we describe the theory of vibrational spectroscopy, including infrared and Raman spectra. In section 3.4 we turn to describe the ionic conductivity, and how it is computed from first principles.

3.2 Structural Models of Water

As discussed in the previous chapter, experimental work has been invaluable in understanding all properties of water and aqueous solutions across a range of conditions. Measurements of bulk water properties including vibrational spectra, heat capacities, enthalpies, electrical conductivity, and phase transition have been the foundations of our understanding of water. However, a complete understanding of the molecular behavior of water requires theories and computational methods that both faithfully reproduce and interpret measurements and make experimentally verifiable predictions. While in this thesis we focus on first principles molecular dynamics, we first briefly survey existing models of water, a topic which has has already been thoroughly reviewed [19, 69, 75, 76, 77, 30, 62, 50].

Water has variably been modelled at levels of detail ranging from a primitive solvation medium to full quantum mechanical detail of electronic structure. The earliest attempts

of describing water models may be attributed to W. C. Roentgen in 1892, who proposed water to be a mixture of low and high density fluids [222]. Later, in 1933, Bernal and Fowler suggested that the electronegativity of oxygen and the tetrahedrality of water due to electrostatic forces may be the cause of many of the extraordinary properties of the liquid [22]. This recognition was the basis on which early classical models of water were built. Pople extended the idea in describing a point-charge model for tetrahedral water molecules [206]. Nevertheless, the realistic modelling of water only accelerated when meaningful physical models were coupled with the increases in computing power during the latter half of the 20th century.

3.2.1 Classical Molecular Dynamics

Hydrogen bonds continuously break and reform in water, leading to a fundamentally dynamical chemical system. The understanding of such a sensitive dynamical system calls for computational tools that may access both detailed time propagation of molecular properties as well as collective averages in time and space.

Molecular dynamics (MD) is such a computational technique used to model the time evolution of an atomic or molecular system. Molecular dynamics requires the calculation of forces from a potential energy surface. These forces are used to solve the Newton equation of motion and are applied to atoms over a discrete timestep, yielding updated positions. This process is repeated regular intervals, allowing for the propagation of the MD trajectory in time. MD trajectories find vast application across physics and chemistry, where they are used to investigate the structural and dynamical properties of broad classes of systems. The positions and velocities of any atom in the course of a molecular dynamics algorithm are given, e.g. by using the Verlet algorithm [274] used to integrate Newton's equation of motion:

$$-\frac{\partial E(\mathbf{R}_j)}{\partial \mathbf{R}_i} = m_i \ddot{\mathbf{R}}_i \tag{3.1}$$

where $E(\mathbf{R}_j)$ is the total energy of the system and m_i and $\ddot{\mathbf{R}}_i$ are the mass and acceleration of the ith nuclei, respectively. Naturally, the challenge in the MD approach is in the calculation of $E(\mathbf{R}_j)$, the driving potential of the molecular dynamics.

In the 1970s, classical molecular dynamics modelling of water began to emerge, where the driving potential was generated with semiempirical methods. Rahman and Stillinger performed pioneering simulations on a model based on tetrahedral arrangements of charges centered on a Lennard-Jones site [213]. Later evolution of this model into the ST2 model had considerable success in interpreting the structure of liquid work [252]. Since then, many other computationally efficient classical potentials have been developed for the study of water. One class of such potentials is simple point charge (SPC) water [21], where three positively charged hydrogen sites are counteracted by a negatively charged oxygen. Another are the transferable intermolecular potential (TIP) models [125] which have become standard workhorses alongside SPC models. Many more rigid water potentials have emerged, with variations in the number and type of the interaction sites (e.g. TIP3P, TIP4P, TIP5P). A major limitation of many classical potentials is the neglect of electronic effects such as polarization and polarizability. Extensive work has been made to compensate for this whether by correction factors in the SPC/E model [20] or more sophisticated polarizable potentials where effective charge distributions are effected by the environment [50]. A significant development in modeling of classical potentials has been the emergence of one such polarizable potential, namely MB-pol. The MB-pol functional form includes one body terms as well as explicit two and three body terms from dimer and trimer interaction energies at the CCSD(T) level of theory [9, 10]. It has been shown to have excellent accuracy for several

structural, thermodynamic, and dynamic properties of water [217].

Most classical potentials are subject to key drawbacks due to their semiemperical foundations. As many potentials are uniquely fitted to specific chemical system or environment, they lack transferability to new contexts. Furthermore, in many cases missing electronic polarizability limits the type of questions one may study with classical potentials. In this thesis, we show that molecular polarizability is crucial to all systems of interest, as we are studying solvation chemistry, nanoconfined environments, and water at extreme conditions. While some classical potentials have been used with varying levels of success to describe ion solvation and even nanoconfinement, most classical potentials have no means to break and reform bonds, making them unsuitable to describe water in our high P/T regime of interest, where molecules are highly dissociative. Given these limitations, a more accurate method that accounts for electronic degrees of freedom is needed.

3.2.2 First Principles Molecular Dynamics

An entirely different route to compute an energy term in Eq. 3.2.1 that drives molecular dynamics is the so-called "ab initio" approach. The seminal contribution of Car and Parinello was to apply density functional theory to drive molecular dynamics [35], which is the primary tool of the rest of this thesis. Here, the potential energy surface of the water is computed "on the fly" through means of quantum mechanical calculations. In density functional theory, instead of computing all wavefunctions of all electrons and nuclei in a given system, we only explicitly deal with the electron density and, within the Kohn-Sham formulation, with single particle orbitals. We also employ the Born–Oppenheimer approximation, where atomic nuclei are classical particles while the electronic wave functions are computed quantum mechanically. Here we further lay the theoretical groundwork of first principles molecular dynamics in further detail.

Density Functional Theory

Density functional theory (DFT) exactly describes ground state properties of a quantum mechanical system using only the electron density $n(\mathbf{r})$, instead of the many-body wavefunction. The theoretical foundation for modern DFT results was laid by the theorems of Hohenberg and Kohn [113], in 1964. These theorems state the following:

1. For any system of interacting particles in an external potential $V_{ext}(\mathbf{r})$, the potential $V_{ext}(\mathbf{r})$ is determined uniquely, modulo a constant, by the ground state electronic density, $n(\mathbf{r})$. Thus $n(\mathbf{r})$ uniquely determines all properties of the system.

2. The total energy of an interacting electronic gas is a unique functional of the electron density. The ground state energy is the variational global minimum of this unique functional $E[n]$.

These state that ground and excited state properties of a system of interacting electrons under an external potential may be derived from the ground state charge density of the system, hence eliminating the need to evaluate explicitly the many-body wavefunction; the energy of the interacting electronic system is a unique functional of its charge density.

In 1965, Kohn and Sham introduced the casting of DFT that enabled the broad proliferation of the theory in electronic structure calculations [135]. A system of N_E interacting electrons is mapped onto a fictitious system of non-interacting electrons with the same electron density. The wavefunction of the non-interacting system is a Slater determinant constructed from the orbitals of the individual non-interacting electrons ψ_v, which are obtained by self-consistently solving a set of Schrödinger-like equations called the Kohn-Sham equations. The ground state density of N non-interacting electrons is defined as:

$$n(\mathbf{r}) = \sum_v 2|\psi_v(\mathbf{r})|^2, \tag{3.2}$$

where the summation runs over occupied states, and $\psi_v(\mathbf{r})$ are single particle wavefunc-

tions. The kinetic energy of the system is

$$T_0 = -\frac{1}{2}\sum_v \langle\psi_v|\nabla^2|\psi_v\rangle \tag{3.3}$$

The Hartree energy, defined as the classical electrostatic energy of a system with electron density $n(\mathbf{r})$ is:

$$E_H[n] = \frac{1}{2}\int d\mathbf{r}d\mathbf{r}'\frac{n(\mathbf{r})n(\mathbf{r}')}{|\mathbf{r}-\mathbf{r}'|} \tag{3.4}$$

The Kohn-Sham approach splits the HK functionals into the sum of T_0, E_H, and the exchange correlation (XC) energy E_{xc}, which is an unknown term:

$$F[n] = T_0 + E_H[n] + E_{xc}[n]. \tag{3.5}$$

Applying the second HK theorem, we obtain the Euler equation:

$$\frac{\delta T_0}{\delta n(\mathbf{r})} + V_{KS}(\mathbf{r}) = \mu \tag{3.6}$$

where μ is the Lagrange multiplier accounting for the constraint on total number of electrons, and V_{KS} is defined as:

$$V_{KS}(\mathbf{r}) = \frac{\delta E_H[n]}{\delta n(\mathbf{r})} + \frac{\delta E_{xc}[n]}{\delta n(\mathbf{r})} + V_{ext}(\mathbf{r}) = V_H(\mathbf{r}) + V_{xc}(\mathbf{r}) + V_{ext}(\mathbf{r}) \tag{3.7}$$

Equation 3.6 is the same as that used to describe a system of non-interacting electrons subject to an effective potential, $V_{KS}(\mathbf{r})$. Thus, we can define the Hamiltonian of an auxiliary non-interacting system as the following:

$$H_{KS} = \frac{1}{2}\nabla^2 + V_{KS}(\mathbf{r}). \tag{3.8}$$

The corresponding Schrodinger equation of the non-interacting system is:

$$H_{KS}\psi_i(\mathbf{r}) = \varepsilon_i\psi_i(\mathbf{r}), \tag{3.9}$$

which is the Kohn-Sham equation. Eq. 3.9 is to be solved self-consistently, and the eigenvalues and eigenfunctions of the equation are Kohn-Sham energies and orbitals.

Ab initio molecular dynamics (AIMD) unifies molecular dynamics with the fully quantum level electronic characterizations by using density functional theory to compute the force on each atom at each individual timestep. In AIMD simulations, the Kohn-Sham energy $E_{KS}(\mathbf{R}_j)$ is computed by solving the Kohn-Sham equations (Eq. 3.9), at each time step. Here, the evaluation of the force term is carried out by virtue of the Hellmann-Feynman theorem [169]. Thus AIMD provides a fully ab initio framework by which to propagate an MD trajectory. Relative to classical molecular dynamics, AIMD has much higher computational cost but higher accuracy for a range of systems, configurations, bonding patterns, and physical phenomena. AIMD simulations also allow for the calculation of quantities like dipole moments and polarizabilities, which are needed to compute ab initio vibrational spectra.

As mentioned above, the exact form of the XC functional is unknown, and approximate functionals are used in practical implementations of DFT. The most commonly used

approximations are the local and semi-local approximations which assume that the exchange-correlation energy depends only locally and semi-locally on the electron density. The Local Density Approximation (LDA) [38, 201] for the exchange correlation energy is written as:

$$E_{xc}^{LDA} = \int d\mathbf{r}\, n(\mathbf{r}) \epsilon_{xc}^{LDA}(n(\mathbf{r})) \tag{3.10}$$

where $\epsilon_{xc}^{LDA}(n(\mathbf{r}))$ is the exchange-correlation energy per electron of a homogeneous electron gas with density n. More sophisticated approximations, such as the generalized gradient approximation (GGA), include the gradient of the electron density in the XC functional:

$$E_{xc}^{GGA} = \int d\mathbf{r}\, n(\mathbf{r}) \epsilon_{xc}^{GGA}((n(\mathbf{r})), \nabla(n(\mathbf{r})) \tag{3.11}$$

Commonly used GGA functionals include BLYP [16] and PBE [199]. These two functionals have been widely used for simulations of water and aqueous solutions and provide a reasonable description of their structural and vibrational properties [95, 58], although simulations are run at artificially elevated temperatures (e.g. 400 K) to match the structural properties measured in liquid at 300 K [58]. Functional development remains an active area of research in first principles modeling of water. The so-called hybrid density functionals include a fraction of the Hartree-Fock exchange energy [200, 17, 111]. The van der Waals functionals [144, 64, 268] include a accounting of long-range dispersion interactions. Finally, the meta-GGA functionals [18, 41, 262] involve a kinetic energy density term. The Strongly Constrained and Appropriately Normed (SCAN) meta-GGA exchange-correlation functional

[257] has been applied to water, reporting accurate structural and density characteristics at 330K [47, 141]. In yet another approach, recently water was modeled with a dielectric dependent hybrid (DDH) functional, where the fraction of exact exchange is set equal to the inverse of the high-frequency dielectric constant of the liquid. The DDH water was shown to have excellent properties of structure and density, as well as good agreement in dielectric properties [86]. We refer to the excellent review of Gillan et al.[95] for a comprehensive analysis of density functional theory modeling of water.

While certainly a considerable challenge, the exchange correlation functional is not the only hurdle towards successful modeling of water. The effect of statistical averages has been often neglected in first principles simulations of water, with recent studies pointing to the importance of multiple independent trajectory sampling in order to accurately capture uncertainty on most computed quantities [58, 141]. The question of statistics remains difficult, as first principles simulations are exceedingly expensive computationally relative to classical simulations. Another important consideration in first principles water modeling is the quantum nature of protons in water [39, 166]. Recent studies have explored including nuclear quantum effects using ring-polymer methods combined with multiple time-step scheme [167, 232, 168]. NQEs have been shown to effect structure, dynamics, and vibrational properties of water, notably causing red-shifting in vibrational spectroscopy [106, 191].

3.3 Vibrational Spectroscopy

Since the vibrational frequencies of a water molecule are particularly sensitive to the surrounding environment, vibrational spectroscopy is a powerful tool for characterizing both molecular structure and dynamics of aqueous systems from the gas to the condensed phases. In this section we will explore the theoretical bases of infrared spectroscopy, which is based on the absorption of infrared radiation, and Raman spectroscopy, which is based on the inelastic scattering of light. In general, vibrational spectra may be computed either by diagonalizing the dynamical matrix to obtain normal modes or by computing time correlation functions

(TCF)[174]. Given the limitations of the former for disordered systems such as aqueous solutions, in this thesis we compute spectra with the latter. Any vibrational spectra calculated from AIMD are based on the Fourier transform of certain autocorrelation functions: power spectra use the particle velocities, IR spectra rely on dipole moments and Raman spectra are obtained from molecular polarizabilities.

3.3.1 Maximally Localized Wannier Functions

For both infrared and Raman spectra as well as our calculations of ionic conductivity, it is necessary to introduce the idea of maximally localized Wannier functions (MLWF) [280, 171]. Wannier functions are orthonormal localized functions that span the same space as the eigenstates of a band or group of bands. Maximally localized Wannier functions, or localized molecular orbitals, use a small number of functions to describe electronic states. By the unitary transformation of the Kohn–Sham orbitals, the MLWF method yields localized Wannier orbitals whose positions (the Wannier function centers) may be interpreted as the location of electron pairs. Thus, MLWFs provide a simple and intuitive tool for qualitatively studying bonding. The position of the nth MLWF, w_n is defined as:

$$r^0_{n,i} = \frac{L_i}{2\pi}\mathrm{Im}\ln\langle w_n|e^{i\frac{2\pi}{L_i}r_i}|w_n\rangle, \tag{3.12}$$

where L_i is the ith cell dimension, and the Wannier functions w_n are obtained by applying a unitary transformation to the occupied Kohn-Sham eigenstates (See Eq. 3.2.2) so as to minimize the total spread [170, 105].

The Γ point formulation of the MLWF approach is used to compute dipole moments of molecules in condensed phases [242]. MLWFs may be assigned to individual molecules based on distance criteria, allowing for calculations of molecular dipole moments. Similarly, the total dipole moment $\mathbf{M}(t)$ is calculated by summing over all ionic charges and MLWFs of the system [266]. In the case of water, this amounts to:

$$\mathbf{M}(t) = e \cdot \sum_{i=1}^{N_H} \vec{R}_i^H(t) + 6e \cdot \sum_{i=1}^{N_O} \vec{R}_i^O(t) - 2e \cdot \sum_{i=1}^{N_{MLWF}} \vec{R}_i^{MLWF}(t), \tag{3.13}$$

where e is the elementary charge, $\vec{R}^O(t)$ and $\vec{R}^H(t)$ are the coordinates of oxygen and hydrogen atoms, respectively, and $\vec{R}^{MLWF}(t)$ are the coordinates of the center of a maximally localized Wannier function. The summations run over all species of the simulation cell.

3.3.2 Infrared Spectroscopy

A given molecular vibration is considered "infrared active" if its charge distribution changes during the vibration [183]. Put differently, infrared spectroscopy detects changes to the sample dipole moment, $\mathbf{M}$. In the literature, there exist two methods to compute the dipole moment under periodic boundary conditions: the Berry phase approach to polarization [221] and the maximally localized Wannier function scheme [170, 244, 243], which we employ here. The infrared intensity is:

$$\begin{aligned} A(\omega) &\propto \frac{2\pi\omega^2\beta}{3cV} \int dt e^{-i\omega t} \langle \mathbf{M}(0)\mathbf{M}(t) \rangle \\ &= \frac{2\pi\beta}{3cV} \int dt e^{-i\omega t} \langle \dot{\mathbf{M}}(0)\dot{\mathbf{M}}(t) \rangle \end{aligned} \tag{3.14}$$

where $\mathbf{M}(t)$ is defined from Eq. 3.13. The correlation function in Eq. 3.14 is classical, requiring a quantum correction factor to approximate the quantum time correlation function [11]. Here we used the so-called harmonic prefactor, which has been shown to satisfy the fluctuation-dissipation theorem and detailed balance [215].

3.3.3 Raman Spectroscopy

The dipole moment, connected to infrared spectroscopy, measures anisotropy of a charge distribution. In contrast, the polarizability, connected to Raman spectroscopy, is the ability of a molecule to alter its charge distribution under external electric fields. The calculation of polarizability ($\alpha = \frac{d\mathbf{M}}{d\mathbf{E}}$) is more computationally intensive than the calculation of the dipole moment.

In this thesis, we use Density Functional Perturbation Theory (DFPT) [15] which is a linear response method for studying a system's response of a system to external perturbations. Here we only discuss DFPT for homogeneous electric field perturbations. Given the Kohn-Sham equations (Eq. 3.9) where H_{KS} is the one-electron Kohn-Sham Hamiltonian and ψ_v is the vth occupied Kohn-Sham orbital with eigenvalue ϵ_v, the response to an external perturbation may be written with Sternheimer equation [251, 158]:

$$(H_{KS} - \epsilon_v)\hat{P}_c|\Delta\psi_v\rangle = -\hat{P}_c\Delta V_{KS}|\psi_v\rangle, \tag{3.15}$$

where $\hat{P}_c$ is the projector onto the unoccupied Kohn-Sham orbitals: $\hat{P}_c = \sum_{c=1}^{+\infty}|\psi_c\rangle\langle\psi_c| = \mathbf{1} - \sum_{v=1}^{N_{orb}}|\psi_v\rangle\langle\psi_v|$, N_{orb} is the number of occupied Kohn-Sham orbitals, and ΔV_{KS} is the perturbation to the Kohn-Sham potential. If the perturbation comes from a macroscopic electric field $\mathbf{E}$, the perturbation potential is written as

$$\Delta_{KS} = e\mathbf{E}\cdot\mathbf{r} + \Delta V_H + \Delta V_{xc}, \tag{3.16}$$

where e is the elementary charge, $\mathbf{r}$ is the position operator, and ΔV_H and ΔV_{xc} are

perturbations to the Hartree and exchange-correlation potentials, respectively. After solving the Sternheimer equation (Eq. 3.15), we can compute the change in electronic density:

$$\Delta n = 2 \sum_{v=1}^{N_{orb}} \psi_v^*(\mathbf{r}) \Delta\psi_v(r) + c.c. \tag{3.17}$$

The induced dipole moment of the system under the perturbing field is given by:

$$\Delta\mathbf{M} = -\mathrm{e} \int_\Omega \mathbf{r} \Delta n d\mathbf{r}, \tag{3.18}$$

where Ω is the volume of the system. The polarizability tensor, α is defined as:

$$\Delta\mathbf{M} = \alpha\mathbf{E}, \tag{3.19}$$

In our calculations, an electric field is applied along each Cartesian axis and the elements of the polarizability tensor α are obtained by dividing the corresponding component of the sample dipole moment by the electric field strength.

As described above, in a periodic system, the ground state maximally localized Wannier functions (MLWF), w_n, may be obtained by applying a unitary transformation $\mathbf{u}$ to the eigenstates of the Kohn-Sham Hamiltonian. We project the system polarizability tensor α onto MLWFs [170] in order to define effective polarizabilities:

$$\alpha = \sum_{j=1}^{N_{\text{orb}}} \alpha_j^{\text{eff}}, \tag{3.20}$$

where α_j^{eff} is the effective polarizability corresponding to the jth MLWF.

Isotropic and anisotropic Raman spectra are defined as:

$$R_{\text{iso}}(\omega) \propto \frac{\hbar\omega}{k_b T} \int dt e^{-i\omega t} \langle \bar{\alpha}(0)\bar{\alpha}(t) \rangle \tag{3.21}$$

$$R_{\text{aniso}}(\omega) \propto \frac{\hbar\omega}{k_b T} \int dt e^{-i\omega t} \langle \frac{2}{15} \text{Tr}\beta(0)\beta(t) \rangle \tag{3.22}$$

In equations 3.21 and 3.22, ω is the frequency, Tr is the trace, and $\bar{\alpha}$ and β are the isotropic and anisotropic components of the polarizability tensor, α: $\bar{\alpha} = \frac{1}{3}\text{Tr}\alpha$ and $\beta = \alpha - \bar{\alpha}\mathbf{I}$, where $\mathbf{I}$ is the identity tensor. Unpolarized Raman spectra are computed as $R_{\text{unpol}} = R_{\text{iso}} + \frac{7}{4R_{\text{aniso}}}$ [154].

In the case of water, there are four MLWFs associated with each water molecule, corresponding to two covalent bonds pairs (BP), and two lone pairs (LP). The effective molecular polarizability of the ith water molecule is:

$$\alpha_i^{\text{eff}} = \alpha_{i,\text{BP1}}^{\text{eff}} + \alpha_{i,\text{BP2}}^{\text{eff}} + \alpha_{i,\text{LP1}}^{\text{eff}} + \alpha_{i,\text{LP2}}^{\text{eff}} \tag{3.23}$$

The induced dipole $\Delta\mathbf{M}_i$ of the ith molecule is therefore:

$$\Delta \mathbf{M}_i = \alpha_i^{\text{eff}} \mathbf{E} \tag{3.24}$$

We cast the expression of the Raman intensities (Eq. 3.21, 3.22) in terms of effective molecular polarizability:

$$R_{\text{iso}}(\omega) \propto \frac{\hbar\omega}{k_b T} \int dt e^{-i\omega t} \langle \sum_{i,j} \bar{\alpha}_i^{\text{eff}}(0) \bar{\alpha}_j^{\text{eff}}(t) \rangle \tag{3.25}$$

$$R_{\text{aniso}}(\omega) \propto \frac{\hbar\omega}{k_b T} \int dt e^{-i\omega t} \langle \frac{2}{15} \text{Tr} \sum_{i,j} \beta_i^{\text{eff}}(0) \beta_j^{\text{eff}}(t) \rangle \tag{3.26}$$

Where $\bar{\alpha}^{\text{eff}} = \frac{1}{3}\text{Tr}\alpha^{\text{eff}}$ and $\beta^{\text{eff}} = \alpha^{\text{eff}} - \bar{\alpha}^{\text{eff}}\mathbf{I}$, and $\mathbf{I}$ is the identity tensor. Tr denotes the trace operator. By separating $i = j$ and $i \neq j$ terms of the summation, we may obtain the intramolecular and intermolecular contributions to the Raman intensity, respectively.

3.4 Molecular Polarizability

The effective molecular polarizability, α_i^{eff}, that is used to compute Raman spectra in Eq. 3.25 and 3.26, is computed from the projections of total polarization onto molecules, thus containing environmental effects. It is different than the intrinsic molecular polarizability, α_i, which depends only on the electronic structure of the molecule. For the purpose of comparing water molecules under different environments as they are studied in this thesis, it is therefore more appropriate to consider the intrinsic polarizability α_i.

Following others [110, 229, 32, 177], we define the molecular polarizabilities, α_i, of the ith water molecule as:

$$\Delta\mathbf{M}_i = \alpha_i \mathbf{E}_i^{\text{loc}} \tag{3.27}$$

where $\Delta\mathbf{M}_i$ is the induced dipole of the ith molecule given in Eq 3.24 and $\mathbf{E}_i^{\text{loc}}$ is the local electric field acting on the ith molecule. Importantly, note that $\mathbf{E}_i^{\text{loc}}$ contains the contribution of both the applied field and the field induced by the induced dipole $\Delta\mathbf{M}_j (j \neq i)$ of all other molecules in the system via dipole-induced dipole (DID) interactions. While higher multipolar contributions may also affect $\mathbf{E}_i^{\text{loc}}$, the DID interactions tend to dominate [270]. The evaluation of the DID interaction tensor has been previously carried out with Ewald summation techniques [275, 3, 142, 184]. In this work we used the method developed by Pan et al. [195] to compute the intrinsic water molecular polarizability α_i, using the electron polarization density of the whole system. The calculated α_i includes multipolar interactions at all orders.

3.5 Ionic Conductivity

We compute the ionic conductivity σ within linear response, using the Green-Kubo formalism [174]:

$$\sigma = \frac{1}{3k_b TV} \int_0^\infty \langle \dot{\mathbf{M}}(0)\dot{\mathbf{M}}(t)\rangle dt, \tag{3.28}$$

Where k_b is Boltzmann's constant, T is the temperature, V is the cell volume, $\mathbf{M}$ is from Eq. 3.13 and the angled brackets indicate the average over time origins. Instead of evaluating the integral of the correlation function of the total dipole moment derivative, we may equivalently employ the Einstein relation:

$$\sigma = \lim_{t\to\infty} \frac{1}{6tk_bTV}\langle[\mathbf{M}(t) - \mathbf{M}(0)]^2\rangle \tag{3.29}$$

While the equations for computing the ionic conductivity are straightforward, we emphasize that a fully ab initio representation of $\mathbf{M}$ is computationally demanding, with most studies in literature resorting to a-priori definitions of effective charges [52, 172, 79, 97]. It is our explicit computation of the MLWFs in Eq. 3.13 that allows for the evaluation of $\mathbf{M}$ entirely from first principles. The ionic conductivity, similar to quantities such as the shear viscosity, is based on the time correlation function of a collective quantity. In general, such quantities have much greater statistical noise than self quantities such as the diffusion coefficient for which statistics are increased by the number of particles [52].

CHAPTER 4

SIMPLE AQUEOUS SOLUTIONS AT AMBIENT CONDITIONS

Reproduced in part from V. Rozsa, T. A. Pham, and G. Galli, J. Chem. Phys. 152, 124501 (2020), with the permission of AIP Publishing.

4.1 Introduction

The chemistry of water and aqueous salt solutions have been active areas of research for decades [165, 108]. However, the effect of ions on the structure and electronic properties of water is not yet fully understood. While the way ions modify the structure of water within the first solvation shell of ions is well established, the effect of ions outside the first solvation shell is more controversial [245, 197]. Some experimental studies, including dielectric relaxation [137] and neutron diffraction [160] measurements, support the view in which ions significantly affect global water properties, such as diffusion, viscosity, and hydrogen bonding [165, 225]. Other experiments employing X-ray absorption spectroscopy [181], fs-IR [188] and terahertz spectroscopy [84] point instead at negligible global effects of ions on the surrounding liquid.

Such discrepancies have motivated numerous simulation studies, however even first-principles simulations have differed in their assessment of the global effect of salt properties. In this chapter, we present first principles simulations of bulk water and three hydrated cations: Li^+, Na^+, and K^+. In order to analyze trends in structural and dielectric properties with statistically significant trajectories, we chose a semi-local functional (PBE [198]), which is computationally less expensive than, e.g. hybrid functionals, and an elevated temperature (400 K) to model the structural properties of water at ambient conditions [239]. Motivated by the necessity of multiple independent trajectories to resolve statistical uncertainty[58, 141], we computed 10 independent trajectories with a total trajectory time of ∼0.45 ns for each bulk cation solution. The total simulation time of the calculations reported here amounts to ∼1.4 ns, which was possible to span using a relatively simple functional as PBE, but it

would have been prohibitively difficult to obtain with more sophisticated density functionals. In this chapter we present an analysis of hydrogen bonding changes in the presence of ions and we relate structural changes to variations of dielectric properties, in particular molecular polarizabilities, which we find to be key fingerprints to understand water modifications both in the presence of ions.

In section 4.2, we discuss the computational methods in our simulations of bulk aqueous solutions. In section 4.3, we present the results and analysis of our statistically robust simulations of solvated ion solutions. In section 4.4, we describe the application of our aqueous K^+ simulations to a study of isotopic fractionation. In section 4.5 we offer conclusions.

4.2 Computational Methods

The bulk salt solutions were modeled by periodic cubic cells consisting of a single ion and 63 water molecules, with the excess charge compensated by a uniform background charge. For all the models, the size of the cell was chosen to yield the experimental density of liquid water under ambient conditions. The salt concentration corresponds to 0.87 M.

Our first-principles simulations were carried out using Born–Oppenheimer molecular dynamics simulations with the Qbox code [104, 1], with the interatomic forces derived from density functional theory (DFT) with the Perdew, Burke, and Ernzerhof (PBE) [198] approximation for the exchange-correlation energy functional. The interaction between valence electrons and ionic cores was represented by norm-conserving pseudopotentials [107], and the electronic wave functions were expanded in a plane-wave basis set truncated at a cutoff energy of 85 Ry. All hydrogen atoms were replaced with deuterium to maximize the allowable time step, which was chosen to be 10 au. We note that the PBE functional was employed in this work as we are mainly interested in trends among the ions, and the use of this functional allows for statistically robust simulations at a manageable computational cost [58, 85].

We equilibrated the bulk solutions at a constant temperature of T = 400 K for at least 10 ps. An elevated temperature was chosen, as use of the PBE approximation is known to yield

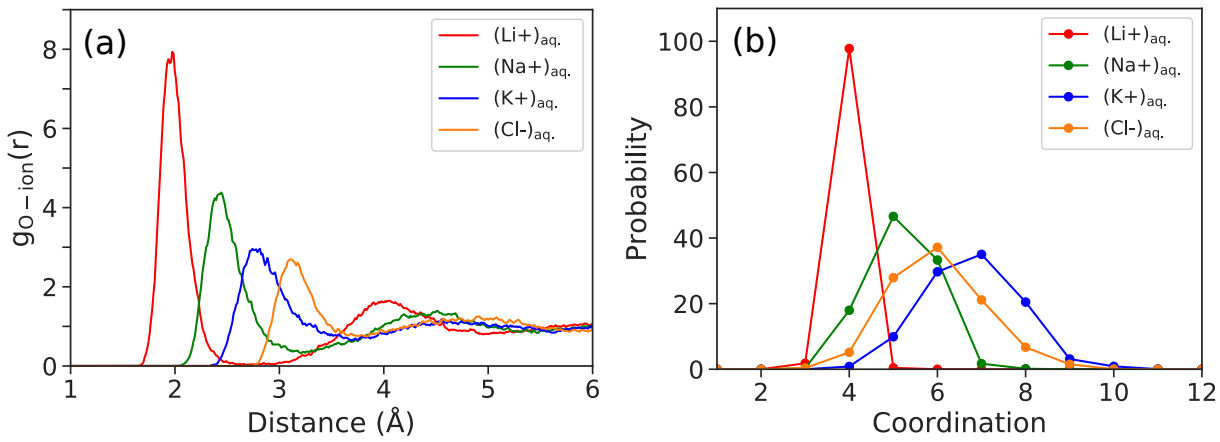

Figure 4.1: Oxygen-ion radial distribution functions (a) and ion coordination numbers (b) of bulk aqueous solutions.

an overstructured liquid at ambient conditions, and the use of a simulation temperature of ~400 K was shown to recover the experimental liquid structure and water diffusion coefficient at T = 300 K[239]. Statistics were collected over 45 ps for each microcanonical simulation of the bulk solutions, for which we propagated 10 independent trajectories for each cation and one trajectory for Cl^-.

4.3 Statistically robust simulations of solvated ion solutions

4.3.1 Structure and Hydrogen Bonding

We begin by examining the solvation properties of the ions in the bulk solutions using the radial distribution functions (RDF) between the solvated ions and oxygen atoms of water molecules (Fig. 4.1). As expected, the position of the RDF first maximum follows the ion size: $Li^+ < Na^+ < K^+ < Cl^-$, yielding a value of 1.97, 2.44, 2.81 and 3.10 Å for Li^+, Na^+, K^+, and Cl^-, respectively. We also report in Fig. 4.1 the average oxygen coordination number in the first ion solvation shell, for which we obtained values of 4.0, 5.2, 6.8, and 6.0 for Li^+, Na^+, K^+, and Cl^-, respectively. Overall, these results are consistent with those of several previous first principles simulations [204, 88, 13, 290] as well as with experimental

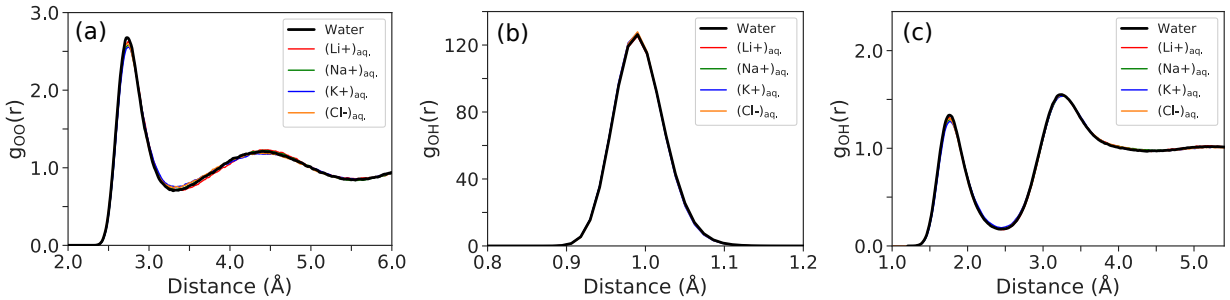

Figure 4.2: Oxygen-oxygen (a) and oxygen-hydrogen (b, c) radial distribution functions (RDF) for bulk water solutions. (b) shows the covalent bond peak, while (c) shows the second and third peaks of the O-H RDF.

studies [96, 55]. We also found that oxygen-oxygen and oxygen-hydrogen RDFs (Fig. 4.2) of all solutions do not show any notable change relative to the corresponding ones of pure water, pointing to minor effects of the ions on the structure of water at the concentration considered here.

To better understand ion effects on the water structure, we investigated hydrogen bonding of the salt solutions. The subtleties of ion effects on hydrogen bonding require attention to statistical uncertainty. We used 10 independent trajectories for each cation solution to obtain statistically robust results with error bars on hydrogen bond averages, which were computed using the Student's T-test for 95% confidence intervals, as in earlier studies [85, 58]. Here, two water molecules were considered to be hydrogen bonded if their oxygen-oxygen separation was less than 3.35 Å while the O...OH angle was equal to or less than 30°[156]. The average hydrogen bond per water molecule in the first and second solvation shells of the ions are shown in Fig. 4.3, and are compared to the results obtained for liquid water using the PBE400 data set [58]. Our results clearly show a substantial suppression of hydrogen bonds in the first solvation shell for all the cations, with the extent of the reduction decreasing with the ion size: $Li^+ < Na^+ < K^+$. In addition, we found that the presence of the cations leads to a weak enhancement in the number of hydrogen bonds in the second solvation shell relative to pure liquid water. However, beyond the second shell, our results show that the hydrogen bonds of none of cation solutions differ from those of liquid water. Our findings

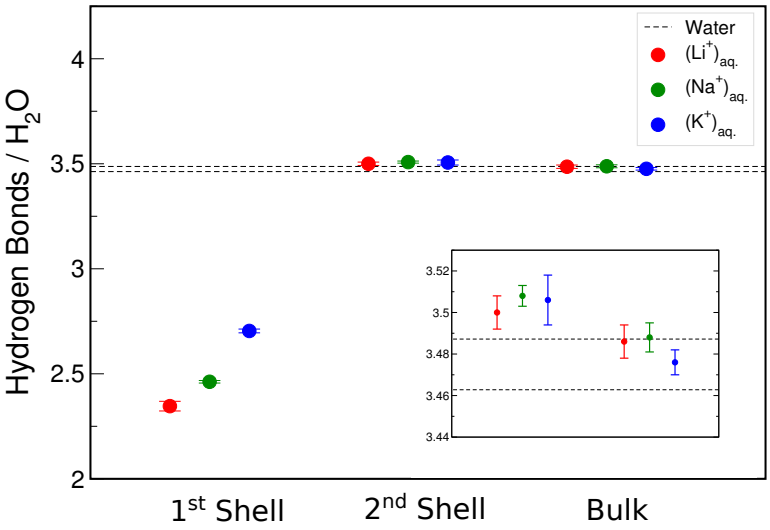

Figure 4.3: Number of hydrogen bonds per molecule in bulk solutions as a function of solvation shells. "Bulk" refers to the region outside the second solvation shell. The boundaries of the 95% confidence interval for pure water (dotted horizontal line) were computed using the PBE400 pure water data set[58]. The inset shows a closer view of the data for the second shell and bulk regions.

are consistent with the results reported by Gaiduk et al. [85] for Na^+, and indicate that the effect of all cations on the water structure is rather localized.

In addition to the analysis of hydrogen bonds, we investigated the diffusion coefficient of water in the presence of the ions, which was computed from the oxygen mean-squared displacement. We find that the presence of cations does not affect water diffusion in a statistically significant manner (See Table 4.1 for specific values) at the concentration considered here, consistent with our hydrogen bonding analysis.

4.3.2 Dipole Moments and Molecular Polarizabilities

We now turn to examine ion effects on the dielectric properties of water molecules. In particular, the dipole moments of water molecules in the solutions were computed using maximally localized Wannier functions [280, 170, 105], and their average values are shown in

Solution	D [O] (x10^{-5} cm^2/s)
Pure Water	1.95(27)
w/ Li^+	1.90(30)
w/ Na^+	2.21(34)
w/ K^+	2.43(39)

Table 4.1: Diffusion coefficient of oxygen for bulk ion solutions. The standard deviation of the average diffusion coefficients of 10 independent trajectories is given in parentheses. Data for bulk water comes from the PBE400 data set [58].

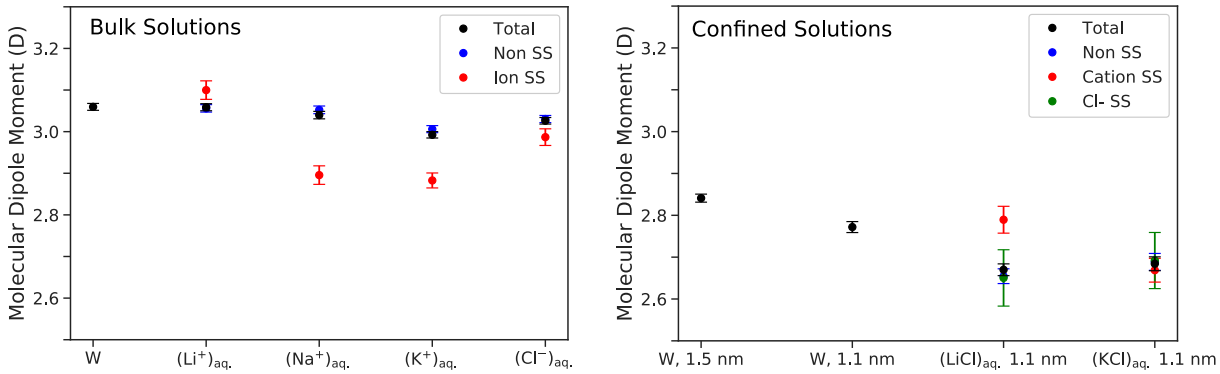

Figure 4.4: Left panel: The molecular dipole moments of water molecules in the bulk aqueous solutions. Right panel: The molecular dipole moments of water molecules in the confined solutions. "Ion SS" and "Cation SS" denote water molecules within the first solvation shell of the ion/cation, while "Non SS" denotes all water molecules outside the first solvation shell of the ions. In the abscissa: "W" denotes pure water.

Fig. 4.4 (left panel). We find that, for all the ions other than Li^+, the water molecules in the first ion solvation shell yield an average dipole moment reduced by at most ~0.15 D, i.e., less than 10% relative to the rest of the liquid. In contrast, water molecules in the first solvation shell of Li^+ exhibit a relatively weak enhancement of the dipole moment by ~0.04 D. Most importantly, we found that ion effects on the water dipole moment are negligible beyond the first solvation shell, consistent with a previous study by Gaiduk *et al.*, where the authors concluded that water dipole moment is insensitive to the long-range effects introduced by the solute (see Fig. 4.5). Our results are also in agreement with a previous first-principles study [123], which similarly concluded that the effect of ions on the dipole moment of water molecules is confined to the first solvation shell for aqueous solutions with the same cations, at a similar concentration.

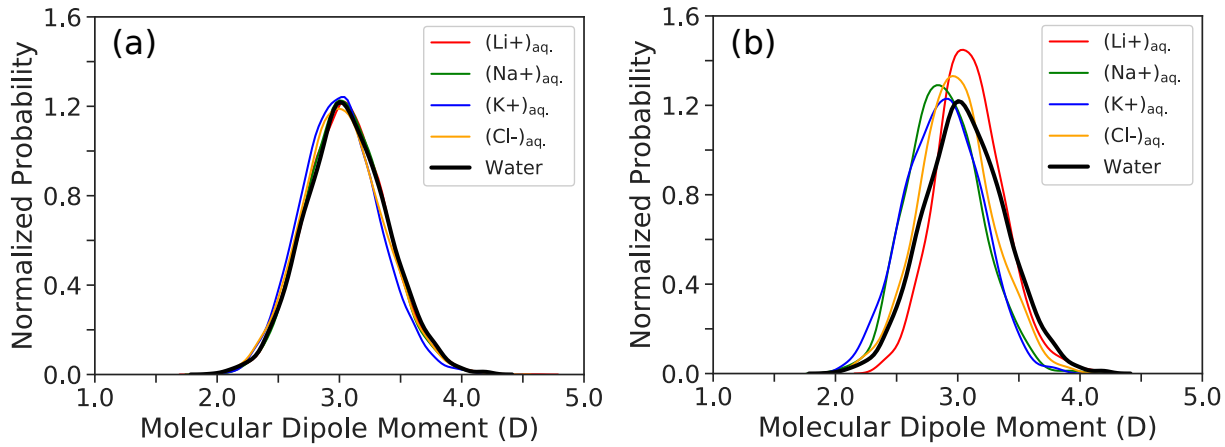

Figure 4.5: (S3) Molecular dipole moment distributions of bulk aqueous solutions for (a) the molecules outside the ion solvation shell (non-SS) and (b) molecules within the first solvation shell (SS).

The study of Ref. [85] on NaCl has shown that the molecular polarizability of water molecules is a useful fingerprint of ion effects. We investigate here whether this conclusion is general and applies to all alkali halide cations. In Ref. [85], an effective molecular polarizability (α_i^{eff}) of water molecules was employed, which is defined through the polarization $\mathbf{P}_i$ of the ith molecule as $\mathbf{P}_i = \alpha_i^{\text{eff}}\mathbf{E}$, where $\mathbf{E}$ is an applied (external) electric field. In this work, we instead employed the intrinsic water molecular polarizability α_i, which is related to the total polarization through the local field $\mathbf{E}_{loc}$ acting on the molecule: $\mathbf{P}_i = \alpha_i\mathbf{E}_{loc}$, where $\mathbf{E}_{loc} = \mathbf{E}$–$\mathbf{E}_{env}$, and $\mathbf{E}_{env}$ is the field induced by the polarization $\mathbf{P}_j$(j≠i) of the rest of the system on the ith molecule via multipolar interactions. More specifically, we used the method developed by Pan et al. [195] to compute $\mathbf{E}_{env}$ and thus the calculated α_i includes multipolar interactions at all orders. A comparison of α_i and α_i^{eff} for water is given in Fig. 4.6, where we found that α_i has lower values and narrower distributions; however the relative ordering of the projections over molecular axes is the same for both quantities. For the purpose of comparing water molecules under different environments, it is more appropriate to consider the intrinsic polarizability. Indeed, in the definition of intrinsic polarizabilities, induced fields from the environment are subtracted ($\mathbf{E}_{env}$) and hence polarizabilities under different environments can be directly compared. In addition, we emphasize that the use of

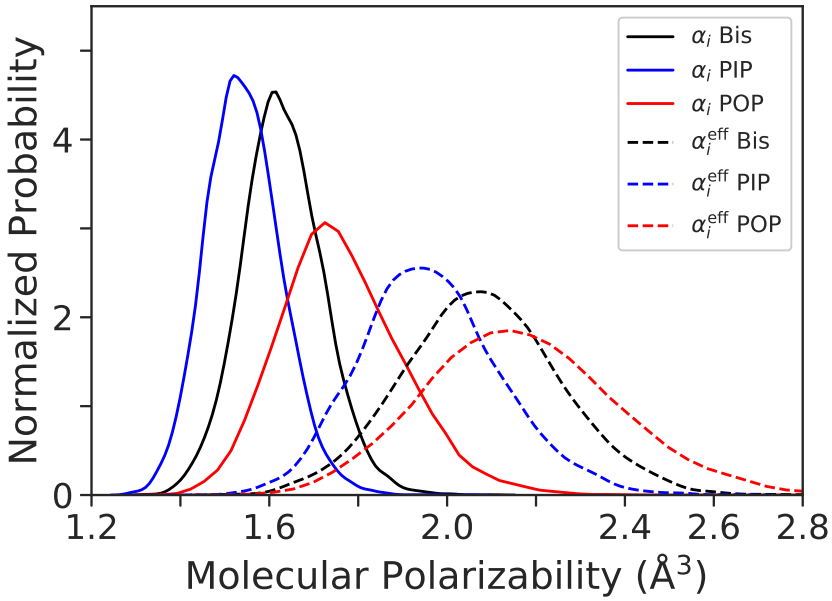

Figure 4.6: Comparison of the molecular polarizability, α_i, and the effective molecular polarizability, α_i^{eff}, for pure water. "Bis" indicates the component of molecular polarizability that bisects the HOH angle; "PIP" indicates the component perpendicular to Bis in the molecular plane; "POP" indicates the component perpendicular and out of the molecular plane.

the method introduced in Ref. [195] enables the inclusion of not only dipolar but also all the multi-polar effects in the calculation of the polarizability at the DFT level of theory.

Our results for the average molecular polarizabilities ($\bar{\alpha}_i = \frac{1}{3}\text{Tr}(\alpha_i)$) of bulk ionic solutions using 140 snapshots extracted equally spaced in time from our simulations are reported in Fig. 4.7 (left panel). Snapshots used for the calculations were extracted from the entire trajectories, with at least ~0.24 ps interval in between. We note that results obtained with 80 and 140 snapshots were indistinguishable. In particular, we compared the average water molecular polarizability in the first ion solvation shell (SS) to all molecules outside the first solvation shell (defined as non-SS) for all ion solutions. We found that the average $\bar{\alpha}_i$ of the first SS is smaller than that of non-SS for all cations, following the ion size trend $Li^+ < Na^+ < K^+$. The most significant change in polarizabilities between SS and non-SS was obtained for Li^+, with ~6% difference, whereas Na^+ and K^+ yield a more modest difference of ~2% and ~1%, respectively. Our result indicates that the trend of $\bar{\alpha}_i$ among the cations is con-

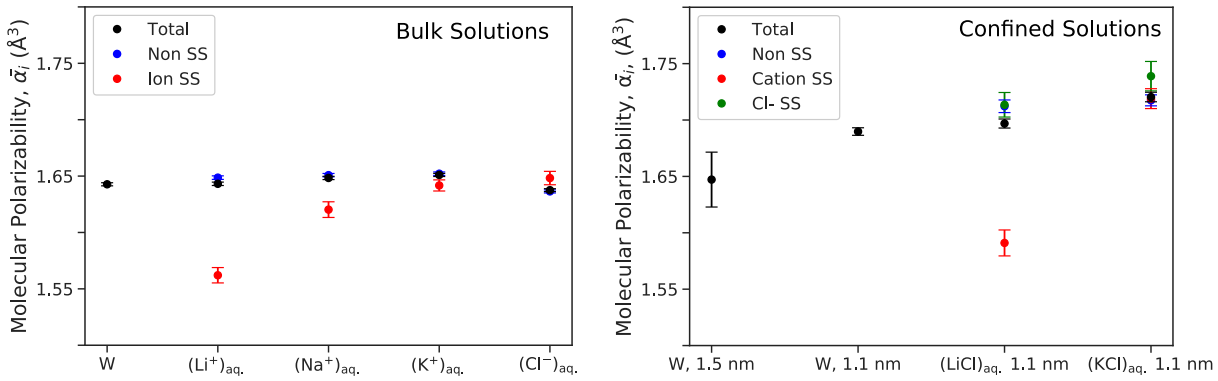

Figure 4.7: Left panel: Average molecular polarizability, $\bar{\alpha}_i$, of water molecules in the bulk solutions. Right panel: Average molecular polarizability, $\bar{\alpha}_i$, of water molecules in the confined solutions. "Ion SS" and "Cation SS" denote water molecules within the first solvation shell of the ion/cation, while "Non SS" denotes all water molecules outside the first solvation shell of the ions. In the abscissa: "W" denotes pure water.

sistent with that found for the number of hydrogen bonds (Fig. 4.3). In addition, consistent with Ref. [85], we found that the cations and Cl^- have different effect on the polarizability of water. The perturbation induced on the water structure by the cations is local, whereas that of Cl^- can extend beyond the second solvation shell, leading to an overall reduction in the water polarizability (Figure 4.7, left panel). We therefore expect that introducing Cl^- to the solutions would slightly reduce the overall polarizability of water molecules in the solution.

In addition to the average water molecular polarizability, we investigated the component of α_i in the direction perpendicular to and out of the molecular plane (α_i^{POP}), which has been shown to be the most affected by the hydrogen bonding environment, and even sensitive to changes outside the second solvation shell of sodium. [85]. We show the long-range effect of ions on α_i^{POP} in Fig. 4.8, where "bulk" refers to all water molecules outside the second solvation shells of ions. We found that both $\bar{\alpha}_i$ (see Fig. 4.9) and α_i^{POP} show the same trend as a function of ion type. Importantly, we found that α_i^{POP} of water molecules outside the second ion solvation shell is different relative to the corresponding average value in pure water, outside statistical error bars. Our results indicate that polarizabilities are sensitive

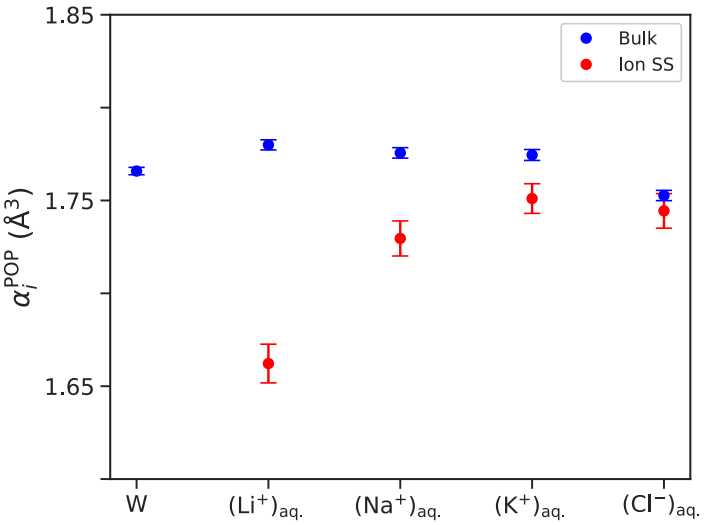

Figure 4.8: Perpendicular out-of-plane (POP) dimension of molecular polarizability (α_i^{POP}) for bulk solutions. "Ion SS" denotes molecules within the first solvation shell of the ions, while "Bulk" denotes molecules outside the second solvation shell of the ions. In the abscissa: "W" denotes pure water.

to changes induced by ions even beyond the second ion solvation shell of the liquid. Hence, we confirm and generalize the findings of Gaiduk et al., who found that polarizabilities are fingerprints of long-range effects in the case of Na^+, though in Ref. [85] only values of α_i^{eff} were computed, in contrast to intrinsic polarizabilities in this work.

4.4 Equilibrium Isotopic Fractionations of Potassium in Minerals and Water

4.4.1 Introduction

Having analyzed in detail the effect of ions on water in several aqueous solutions, we turn to a different application of these simulations to a problem of geophysical relevance: isotopic

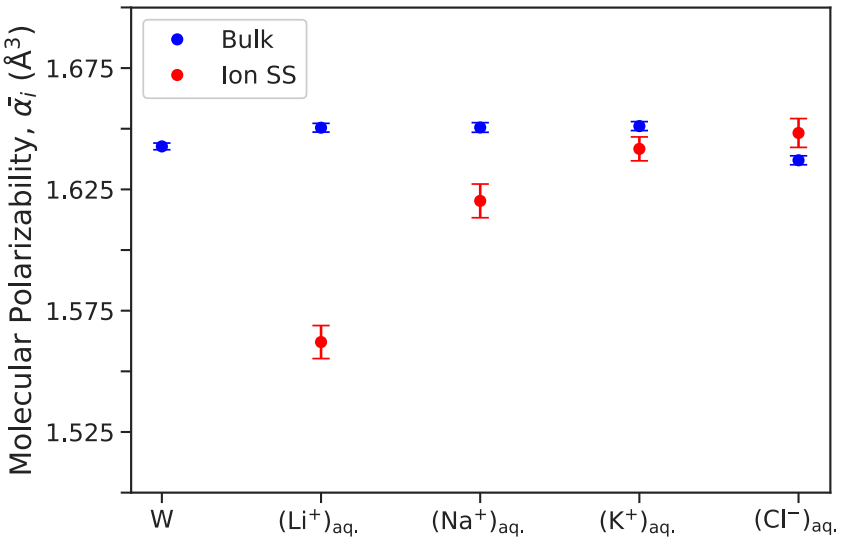

Figure 4.9: (S4) Average molecular polarizability, $\bar{\alpha}_i$, of water molecules in the bulk solutions. In the abscissa: "W" denotes pure water. "Ion SS" denotes molecules within the first solvation shell of the ions, while "Bulk" denotes molecules outside the second solvation shell of the ions.

fractionation of potassium in water. Potassium is a moderately volatile, lithophile element that is present in relatively high abundance in the ocean [148], Earth's crust [148, 281, 224], bulk silicate Earth (BSE) [36, 258], and in the solar system [7, 100, 153]. Understanding how K isotopes are fractionated at equilibrium between vapor and condensed phases is important for understanding why planetary bodies are depleted in these moderately volatile elements. The isotopic compositions of K could help trace continental weathering and reverse weathering in marine sediments, which both influence climate processes. Thanks to improvements in purification protocols and multi-collector inductively coupled plasma mass spectrometry, the isotopic composition of K (expressed using the $^{41}K/^{39}K$ ratio) can now be measured with a precision of ~0.1‰ [277, 276, 45, 115, 147, 196, 116], spurring wide interest in K isotopes, which have now been used to study weathering [216, 145], seafloor alteration [196], and volatile element depletion in planetary materials [118, 5, 263, 277]. Potassium isotopic compositions are reported as the per mil (‰) deviation (^{41}K) of the ratio of two potassium stable isotopes ^{41}K (6.730%) and ^{39}K (93.258%), relative to the inferred composition of the

mantle or the NIST standard reference material 3141a. K isotopic variations are thought to follow the laws of mass-dependent fractionation, meaning that the relative deviations in the $^{40}K/^{39}K$ ratio are approximately half those of the $^{41}K/^{39}K$ ratio ($\delta^{40}K = \delta^{41}K/2$)[23, 272].

Despite progress made in measuring the isotopic compositions of K, understanding the cause of the isotopic variations for those elements in natural systems can be challenging, partly due to an insufficient theoretical understanding of how equilibrium and kinetic processes control the fractionations of K isotopes. More work is needed to understand how the isotopic compositions of Rb and K are fractionated at equilibrium between different minerals, gaseous species, and water. These fractionations are critical for interpreting the origin of K isotopic variations in low-temperature aqueous systems and planetary/nebular processes that involved the volatilization of K. Because equilibrium fractionation properties are highly sensitive to coordination numbers and to nearest neighbor distances, we used first-principle molecular dynamics (FPMD) to study hydrated K^+, capturing many instantaneous configurations of the fully hydrated K^+, in contrast to a cluster approach where static hydrated configurations are considered.

Our results suggest that (a) equilibrium fractionation between K-bearing clays (illite) and seawater could be a significant source of oceanic ^{41}K enrichment and (b) the bond strengths of Rb and K are similar, so equilibrium processes are expected to impart correlated isotopic fractionations to Rb and K that differ from kinetic processes, providing a means of distinguishing between equilibrium and kinetic processes in nature.

4.4.2 Equilibrium Fractionation

Isotopic fractionation is defined as the relative partitioning of heavier and lighter isotopes between two coexisting phases in a natural system. Equilibrium isotope fractionation for an element X between two phases A and B ($\alpha_{A\text{-}B}$) can be calculated using the rpfr (or β-factor) of each phase[23, 272, 26]

$$\alpha_{\mathrm{A-B}} = \frac{(X'/X)_{\mathrm{A}}}{(X'/X)_{\mathrm{B}}} = \frac{\beta_{\mathrm{A}}}{\beta_{\mathrm{B}}} \tag{4.1}$$

where X, X' refer to the abundances of two isotopes of an element. The rpfr can be calculated from [26]

$$\beta = \left(\prod_{i=1}^{3N} \prod_{\mathbf{q}} \frac{\nu_i}{\nu_i'} \times \frac{\mathrm{e}^{-h\nu_{\mathbf{q},i}/2kT}}{1-\mathrm{e}^{-h\nu_{\mathbf{q},i}/kT}} \times \frac{1-\mathrm{e}^{-h\nu'_{\mathbf{q},i}/kT}}{\mathrm{e}^{-h\nu'_{\mathbf{q},i}/2kT}} \right)^{1/n\cdot N_{\mathbf{q}}} \tag{4.2}$$

where N is the total number of atoms in the unit cell, $\nu_{\mathbf{q},i}$ and $\nu'_{\mathbf{q},i}$ are the frequencies of vibrational mode i for two isotopes at a given wavevector $\mathbf{q}$, $N_{\mathbf{q}}$ is the total number of $\mathbf{q}$-vectors, and n is the number of isotopic sites in the unit cell. When measured experimentally, equilibrium isotopic fractionation (in ‰) between two phases is expressed as

$$\Delta_{\mathrm{A-B}}(‰) = 1000 \ln \alpha_{\mathrm{A-B}} = 1000(\ln \beta_{\mathrm{A}} - \ln \beta_{\mathrm{B}}) \tag{4.3}$$

To good approximation, one can write 1000 ln β as a polynomial expansion in even powers of the inverse of the temperature [57, 205]

$$1000 \ln \beta = \frac{A_1}{T^2} + \frac{A_2}{T^4} + \frac{A_3}{T^6} \tag{4.4}$$

where A_1, A_2, A_3 are constants that depend on the mineral/phase considered. The coefficient of the first-order term, which always dominates the rpfr, especially at high temperatures (>200K), can be rewritten as

$$A_1 = 1000 \left(\frac{1}{M'} - \frac{1}{M} \right) \frac{\hbar^2}{8k^2} F \tag{4.5}$$

where $\hbar$ is the reduced Planck constant, k is the Boltzmann's constant, M' and M are the masses of the two isotopes, and $\langle \mathrm{F} \rangle$ is the mean force constant of the K or Rb bonds (equivalent to the spring constant of a harmonic spring), which can be calculated from the partial phonon density of states (PDOS, $g(E)$)[57]

$$F = \frac{M}{\hbar^2} \int_0^{+\infty} E^2 g(E) \mathrm{d}E \tag{4.6}$$

At high temperature for $^{39/41}$K, eq 4.4.2 can be written as

$$1000 \ln \beta_{\mathrm{K}} \simeq 5500 \frac{\langle F \rangle}{T^2} \tag{4.7}$$

4.4.3 FPMD of Potassium in Water

We carried out FPMD of aqueous K^+ as described in Section 4.3, using the Perdew, Burke, and Ernzerhof (PBE) exchange correlation functional [199]. This relatively simple functional was chosen as it was reported that there is no significant difference in rpfr calculated from PBE and van der Waals functionals [67]. We used the same functional for minerals and hydrated potassium, to facilitate comparing fractionation factors for different systems and to take advantage of cancellation of errors. We considered configurations of solvated K^+ from 20 uncorrelated snapshots over the entire trajectory.

In addition to the hydrated K^+ simulations, several minerals were studied, including orthoclase ($KAlSi_3O_8$), microcline ($KAlSi_3O_8$), albite ($NaAlSi_3O_8$), anorthite ($CaAl_2Si_2O_8$), muscovite ($KAl_3Si_3O_{12}H_2$), illite ($KAl_2Si_4O_{11}F$), phlogopite ($KAlSi_3Mg_3O_{12}H_2$), and sylvite (KCl). A visualization of the mineral structures as well as the aqueous K^+ systems is given in Fig. 4.10. Structural relaxation and phonon calculations were carried out with the Quantum ESPRESSO code[93]. Phonon calculations were performed for each structure using density functional perturbation theory [15]. Further details of the solid phase calculations are given in Ref [288].

We calculated the rpfr for aqueous K^+ by extracting 20 snapshots for rpfr convergence with respect to number of snapshots) from MD trajectories, and performed phonon calculations on the relaxed snapshot structures, to use a consistent approach for the liquid and the minerals. In PDOS calculated for aqueous K^+, we can clearly see couplings to the H-O-H bending and O-H stretching modes at higher frequency (Fig. 4.11).

The calculated rpfr of aqueous K^+ shows some variability (see error bars in Fig. 4.12 across different snapshots due to dynamical changes in the coordination environment of K^+. In our FPMD simulation we found that the coordination number of K^+ varies from 4 to 10 between snapshots, with an average coordination number of 6.7. We averaged the rpfr obtained from 20 snapshots uniformly spaced in time, whose average coordination number, 7.2, is comparable to that obtained over the whole trajectory. Similar to the results of Ducher

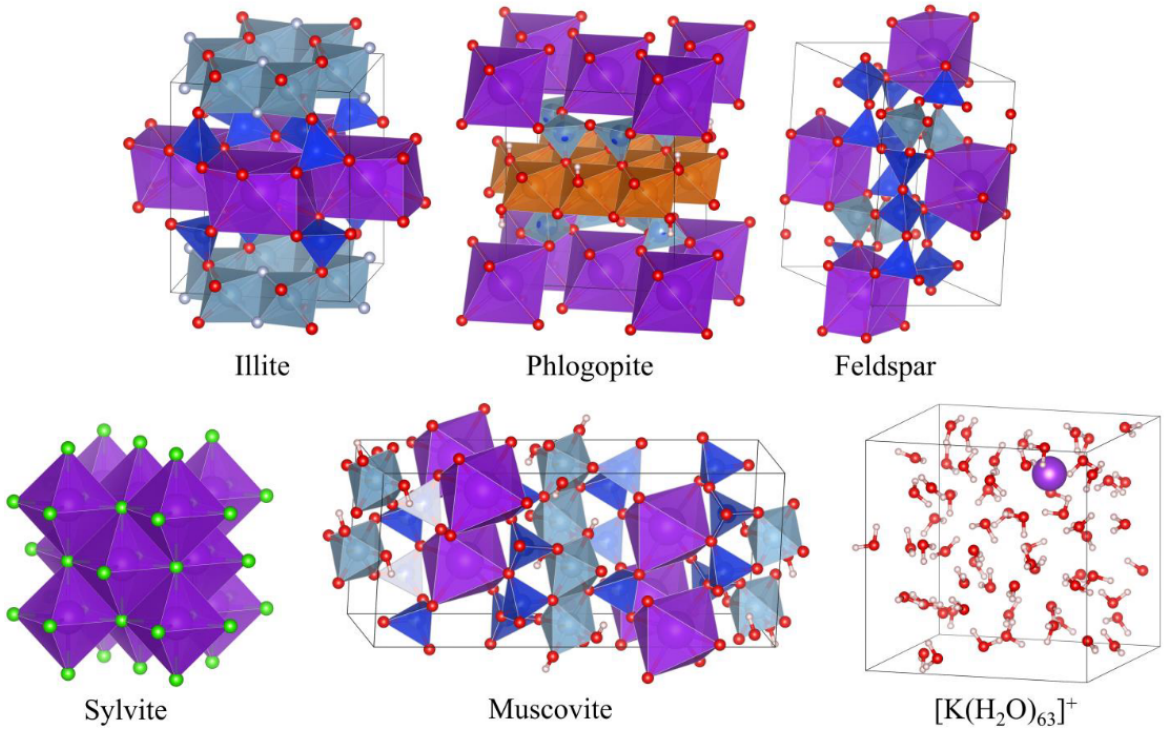

Figure 4.10: Structures of minerals and aqueous K^+. Albite, anorthite, microcline, and orthoclase share the feldspar structure. Red represents O, white represents H, green represents Cl, dark blue represents Si, light blue represents Al, purple represents K, brown represents Mg, and grey represents F.

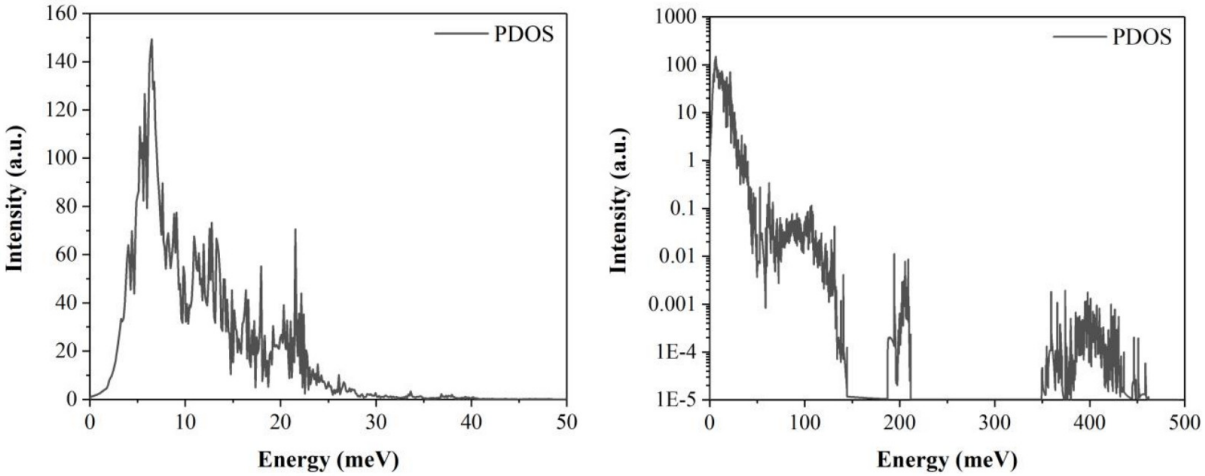

Figure 4.11: Phonon density of states (PDOS) for aqueous K^+. The full spectrum in logarithm scale shows higher frequency couplings to the H–O–H bending and O–H stretching modes.

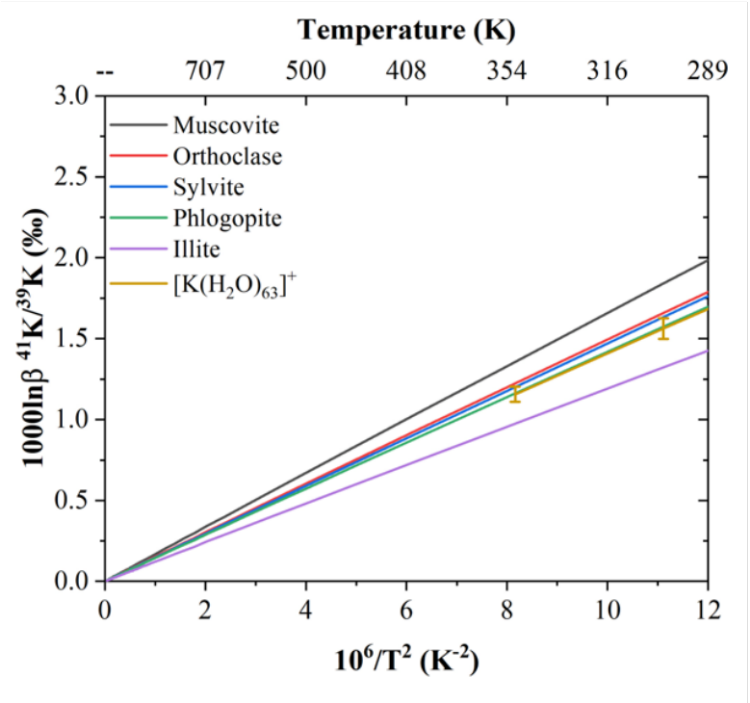

Figure 4.12: Temperature dependence of 1000 ln β for K. The error bars are the standard errors of the mean value for aqueous K^+.

et al. for solvated Zn, we found little correlation between rpfr and coordination numbers (R^2=0.05), so the small difference between the average over the selected samples and whole trajectory should have an insignificant impact on the computed rpfr [67]. We also assume that the dependence of phonon frequencies on temperature is weak, and use the computed phonon frequencies across all temperatures.

4.4.4 Mineral/Water Fractionation: Comparison with Experiments

While the database of K isotope measurements of sediments and products of weathering is rapidly expanding[45, 115, 216], the rpfr of K^+ in aqueous media has not been studied. The most relevant data that we can compare our calculations with are the experimental results from W. Li et al., who studied equilibrium isotopic fractionation of K between soluble K-salts and their saturated solutions, a proxy for aqueous K^+[147]. W. Li et al. found indistinguishable K fractionation between sylvite and aqueous K^+. One concern with such experiments

is that achieving equilibrium between phases at room temperature can be difficult. Our calculated rpfr indicates that sylvite and aqueous K^+ have indistinguishable fractionation at room temperature, given the current analytical precision on δ41 K measurements (~0.1‰). Our results thus agree well with the experimental results of W. Li et al. One potential concern is that W. Li et al. used saturated sylvite solution while in our calculation K^+ is not saturated. However, we do not expect the concentration to have a significant impact based on the study by Wang et al.[279], which shows that an increase in the simulation concentration of Mg^{2+} from 1 Mg in 50 H_2O to 1 Mg in 30 H_2O only increases the rpfr of Mg by ~3%.

4.4.5 Mineral/Water Fractionation: Implications

Wang et al. reported a K isotopic fractionation between seawater and the BSE of $\delta^{41}K_{ocean–BSE}$ = +0.6‰[276]. The residence time of K is on the order of 10 Myr, indicating that although only a handful of measurements were reported, they are likely representative of Earth's oceans as a whole because the ocean mixing timescale is only around 1 kyr[51]. The heavy isotope enrichment in seawater most likely involve K isotopic fractionation (kinetic or equilibrium) between solvated K^+ and minerals, either during terrestrial weathering[139, 61] or due to uptake in silicate minerals in sediments and hydrothermal systems[27, 250, 139]. Li, S. et al. evaluated the global mass-balance of K in the oceans using $\delta^{41}K$ values of the sources and sinks as inputs[145]. They found that potassium dissolved in river waters seems to be shifted in its $\delta^{41}K$ value by +0.55 *pm* 0.29‰ relative to the clay fraction in the same rivers, and globally, the $\delta^{41}K$ value of rivers is 0.22 ± 0.04‰, which is shifted by ~+0.3‰ relative to the BSE, which has a $\delta^{41}K$ value of ~ -0.52.(18,25,38) The riverine $\delta^{41}K$ value is low relative to the seawater value of ~+0.06 ± 0.10‰[146], which corresponds to a seawater-riverine run off difference in $\delta^{41}K$ values of +0.28 ± 0.11‰. There is insufficient data available at present to evaluate what processes affect K isotopes on a global scale, which is important if one wants to transfer knowledge of the present terrestrial cycle to the geological record.

Our calculation of the K isotopic fractionation between solvated K^+ and illite allows us to partially address this question. At a temperature of 25 °C relevant to weathering at the surface of continents, we calculate an equilibrium δ^{41}K fractionation between water and illite of +0.24‰. At a higher temperature of 100 °C relevant to hydrothermal systems or smectite-illite conversion in sediments (50–100 °C), we calculate a fractionation of +0.16‰. The K inputs in the oceans comprise (1) continental weathering and (2) mid ocean ridge hydrothermal fluxes. The sinks that remove K from the oceans are (1) the formation of K-bearing authigenic clays and ion exchange during sediment diagenesis and (2) low temperature basalt alteration. Given the elevated temperatures involved in hydrothermal systems, it is unlikely that the hydrothermal flux has a δ^{41}K value higher than seawater to balance the low δ^{41}K value of the rivers. To explain the elevated δ^{41}K value of seawater relative to the sources (rivers and mid ocean ridges), there must therefore be a negative fractionation between the K sinks and seawater ($\delta^{41}K_{sinks} - \delta^{41}K_{seawater} < 0$). Li, S. et al. estimated that the isotopic fractionation between sediments (formation of authigenic clays and ion exchange) and seawater must be 0.6 to 0.3‰[145]. The equilibrium fractionation that we calculate between illite and solvated K^+ is 0.24‰, which could explain the seawater value if the 0.3‰ shift between sediment and seawater was the correct number or would be insufficient if the shift was actually 0.6‰ (but it could still contribute to half of the overall shift). Further work is clearly needed to better constrain the global geochemical cycle of K. In particular, combining K and Rb isotopic analyses could provide new insights into these processes.

4.5 Conclusions

In summary, we investigated the effect of ions on the structural and dielectric properties of water by carrying out first principles molecular dynamics simulations of several solutions containing alkali ions and alkali halides. In the case of bulk water we found that Li^+ and K^+ have a local effect on the water structure, and that molecular polarizabilities are fingerprints of hydrogen bond changes, generalizing the findings reported by Gaiduk et al. [85] in the case

of Na^+. We also computed diffusion coefficients of water, finding no cations to affect water diffusion in a statistically significant manner at the concentration considered here (0.87 M). This is consistent with the picture that emerged from hydrogen-bonding analysis, showing that none of the cations studied here are global structure maker/breakers, and all have a similar effect on the structure of water. Our work provides a set of statistically robust reference data on ion solvation in pure water for future studies using more sophisticated exchange-correlation functionals beyond the PBE approximation.

We also reported a thorough first-principles study of equilibrium fractionation properties of aqueous K^+ and K in common K-bearing minerals using DFT and FPMD, to provide a framework for interpreting the isotopic variations documented in natural systems for K. In water, we did not find a clear correlation between the strength of the K bonds and the coordination number. The mean force constant of K bonds in water is ~25 N/m. This falls within the range of force constant values calculated by us and others for K-bearing minerals. Based on the computed rpfr, we obtained the equilibrium K isotopic fractionation between aqueous K^+ and illite, taken as a proxy mineral for clays. At 25 °C, the fractionation is +0.24 ‰, suggesting that equilibrium fractionation between aqueous K^+ and K-bearing clay minerals is most likely insufficient to explain the observed K heavy isotope enrichment in seawater or river waters. Instead, this heavy K isotope enrichment could partly reflect kinetic isotopic fractionation associated with diffusive transport or unidirectional chemical reactions.

CHAPTER 5

DIELECTRIC PROPERTIES OF CONFINED AQUEOUS SOLUTIONS

Reproduced in part from V. Rozsa, T. A. Pham, and G. Galli, J. Chem. Phys. 152, 124501 (2020), with the permission of AIP Publishing.

5.1 Introduction

While we find the effect of solvation of ions to be rather local and primarily detectable at longer distances in the molecular polarizability, the nanoscale confinement of water may be expected to significantly perturb water properties. Nanoconfined water of water has already been shown to cause many interesting and exotic changes to water properties, including including enhanced diffusion[159, 14], elevated proton conductivity[163], the formation of one-dimensional water chains [278], square ice phases [133, 46], and diameter-dependent elevated phase transition temperatures [260, 214, 2]. While many classical simulations have been employed [211, 109, 178] to better understand such phenomena, first-principles simulations of aqueous solutions confined at the nanoscale are still relatively rare [49, 278, 140, 241].

In this work, we present analysis of simulations in water and LiCl and KCl solutions under confinement within carbon nanotubes (CNTs) of small diameter (1.1–1.5 nm). In particular, we examine how the molecular polarizabilities are altered by confinement and ion solvation under confinement, having been established as a good fingerprint of ion perturbations in bulk water.

In section 5.2, we discuss he computational methods in our simulations of nanoconfined aqueous solutions. In section 5.3, we present the results and analysis of our confined simulations. In Section 5.4 we present conclusions about the dielectric properties under confinement and their relation to ion solvation properties.

5.2 Computational Methods

We considered water confined in carbon nanotubes (CNTs) with two different diameters, including 1.5 nm and 1.1 nm, that correspond to the (19×0) and (14×0) semiconducting CNTs. Specifically, the liquid confined in CNTs was modelled using supercells of dimension a = b = 21.17 Å, c = 17.0 Å, and a = b = 17.25 Å, c =25.56 Å, respectively. Our simulation model contained 54 water molecules for the 1.5 nm CNT, whereas 34 water molecules were included for the 1.1 nm CNT. We also considered confined salt solutions in the 1.1 CNT, using a supercell that contained one cation-anion pair and 32 water molecules. The concentration for the confined solutions is higher than in the bulk: 1.63 M, but it can still be considered close to a dilute limit case. The number of water molecules was chosen so as to obtain the experimental equilibrium density of water at ambient conditions. In particular, we estimated the thickness of the exclusion volume present at the interface between water and CNT wall to be ∼2 Å [49]. This thickness was employed to determine the number of molecules needed to fill up the tubes in order to obtain a density of ∼1 g/cm^3. All samples were equilibrated for 100 ps using the SPC/E classical potentials for water molecules, and the final structure was then used as input for the first-principles simulations. For the salt solutions under confinement, the initial configurations were obtained by replacing two water molecules with one cation and one anion.

Our first-principles simulations were carried out using Born–Oppenheimer molecular dynamics simulations with the Qbox code [104, 1], with the interatomic forces derived from density functional theory (DFT) with the Perdew, Burke, and Ernzerhof (PBE) [198] approximation for the exchange-correlation energy functional. The interaction between valence electrons and ionic cores was represented by norm-conserving pseudopotentials [107], and the electronic wave functions were expanded in a plane-wave basis set truncated at a cutoff energy of 85 Ry. All hydrogen atoms were replaced with deuterium to maximize the allowable time step, which was chosen to be 10 au. We note that the PBE functional was employed in this work as we are mainly interested in qualitative effects of confinement, and the use of

this functional allows for reasonable structure at manageable computational cost [58, 204].

We equilibrated confined solutions at a constant temperature of T = 400 K for at least 10 ps. An elevated temperature was chosen, as use of the PBE approximation is known to yield an overstructured liquid at ambient conditions, and the use of a simulation temperature of ~400 K was shown to recover the experimental liquid structure and water diffusion coefficient at T = 300 K[239]. We ran single 25 ps simulations for the confined solutions due to their higher computational cost.

5.3 Results and Discussion

5.3.1 Choice of CNT Diameters

We now turn to discuss the perturbation to water induced by confinement. In particular, we examined liquid water and salt solutions confined in carbon nanotubes with the diameter of 1.1 nm. This specific diameter was chosen due to a unique balance between permeability and salt rejection, making it the "Goldilocks diameter" for desalination applications [266]. In addition, it has been shown that 1.1 nm CNTs exhibit a pronounced local minimum in the diameter-dependent diffusion [14] and anomalous phase transitions [2]. For comparison, we also considered liquid water confined in a 1.5 nm CNT; as we show below, water molecules can be effectively considered all interfacial in the 1.1 nm CNT, whereas a demarcation between interior and interfacial water molecules may be made in the 1.5 nm CNT. In this regard, the use of 1.1 nm and 1.5 nm CNTs provides proper models for understanding surface effects under confinement [49, 140].

5.3.2 Confined Water

Our initial examination of the structure of water confined in the CNTs was based on the radial density distribution function. As expected, we find that water molecules do not occupy the central region of the 1.1 nm CNT, and therefore all water molecules can be considered to be

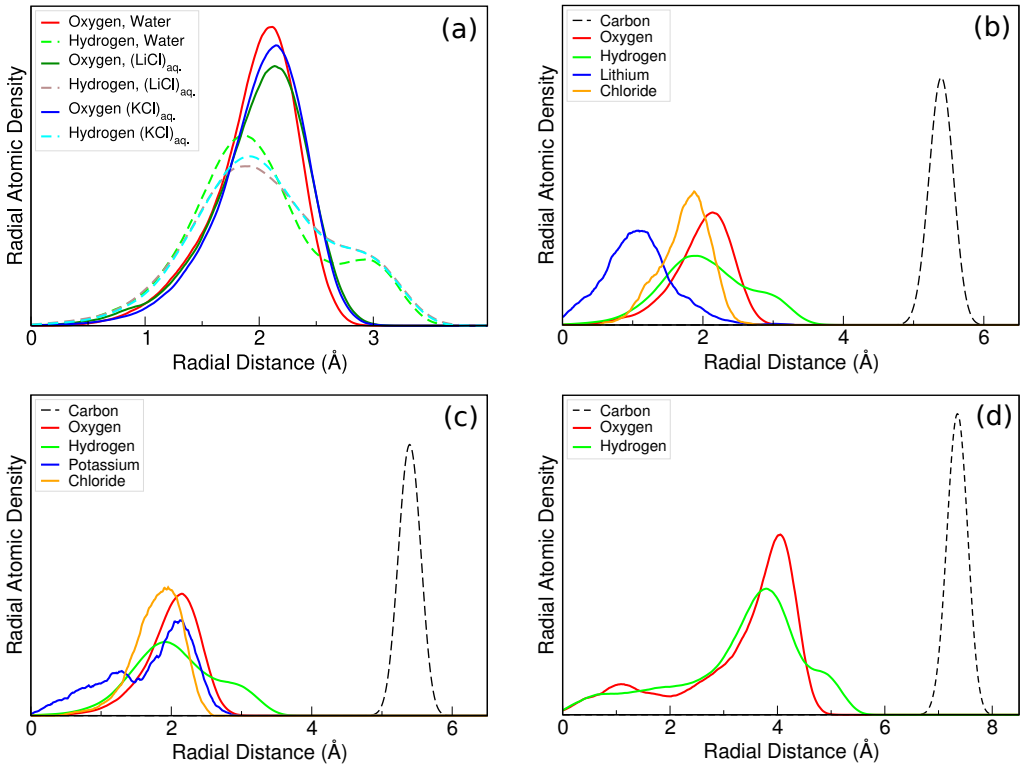

Figure 5.1: (S5) Radial density distributions for (a) oxgyen and hydrogen in all solutions in 1.1 nm nanutubes, (b) all species in $(LiCl)_{aq.}$ 1.1 nm solution, (c) all species in $(KCl)_{aq.}$ 1.1 nm solution, (d) all species in water confined in the 1.5 nm nanotube.

interfacial in this geometry (Fig. 5.1). This is in contrast to the 1.5 nm CNT, which exhibits both well-defined interior and interfacial water layers. A rendering of the two nanotube configurations showing these properties is given given in Fig. 5.2. In addition, we found a strong preferential alignment of water molecules inside in the 1.1 nm CNT, as indicated by the (20°) maximum in the dipole-dipole angle distribution function (Fig. 5.4). We found some preferential alignment of water molecules in the larger CNT as well, however the effect is less pronounced. Finally, over the time scale of our simulations, we found no evidence of the square ice formation at the ambient conditions, consistent with previous reports [49].

The average water dipole moments of the confined systems, as obtained by averaging over 100 snapshots, are shown in Fig. 4.4, right panel. We found that water molecules under confinement exhibit reduced molecular dipole moments relative to the bulk value,

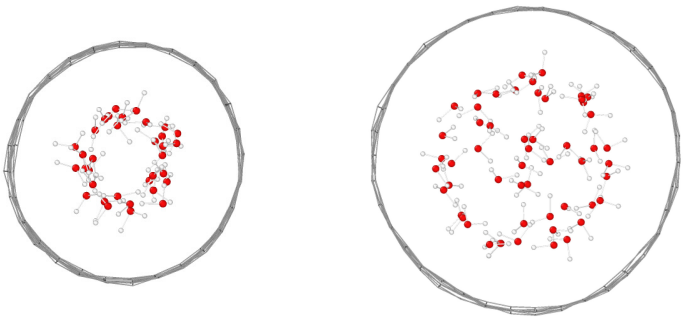

Figure 5.2: (S6) The 1.1 nm diameter CNT (left) and 1.5 nm diameter CNT (right) systems.

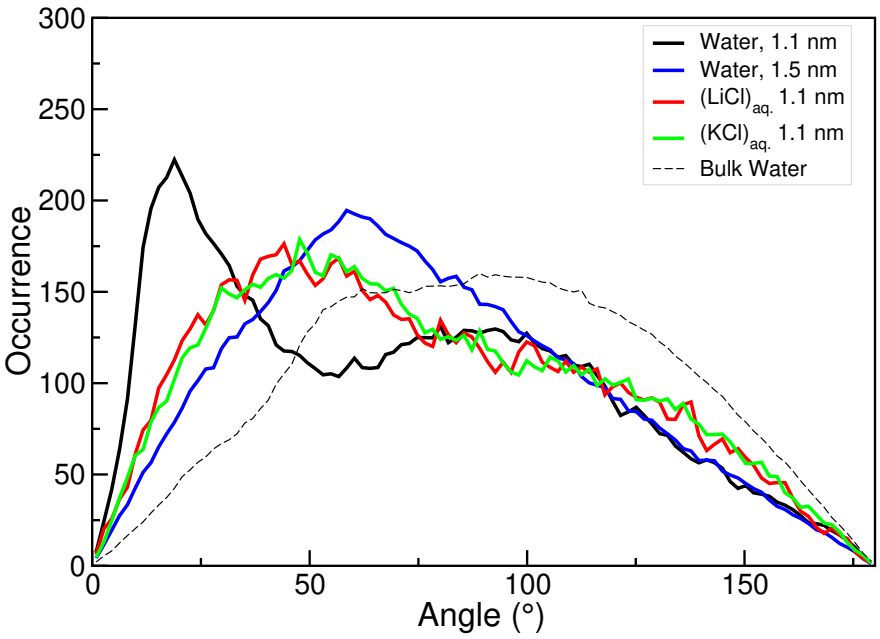

Figure 5.3: (S7) The dipole-dipole angle distributions for confined aqueous solutions as well as pure bulk water.

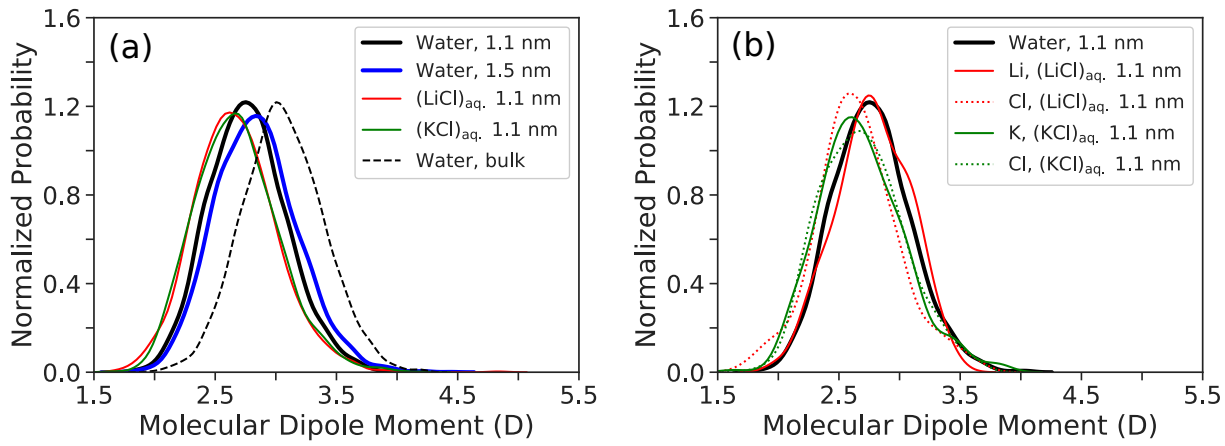

Figure 5.4: (S8) Molecular dipole moment distributions of all confined aqueous solutions for (a) the molecules outside ion solvation shells (non-SS) and molecules of pure water for 1.1 and 1.5 nm nanotubes and (b) molecules within the first solvation shell (SS) in the 1.1 nm nanotube.

with a greater reduction in the smaller tube (9% and 7%, for 1.1 nm and 1.5 nm CNTs respectively). A better understanding of this reduction may be inferred from Fig. 5.5 (left panel), where we present the radial dependence of the water dipole moment, which is shown to decrease as a function of the distance from the tube center. In particular, we found that dipole moments of water molecules in the interior of the 1.5 nm CNT remain close to those of bulk water, while the molecules belonging to the interfacial region exhibit a monotonic reduction of their dipole moment, as a function of the distance from the interface. In the case of the 1.1 nm CNT, all molecules are interfacial and exhibit a significant reduction of their dipole moment at all distances from the interface, except for a limited number of molecules residing the closest to the center of the CNT. Overall, our results for confined liquid water are consistent with those of Ref. [49].

Interestingly, we found that the changes of the molecular polarizability of water molecules under confinement are more complex than those of the dipole moment. We found that the average water polarizability in the 1.1 nm CNT, where all water molecules are interfacial, is enhanced by ~3% relative to the bulk value, whereas the average water polarizability in the 1.5 nm CNT is unchanged relative to bulk (Fig. 4.7, right panel). The radial dependence

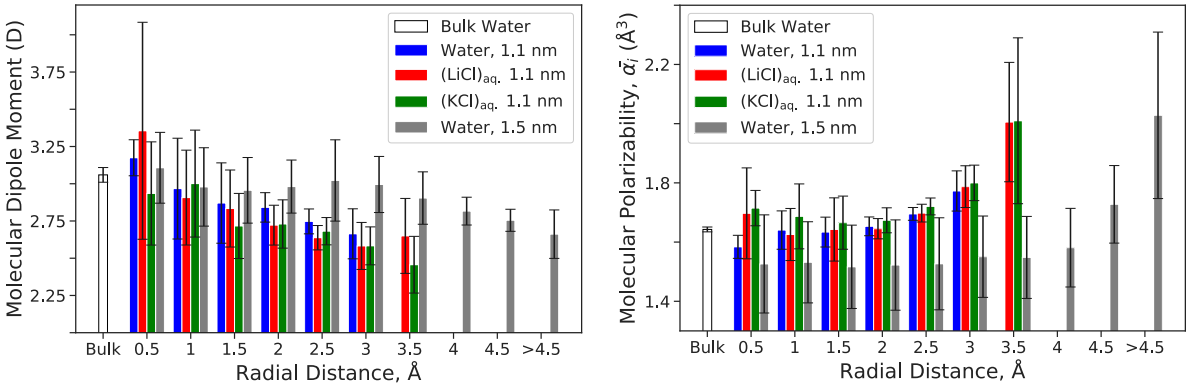

Figure 5.5: Left panel: The radial dependence of molecular dipole moments of water molecules in confined aqueous solutions. Right panel: The radial dependence of the average molecular polarizability of water molecules in confined aqueous solutions. All distances are measured along the nanotube axis, from the tube center, and distance on the abscissa are the results of a histogram with bins of width 0.5 Å.

of the molecular polarizabilities is shown in Fig. 5.5 (right panel), where all systems exhibit enhancement at the interface. Molecular polarizability in the 1.5 nm CNT is being balanced between lower interior polarizabilities (by ~15% relative to bulk) and enhanced ones (by ~23% relative to bulk) in the interfacial region.

To further understand the change in the water molecular polarizability under confinement, we considered the cartesian components of α_i: α_i^{XX}, α_i^{YY}, and α_i^{ZZ}, where X, Y and Z denote the axes of the simulation cell (Fig. 5.6). We found that α_i^{ZZ} is primarily responsible for the reduction of $\bar{\alpha}_i$ in the interior of the 1.5 nm CNT as well as the enhancement in the interfacial region; specifically, α_i^{ZZ} increases by ~88% between interior and interfacial water molecules, compared to a value of ~14% obtained for the other components. In addition, our results show that while α_i^{ZZ} is the most affected component in the 1.1 nm CNT as well, the anisotropy between the three polarizability components is much weaker than for the 1.5 nm CNT.

In order to investigate the reasons for the enhancement of α_i near the interface, we computed dipole moments and molecular polarizabilities in the presence and absence of the confining CNT, for the same exact configurations obtained from simulations where the

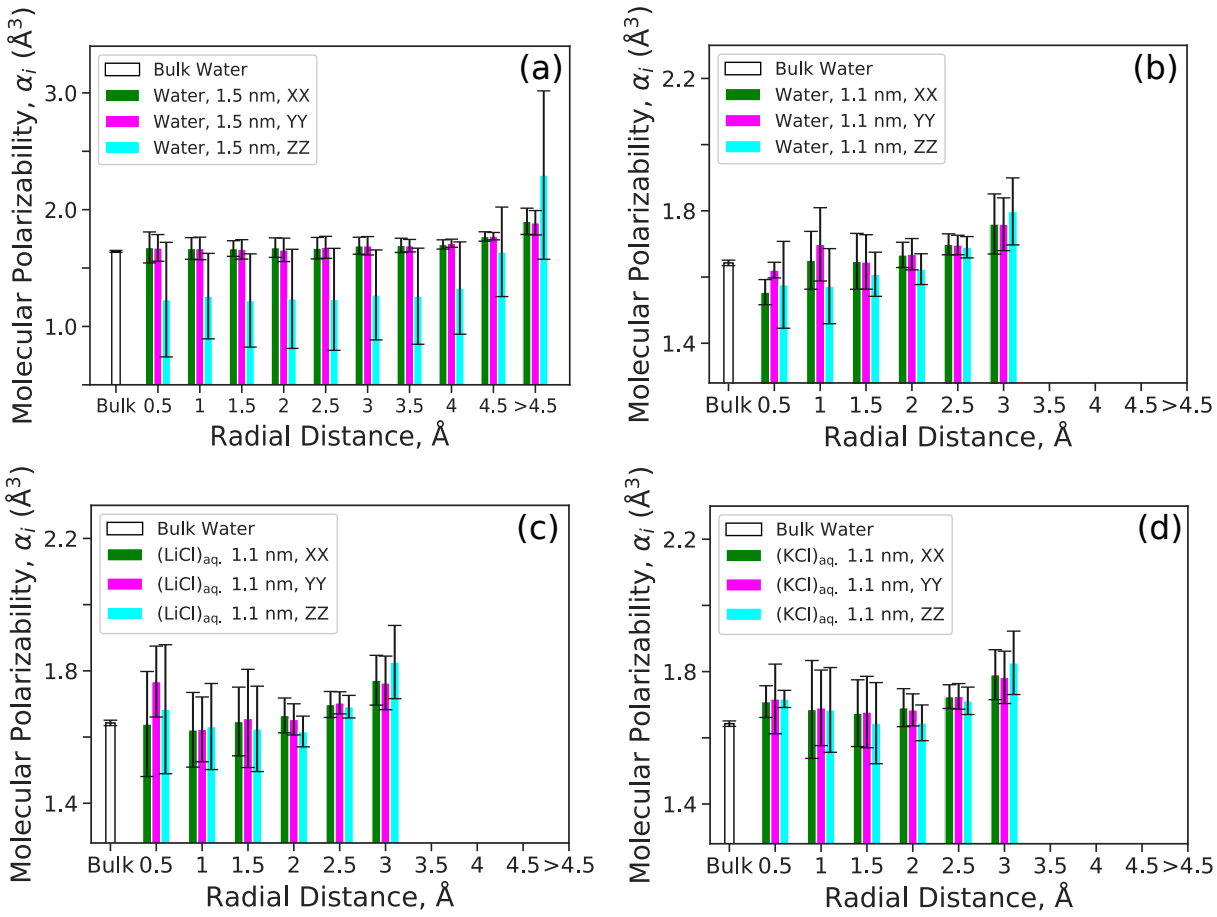

Figure 5.6: (S9) Radial dependencies of molecular polarizability decomposed into system coordinates for (a) 1.5 nm confined water, (b) 1.1 nm confined water, (c) $(LiCl)_{aq.}$ 1.1 nm solution, and (d) $(KCl)_{aq.}$ 1.1 nm solution. For better visualization of trends, (a) is plotted with a larger range of α_i than (b-d).

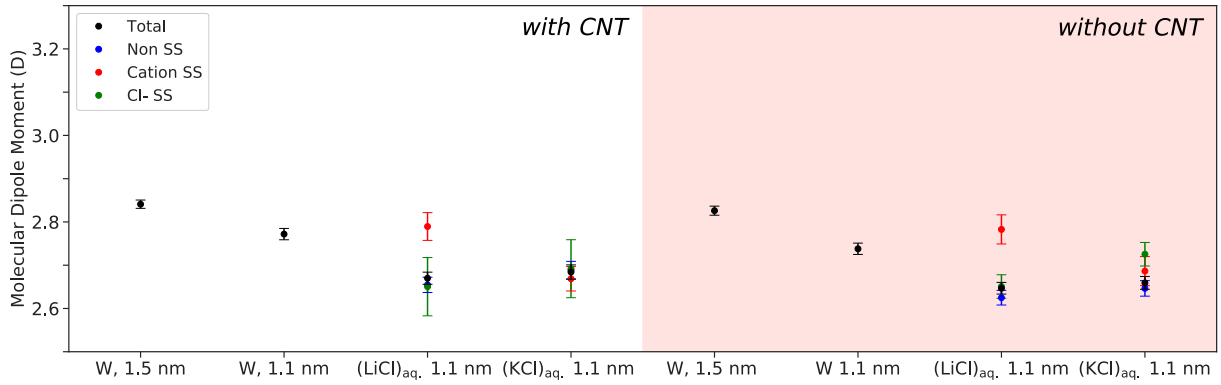

Figure 5.7: (S10) Dipole moments of water molecules in the confined solutions. The points in the unshaded region are reproduced from Fig. 4.4, while the data in the shaded region correspond to the same solutions, where dipole moments were computed without the nanotube present. "Cation SS" and "Cl^- SS" denote water molecules within the first solvation shell of the cation and chloride, while "Non SS" denotes all water molecules outside the first solvation shell of the ions. In the abscissa: "W" denotes pure water.

CNTs are present. We found that the dipole moments are unchanged by the presence of the confining surface (see Fig. 5.7), indicating that the reductions of dipole moments under confinement are driven by changes in the water structure, i.e. broken hydrogen bonds, and not by interfacial effects. The results for molecular polarizability are given in Fig. 5.8, showing significant reductions of ~0.1 $Å^3$ in all solutions when the CNT is absent: molecular polarizabilities are reduced by ~6-7% relative to bulk values. These results indicate that the variation in the water polarizability confined in a CNT is due to competing structural and interfacial effects. In particular, the polarizability decreases relative to bulk water, due to broken hydrogen bonds at the interface; such a decrease is counterbalanced by that of the interaction with the confining surface, which is responsible for a polarizability increase. In the 1.1 nm CNT case, where all water molecules are at the interface, the effect due to the interaction with the CNT is dominant, leading to an overall increase of the molecular polarizability in confinement. In the 1.5 nm CNT case, the balance of interfacial and broken hydrogen bond effects lead to the same average polarizability as in the bulk.

Overall, our findings on water dipole moment and polarizabilities point to important effects of nanoconfinement on the electronic properties of liquid water. These results are

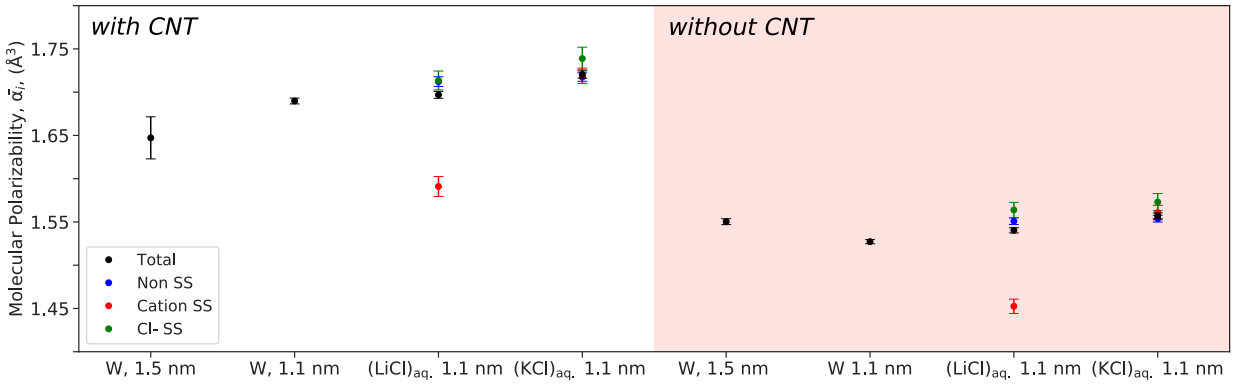

Figure 5.8: Average molecular polarizability, $\bar{\alpha}_i$, of water molecules in confined solutions. The points in the unshaded region are reproduced from Fig. 4.7, while the data in the shaded region correspond to the same solutions, where polarizabilities were computed in the absence of the CNT. "Cation SS" and "Cl^- SS" denote water molecules within the first solvation shell of the cation and chloride, while "Non SS" denotes all water molecules outside the first solvation shell of the ions. In the abscissa: "W" denotes pure water.

further corroborated by investigating the band gap of confined liquid. In particular, we obtained a value of 3.87 (0.06) eV and 3.88 (0.04) eV for water confined in the 1.1 nm and 1.5 nm CNTs, respectively, by using 200 water snapshots extracted from the simulations. Here, the numbers reported in parentheses are limits of the 95% confidence error using the Student's T-test. The band gaps under confinement are reduced by less than 10% relative to that of bulk water, consistent with other studies that found reductions of the water's band gap at the surface of the liquid[87]. We note that the absolute value of the computed gaps largely underestimates experimental values due to the limitation of the PBE functional; however we expect to obtain the same trends at higher levels of theory. [203, 90] Finally, we found that the gaps obtained using the whole systems, inclusive of the tube, yielded an additional reduction due to the hybridization between water and carbon states, and to carbon states falling in the gap of the liquid.

5.3.3 Confined ion solutions

We now turn to examine the combined effects induced by the presence of solvated ions and confinement on water by examining LiCl and KCl solutions in the 1.1 nm CNT. We found that Li^+ resides closest to the tube center, followed by K^+ and Cl^- (see Fig. 5.1). In addition, we found clear evidence of ion disruption to the dipolar orientations of liquid water reported in the previous section. In particular, we found that the dipole-dipole angle distribution of both confined salt solutions has a reduced intensity at low angles (e.g. higher dipolar alignment) relative to pure water. The presence of ions also decreases the hydrogen bond lifetime in the confined solutions (Fig. 5.9). These results are consistent with experimental X-ray diffraction studies by Ohba et al. [185], who attributed increased intermolecular water distances and weakened hydrogen bonding of NaCl solutions in 2 nm diameter CNTs to the disruption introduced by the solvated ions. Our findings are also supported by recent classical MD simulations on Na^+, K^+, and Cl^- ion solutions confined in CNTs of diameters up to ~1 nm [109], which found disruptions to the hydrogen bond structure across all ions.

The confinement of pure water at 1.1 nm caused a reduction of the average dipole moment by ~9% relative to the bulk. We find that this reduction is enhanced by the presence of solvated ions, as the dipole moment of water molecules outside the first cation solvation shell is reduced by ~13% and ~12% relative to pure bulk for the LiCl and KCl solutions, respectively. This is consistent with the structural modifications leading to smaller dipolar alignments and disrupted hydrogen bonding due to the ions. Similarly, while $\bar{\alpha}_i$ of pure water at 1.1 nm was enhanced by ~3% relative to bulk water, in the LiCl and KCl solutions polarizabilities were both enhanced ~4%. These results show that at the concentration considered here, the solvation of ions moderately amplifies the effects of confinement on dipole moments and molecular polarizabilities. Furthermore, given the similar effects found for LiCl and KCl, these results suggest minimal effects of the cation identity (e.g. Li^+ vs K^+) past the first solvation shell, consistent with our findings for the bulk solutions. Our results also show that the effect of counterions on the water structure is more complex under

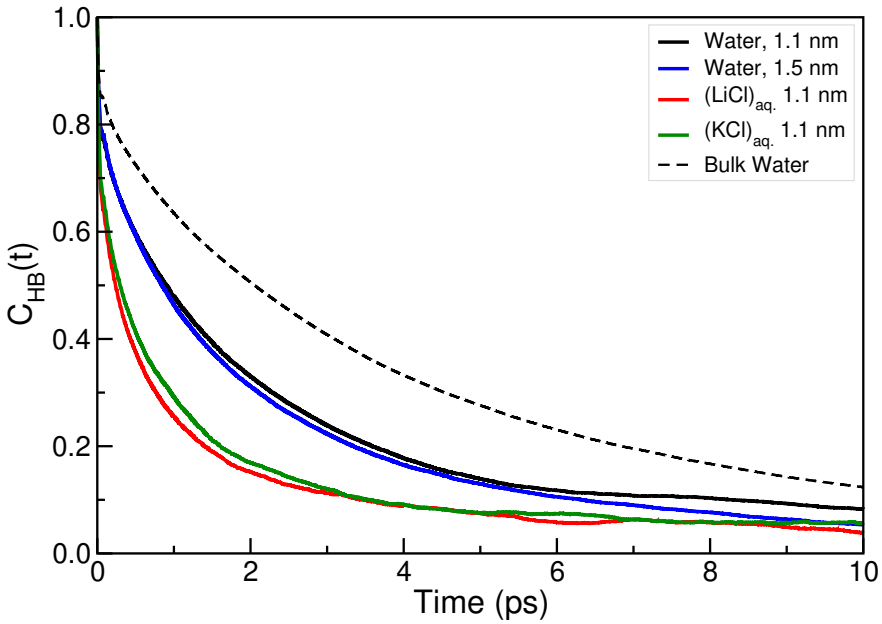

Figure 5.9: (S11) The hydrogen bond existence correlation functions for confined ion solutions (solid lines) and bulk water (dashed lines). Here, $C_{HB}(t)$ is the hydrogen bond existence correlation function, $\frac{\langle h(t)h(0)\rangle}{\langle h\rangle}$, where h is 1 when a tagged species in the system is hydrogen-bonded or 0 if it is not.

confinement. While the introduction of Cl^- in the bulk solutions reduces the polarizability of water molecules, we do not observe any reduction in the case of confined solutions.

Notably, we find that the Li^+ solvation shell is structurally resilient under confinement, maintaining a tight tetrahedral coordination. The structural resilience of the confined Li^+ solvation shell was recently reported by using experimental XRD [129], finding that the hydration number of Li^+ in 2 nm CNT to be much more bulk-like than that of larger cations. We also found that the water dipole moment in the Li^+ solvation shell (see Fig. 4.4, right panel) under confinement is similar to the bulk; specifically, the water dipole moment is enhanced in the first solvation shell relative to the rest of the liquid. Likewise, the qualitative behavior of the polarizability of the Li^+ solvation shell molecules (see Fig. 4.7, right panel) is similar to that of the bulk: $\bar{\alpha}_i$ is suppressed relative to its non-SS counterpart.

In the case of K^+ and Cl^- under confinement, we find that K^+ and Cl^- are desolvated relative to the bulk. In particular, the oxygen coordination of K^+ decreases from 6.8 in the

bulk to 5.4. under confinement, whereas that of Cl^- decreases from 6.0 to 4.7 and 5.5 in the KCl and LiCl solutions, respectively. In contrast to Li^+, for these larger ions, we found no difference in the dipole moment between water inside and outside the first ion solvation shell. This differs from their corresponding bulk behavior, where water dipole moments in the K^+ and Cl^- solvation shell are reduced relative to the bulk value. Similarly, the $\bar{\alpha}_i$ of water molecules in the first solvation shell of K^+ is indistinguishable from that of non-SS water molecules, again in contrast to the bulk behavior. Collectively, we found that water molecules in the solvation shell of Li^+ preserve their bulk patterns due to the rigidity of the ion solvation, whereas those belonging to the solvation shell of larger ions, do not.

5.4 Conclusions

We found that under confinement, two competing effects influence the value of the polarizability of water molecules: we observed a reduction due to broken hydrogen bonds, and an enhancement caused by the interaction of water molecules with the CNT interface. The latter dominates in the narrow CNT (1.1 nm) where all water molecules are interfacial, resulting in ~3% enhancement in the molecular polarizability relative to bulk water. In the wider CNT (1.5 nm) that contains both interior and interfacial water molecules, the broken hydrogen bonds and interfacial effects offset each other, yielding a total polarizability unchanged from that of the bulk. We also note that, under confinement, the polarizability of water molecules is highly anisotropic, with enhancements and reductions observed primarily in the component of the polarizability along the nanotube axis. The effect of confinement also led to a small reduction of band gaps for both CNTs. We found that ion solvation leads to a slight amplification of confinement effects on water molecular polarizabilities and dipole moments in the 1.1 nm CNT. Several trends observed for properties of ion solvation in the bulk were found to be the same under confinement, including the local effect of cations. In addition, we found that the Li^+ solvation shell is structurally resilient under confinement, with similar modifications of water dipole moments and polarizabilities in the ion solvation

shell as in the bulk. In contrast, the larger cation K^+ is desolvated under confinement and does not maintain the bulk trends in ion solvation shell dipole moments and polarizabilities.

Overall, our findings demonstrate the sensitivity of molecular polarizability to the perturbation introduced by both solvated ions and confinement on liquid water. Our results highlight the importance of the inclusion of polarizability for realistic simulations of water in complex environments, and may assist with parameterization of future interatomic potentials.

CHAPTER 6

AB INITIO SPECTROSCOPY AND IONIC CONDUCTIVITY OF WATER UNDER EARTH MANTLE CONDITIONS

Reproduced in part from V. Rozsa, D. Pan, F. Giberti, and G. Galli, Proc. Nat. Acad. Sci. USA, 115 (27) 6952-6957, (2018).

6.1 Introduction

Water at extreme conditions plays a critical role in earth and planetary science. For example, ice has been proposed to exist in cold, subducting tectonic slabs at 10-20 GPa, bearing large reservoirs of water with immense impact on terrestrial geochemistry [24]. In addition, recent studies supported the existence of stable hydrous silicate minerals in the deep earth [182], and of local aqueous pockets in the upper mantle [271] where water is an important medium to transport oxidized carbon [128, 192]. At the fundamental level, high pressure and temperature create complex changes in the bonding and structural properties of water, eventually leading to dissociation, and many of these changes remain poorly characterized. One of the reasons stems from experimental difficulties in probing the liquid at extreme conditions, including water's reaction with metals present in the experimental apparatus, high corrosiveness of the liquid, and other limitations of current high-pressure experimental techniques. Available measurements of water at extreme conditions are mostly limited to vibrational spectroscopy and conductivity, obtained in static and shock-wave high pressure experiments. On the theoretical side, spectroscopic signatures and ionic transport may not be studied with simple classical simulations, due to the presence of complex dissociation processes. Hence, their investigation calls for the use of quantum mechanical calculations, which are usually rather demanding from a computational standpoint. To this date there have been few ab initio simulations of high pressure water encompassing structural, vibrational and transport properties (e.g. ionic conduction); for example no vibrational spectra

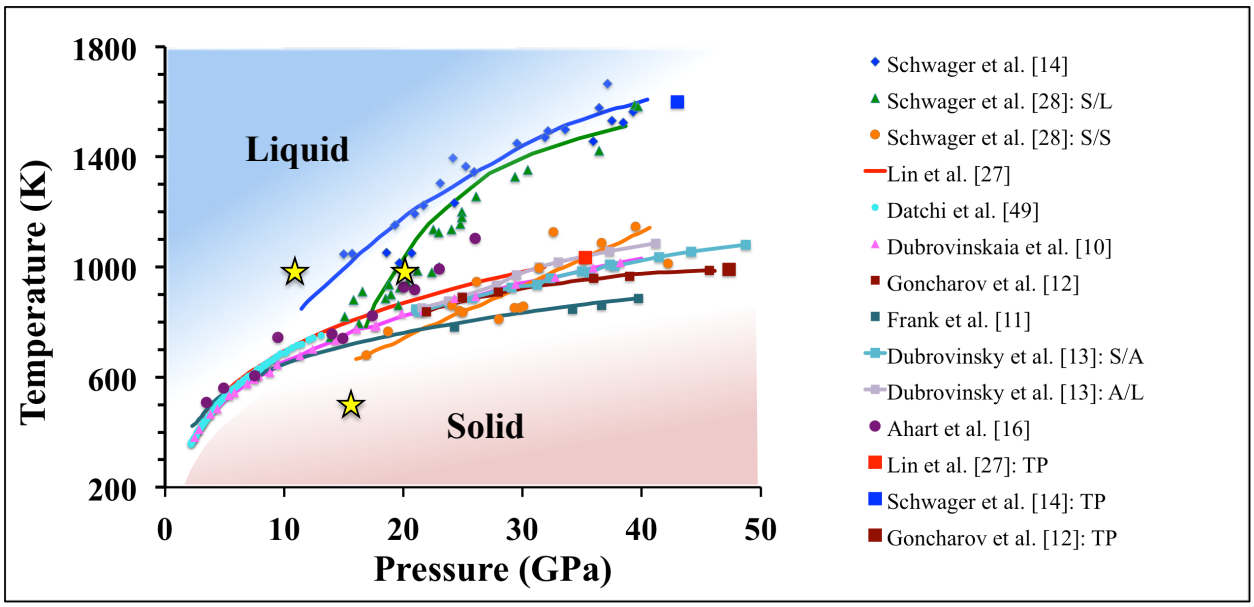

Figure 6.1: The phase diagram of water at high pressure (P) and temperature (T). All points are experimental data, marking the ice VII/liquid transition unless otherwise specified. Other points mark the proposed ice VII/solid (S/S), solid/liquid (S/L), solid/amorphous (S/A), and amorphous/liquid (A/L) transitions. Proposed triple points (TP) of ice VII, liquid, and ice X phase are marked as squares. The (P,T) conditions investigated in this work are marked with yellow stars.

have been computed for the fluid close to the ice VII melting line, and water conductivity has been investigated primarily at conditions well above 20 GPa. [37, 97, 79, 78].

Overall the water phase diagram at high pressure is still poorly known, with many controversial results present in the literature, e.g. regarding the location of the melting line in the region of 10-50 GPa (see Fig. 6.1). A number of experimental studies [65, 74, 98, 66] indicate the presence of a melting line near 700 K at 20 GPa, almost 400 K lower than previously reported[235, 238]; however, the most recent measurements proved to be inconclusive in fully resolving the discrepancy[4]. In addition, three markedly different locations for the triple point of the liquid, ice VII, and ice X have been proposed in the literature[68], differing by 500 K and 10 GPa. The structural and dynamical properties of the fluid close to melting are also not well established, with ongoing debates on many fronts, including the existence of plastic ice phases close to the ice VII melting line [261, 8], the molecular or dissociative

nature of water [122] and the primary mechanism of ionic conduction [78, 60]. Some studies suggested a unimolecular dissociation process [114, 97, 285, 80, 99], $H_2O \longrightarrow H^+ + OH^-$ occurring above 10 GPa and 1000 K, while others pointed at the existence of bi-molecular dissociation [237, 98, 79], i.e. $2\,H_2O \longrightarrow H_3O^+ + OH^-$ similar to low pressure, with some experiments being unable to corroborate either mechanism[151]. Likewise the interpretation of vibrational spectra [98, 114] of high pressure water remains controversial.

To shed light on the water phase diagram between 10 and 20 GPa, we carried out a series of ab initio simulations aimed at characterizing the structure of the fluid, its vibrational spectra and the mechanism of ionic conduction. We focused on three specific (P, T) conditions, including one (11 GPa and 1000 K) where the system is believed to be a fluid according to all experiments, and for which measured Raman spectra are available, and another condition (20 GPa and 1000 K) characterized as either solid or liquid by different measurements. We also considered an amorphous phase, quenched from the liquid (16 GPa, 500 K), to compare vibrational signatures of fluid and disordered solid water in a similar pressure range. We computed ab initio molecular dynamics trajectories of length ∼240 ps at each of the (P, T) conditions. Our results are consistent with the most recent estimates [98, 66] of the location of the water melting line between 11 and 20 GPa; our simulations provide a detailed microscopic picture of the fluid, including dissociation mechanisms, and the origin of its high conductivity above 10 GPa.

In section 6.2, we discuss he computational methods in our simulations of high P/T aqueous solutions. In section 6.3, we present the results and analysis of our simulations, including structure/diffusion analysis, various vibrational spectra, and ionic conductivity calculations. We offer conclusions in section 6.4.

6.2 Computational Methods

We performed ab initio MD simulations in the Born–Oppenheimer approximation with the PBE exchange-correlation functional [198] and the Qbox code [1]. The choice of the PBE

functional was motivated by the good agreement with experiment found for the fluid equation of state at high pressure [192, 193, 194].

We used norm-conserving pseudopotentials [273] (http://fpmd.ucdavis.edu/potentials/), with a plane wave basis set and kinetic energy cutoff of 85 Ry, which was increased to 220 Ry for pressure calculations. The densities of water were 1.57 g/cm^3 and 1.86 g/cm^3, computed at 1000 K to correspond to pressures of 11 and 20 GPa, respectively. Our simulation supercell was cubic, with 64 water molecules. Molecular dipole moments were calculated using maximally localized Wannier function centers[280, 103]. Temperature was controlled with the stochastic velocity rescaling method [33]. Simulation timesteps were 5 au (0.121 fs), while the thermostat time was 121 fs. In the interest of computational time, the full computation of DFPT-based polarizabilities was performed every 25 MD steps. Trajectories were collected for $\sim$240 ps at each pressure, after initial equilibration of $\sim$10 ps.

6.3 Results and Discussion

6.3.1 Structure and Diffusion

We first determined whether water is solid or liquid at the conditions chosen in our study by computing diffusion coefficients from the mean squared displacement of oxygen and hydrogen (see Fig. 6.2A and Table 6.1). We found that at 1000 K, both at 11 and 20 GPa, water is a liquid. Hence our results are consistent with the melting line reported by Lin, et al [151] but not with studies which classified water as solid at these conditions, where the system was suggested to be either in the ice VII [235] structure or adopt a new, unspecified crystalline phase [234]. We found that the quenched phase at 16 GPa/500 K is instead non-diffusive and we classified it as solid-like. A summary of the thermodynamic conditions and computed diffusion coefficients is given in Table 6.1.

At 20 GPa/1000 K, we found that hydrogen diffuses twice as fast as oxygen. Clear evidence of the dissociation processes occurring in the liquid emerges from the analysis

ρ (g/cm^3)	T (K)	P (GPa)	D_O (cm^2/sec)	D_H(cm^2/sec)
1.57	1020 ± 50	11 ± 1	~9x10^{-5}	~9x10^{-5}
1.86	1020 ± 51	20 ± 1	~3x10^{-5}	~7x10^{-5}
1.86	510 ± 25	16 ± 1	nondiffusive	nondiffusive

Table 6.1: Density (ρ), computed temperature (T), pressure (P) and oxygen (D_O) and hydrogen (D_H) diffusion coefficients for three first principles molecular dynamics trajectories. Averages were computed over 240 ps.

of radial distribution functions (RDF), e.g. a significant intensity of the O-H RDF (Fig. 6.2B) near its first minimum. Further evidence of molecular dissociation is in the RDF between oxygen atoms and maximally localized Wannier function centers (Fig. 6.2C). The latter represent centers of charge in the system. There are four centers associated to an intact water molecule, with two lone pairs and two bond pairs located within O-H covalent bonds. The non-negligible intensity in correspondence of the minimum between lone and bond pair distributions is a signature of proton transfer. We directly observed dissociation and proton transfer events in our simulation, with frequent creation of short-lived (¡ 10 fs) ionic products of bi-molecular dissociation events, consistent with earlier studies [237, 40]. While the most commonly observed ionic species are simple hydronium and hydroxide (6.3A), we also detected the formation of larger transient ionic species, as defined by simple distance cutoffs. Many of them are "Zundel" ($H_5O_2^+$) ions (Fig. 6.3B). Our observations of transient multimolecular ionic species differ from the hypothesis of unimolecular dissociation, which would imply the existence of free protons [114, 97, 285, 80].

Interestingly, at both 11 and 20 GPa the fluid exhibits a distinct second coordination shell in the O-H RDF. This indicates that intermolecular hydrogen bonding persists at these conditions, despite molecular dissociation and proton transfer events. The location of the second peak of the O-H distribution is sensitive to pressure, varying from 1.75 Å at 11 GPa to 1.62 Å at 20 GPa. In contrast, the maxima of the first coordination shell are in similar locations at both pressures, confirming the insensitivity of water's first coordination shell to compression, as noted by other authors [29].

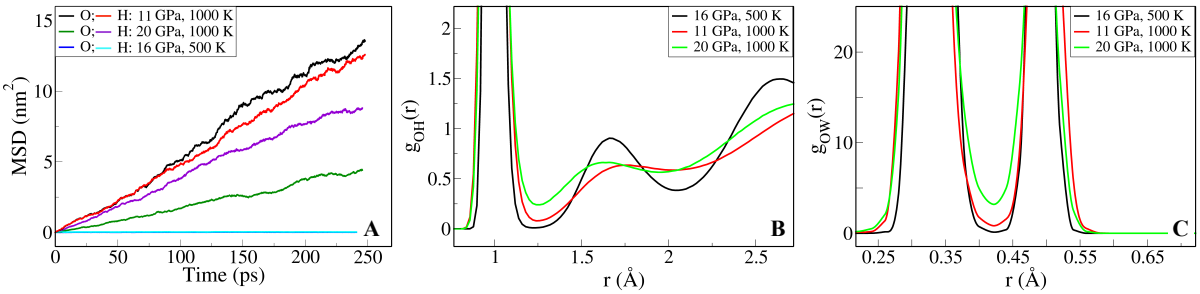

Figure 6.2: A) The mean squared displacement of oxygen/hydrogen at 11 GPa/1000 K, 20 GPa/1000 K, and 16 GPa/500 K. B) The Oxygen-Hydrogen radial distribution functions. C) The Oxygen-MLWF radial distribution functions.

6.3.2 Ionic species and Ionic Lifetimes

We analyzed the presence of ionic species in compressed water as a function of time for the ∼11 and ∼20 GPa trajectories (see Table 6.1). Ionic species were defined using criteria based on hydrogen bonding analysis. We defined a hydrogen and an oxygen atom as hydrogen bonded when the distance between them is less than the second minimum of the OH radial distribution function (RDF) and the deviation of the O – H...O angle from a straight line is $< 30°$[155]. Here O – H denotes a covalent bond and H...O an hydrogen bond. Using this definition, we constructed the hydrogen bond network of each snapshot of our trajectories, and then mapped the network onto a graph, with oxygens as vertexes and hydrogen bonds as direct connections between pairs of vertexes.

In this framework, a hydronium ion, composed of three hydrogens and a central oxygen, was identified as a chemical species donating three hydrogen bonds to its vicinal neighbors. A hydroxide ion, composed of one hydrogen and one oxygen, was identified as a chemical species donating one hydrogen bond while accepting three or more hydrogen bonds. This strategy has also been used to identify constituent ions in water at ambient conditions [94].

The variation of the number of hydronium and hydroxide species over two short trajectories at 11 and 20 GPa is plotted in Fig. 6.4, where the number of the two species has been represented in different quadrants for clarity. The formation of $H3O^+$ and OH^- is clearly

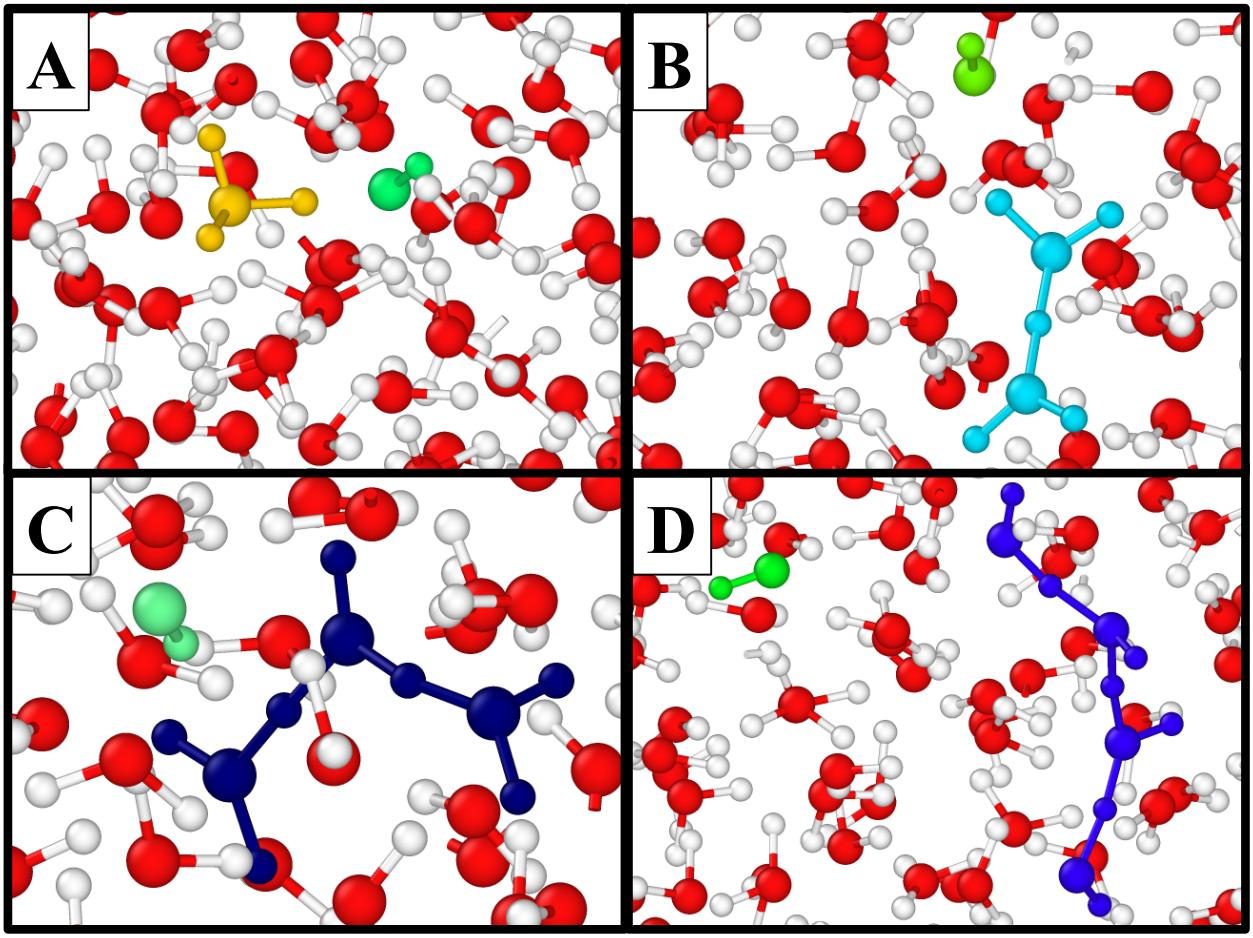

Figure 6.3: Snapshots of configurations extracted from molecular dynamics trajectories at 20 GPa and 1000 K, showing short-lived ionic species. Color coding of ionic species is based on a distance cutoff corresponding to the first minimum of the O-H radial distribution function. Hydroxide ions are shown in green. A) A hydronium (yellow) /hydroxide pair, formed after a bi-molecular dissociation event B) A Zundel-like $H_5O_2^+$ species (cyan) with a nearby hydroxide C) A $H_7O_3^+$ species (dark blue) with a nearby hydroxide D) A $H_7O_4^-$ species (blue) and an hydroxide ion.

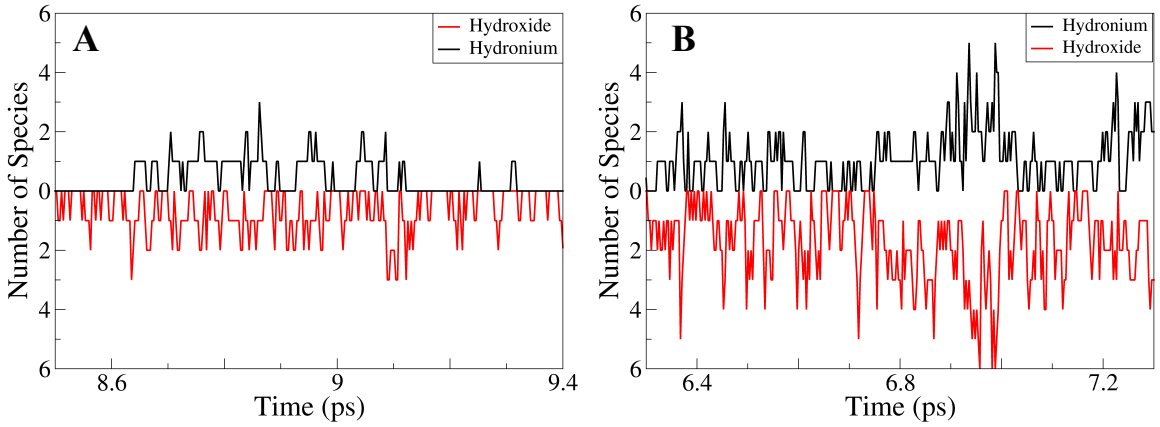

Figure 6.4: Number of ionic species along a short 11 (A) and 20 (B) GPa trajectory (see text for definition of hydronium and hydroxide ions).

correlated, indicating that dissociation occurs as a bimolecular process. Fig. 6.4 shows a larger concentration of hydroxide and hydronium ions at 20 than at 11 GPa; the same trend was found over the entire trajectory. Thus we found that hydronium and hydroxide ions are formed in a highly correlated fashion

We also investigated whether "free hydrogens" were present in our simulations. For each hydrogen, at each step we calculated its coordination number with respect to oxygen. A hydrogen was considered "free" if its coordination was 0, i.e. no oxygen was present within a distance equal to the first minimum of the OH RDF. Then, for each free hydrogen, we counted the number of contiguous snapshots over which the hydrogen persists as a free species. We defined the lifetime, τ, of the free hydrogen as the time an hydrogen atom spends as a free species. We constructed an histogram of all computed τ. By normalizing the histogram with respect to the total number of snapshots and total number of hydrogens, we obtained the probability, at a given time step, to observe a free hydrogen with a lifetime τ. Fig. 6.5 displays the computed probabilities for two choices of cutoff distances for a 3 ps portion of the 20 GPa trajectory containing dissociation events. We found extremely small values of τ (<0.3 fs) with very low probabilities ($< 2\text{x}10^{-5}$). Hence our results show that

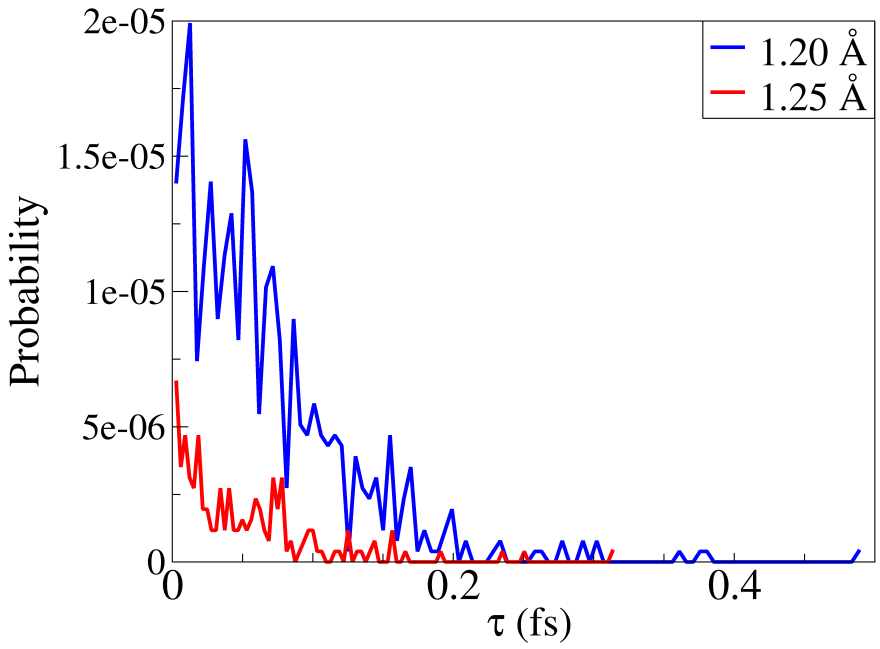

Figure 6.5: Probability to observe a free hydrogen as a function of lifetime τ (see text for definition) over a 3 ps trajectory at 20 GPa, 1000 K. We show results for two cutoff distances: 1.25 Å, corresponding to the first minimum of the O-H RDF, and a cutoff 4% percent smaller.

free hydrogens are fleeting species, with no evidence of long-lived free hydrogens arising from unimolecular dissociation.

In spite of its simplicity, the method adopted here to define free protons (using a cutoff distance) clearly indicates that isolated hydrogen ions are transient species, consistent with a bi-molecular dissociation mechanism. These rapid dissociation events occur in the liquid at both 11 and 20 GPa, with frequency increasing with pressure (see Fig. 6.4), consistent with the trend observed in RDFs.

6.3.3 Ionic Conductivity

In order to understand whether the short-lived hydronium, hydroxide, and more complex ions (see Fig. 6.3) found in our simulation act as charge carriers, we computed the ionic

conductivity of the fluid. Along the shock Hugoniot, the conductivity of water has been shown to rapidly increase by several orders of magnitude under pressure, before reaching a plateau on the order of 10 $(\Omega\text{cm})^{-1}$ above 30 GPa [176]. This increase has been interpreted as the result of increasing dissociation of water molecules [79], although the nature of the ionic species responsible for conduction was not determined and the ability of ionic species present in the fluid to effectively carry charge has been questioned in the literature [114, 60].

We computed ionic conductivities directly from first principles, without resorting to a-priori definitions of ionic charges, e.g. geometric partitioning, [172][79], Mulliken [97] or Born effective charges [78]. Avoiding approximate definitions of charges is key for obtaining unbiased and predictive results for ionic conductivities. We computed σ through Eq. 3.28. Instead of directly evaluating the integral of the correlation function of the total dipole moment derivative, we employed the Einstein relation, according to Eq. 3.29.

In order to minimize statistical errors in the evaluation of Eq. 3.29, we partitioned the trajectories over which $\mathbf{M}(t)$ was computed into many separate portions of length 10 ps. The results are shown in Fig. 6.6, where we also display the time progression of the average. As reported in the main text, we obtain $\sigma \sim 1$ $(\Omega\text{cm})^{-1}$ at 11 $\pm$1 GPa, 1000 K, and $\sigma \sim 10$ $(\Omega\text{cm})^{-1}$ at 20 $\pm$1 GPa, 1000 K. We note that the values of the conductivity computed over the 10 ps segments exhibited a standard deviation of the mean of 0.3 $(\Omega\text{cm})^{-1}$ at 11 GPa, 1000 K, and 1.0 $(\Omega\text{cm})^{-1}$ at 20 GPa, 1000 K. A comparison of the averages over partitions at both conditions is presented in Fig. 6.7, clearly displaying the higher conductivity of the water at 20 GPa. We also computed the ionic conductivities from the directly analogous method of Green-Kubo integration of Eq. 3.28 and report full consistency in our results (Figs. 6.8, 6.9.

Our estimates of σ are compared to other experimental [107, 176] and computational [97, 79] studies on the conductivity of water along the principal Hugoniot in Fig. 6.10. In Table 6.2 we also present the data corresponding to Fig. 6.10, including temperatures. While temperatures were not reported in Refs. [176] and [79], we obtained temperatures

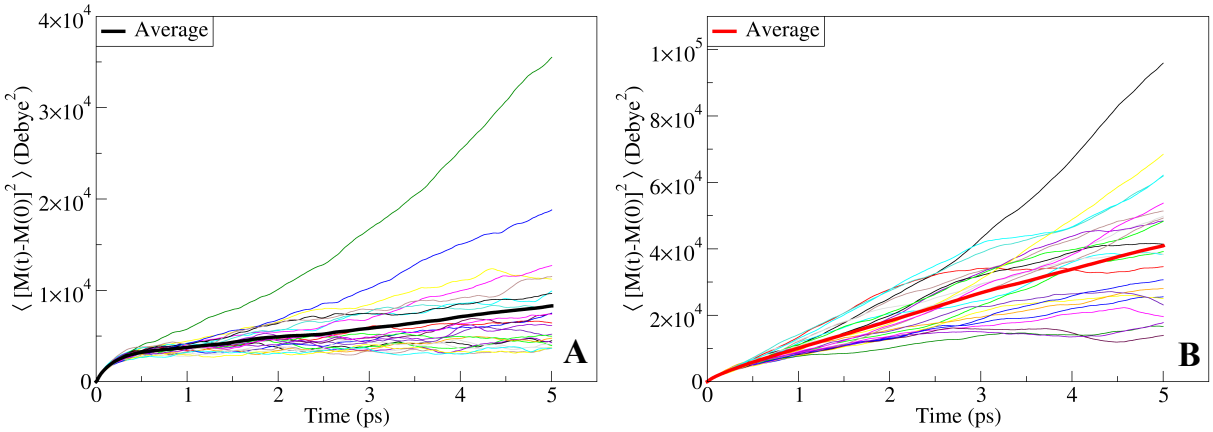

Figure 6.6: Time-averaged mean squared displacement of the total dipole moment **M** as a function of separation time for multiple partitioned segments of length 10 ps from a 240 ps trajectory at 11 GPa and 1000K (A) and 20 GPa and 1000 K (B). The average over segments for 11 GPa and 1000 K is reported as a thick black curve, yielding $\sigma \sim 1$ $(\Omega\text{cm})^{-1}$. Similarly, the average over segments for 20 GPa and 1000 K is reported as a thick red curve, yielding $\sigma \sim 10$ $(\Omega\text{cm})^{-1}$.

in both cases from closely related publications by the same authors. To the best of our knowledge this is the first study to compute the ionic conductivity of water entirely from first principles utilizing maximally localized Wannier functions. An equivalent approach employed by Cavazzoni, et. al [37] used the Berry Phase method at 30 to 300 GPa and 300 to 7000 K.

In order to minimize error arising from statistical noise [6], we obtained estimates of σ by partitioning the total trajectory over which $\mathbf{M}(t)$ was computed into shorter portions (of 10 ps each) and computing the ionic conductivity as an average (see Figs. 6.6 and 6.8). We obtain an estimate of $\sigma \sim 1$ $(\Omega\text{cm})^{-1}$ at 11 $\pm$1 GPa, 1000 K, and $\sigma \sim 10$ $(\Omega\text{cm})^{-1}$ at 20 $\pm$1 GPa, 1000 K. We report these values emphasizing their orders of magnitude, as multiple additional trajectories would be required for a more precise determination.

The values of σ obtained at 11 and 20 GPa along the 1000 K isotherm are six and seven orders of magnitude higher than at ambient conditions, respectively [149]. Fig. 6.10 shows how these estimates compare to previous experimental and computational reports of

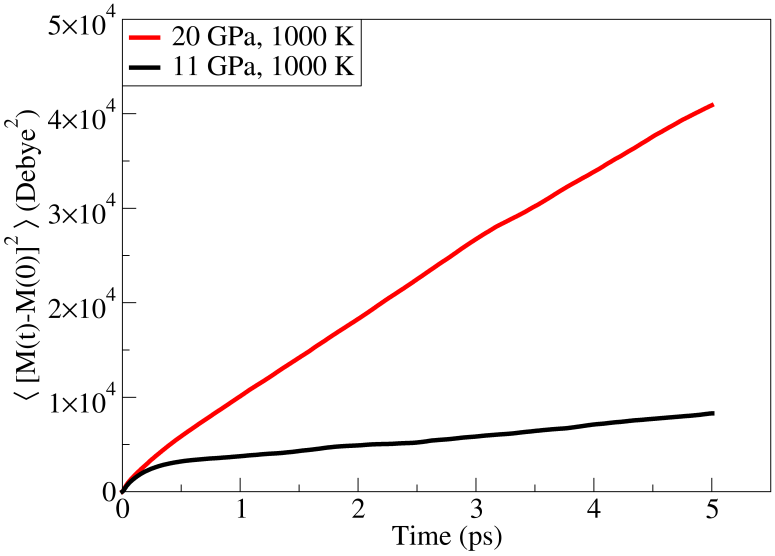

Figure 6.7: Comparison of the averages of time-averaged mean squared displacement of the total dipole moment **M** as a function of separation time for multiple partitioned segments of length 10 ps at 11 GPa and 1000 K and 20 GPa and 1000 K. The average over segments for 11 GPa, 1000 K is reported as a black curve ($\sigma \sim 1$ $(\Omega\text{cm})^{-1}$) while the average over segments for 20 GPa, 1000 K is reported as a red curve ($\sigma \sim 10$ $(\Omega\text{cm})^{-1}$)

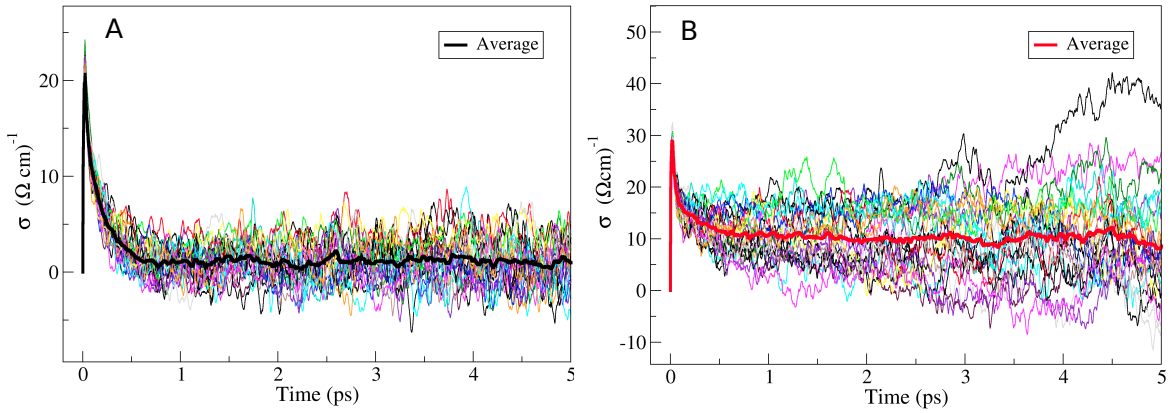

Figure 6.8: Green-Kubo integral values for σ from multiple partitioned segments of length 10 ps from a 240 ps trajectory at 11 GPa and 1000K (A) and 20 GPa and 1000 K (B). The average over segments for 11 GPa and 1000 K is reported as a thick black curve, yielding $\sigma \sim 1$ $(\Omega\text{cm})^{-1}$. Similarly, the average over segments for 20 GPa and 1000 K is reported as a thick red curve, yielding $\sigma \sim 10$ $(\Omega\text{cm})^{-1}$.

Study	P (GPa)	T (K)	σ ($(\Omega\text{cm})^{-1}$)
Hamann et al. [107]	5.4	547	0.00076
	8.3	731	0.04
	12.1	991	0.56
	16.7	1326	2.3
	21.9	1710	7.1
Mitchell et al. [176]	28.0	1790	14
	35.0	2200	28
	46.0	3030	19
	47.0	3090	18
	59.0	3810	29
Goldman et al. [97]	18.2 ± 0.2	791 ± 7	6.0 ± 2
	26.5 ± 0.4	1167 ± 4	7.2 ± 3
	42.0 ± 0.3	1995 ± 8	7.9 ± 3
	53.8 ± 0.3	2744 ± 10	11.2 ± 4
	67.8 ± 0.2	3654 ± 6	11.1 ± 4
French et al. [79]	14.8	1010	2 ± 1
	23.5	1550	11 ± 4
	30.9	2000	25 ± 7
	46.8	3010	47 ± 10
	62.9	4040	122 ± 26
This study	11 ± 1	1020 ± 50	∼1
	20 ± 1	1020 ± 51	∼10

Table 6.2: Pressure (P), temperature (T), and conductivity (σ) of water along the principal Hugoniot, as displayed in Fig. 6.10. Temperatures for Mitchell et al. [176] were obtained from the same group's later study, reported in Ref. [157]. Temperatures for French et al. [79] were obtained from the same group's earlier study, reported in Ref. [80].

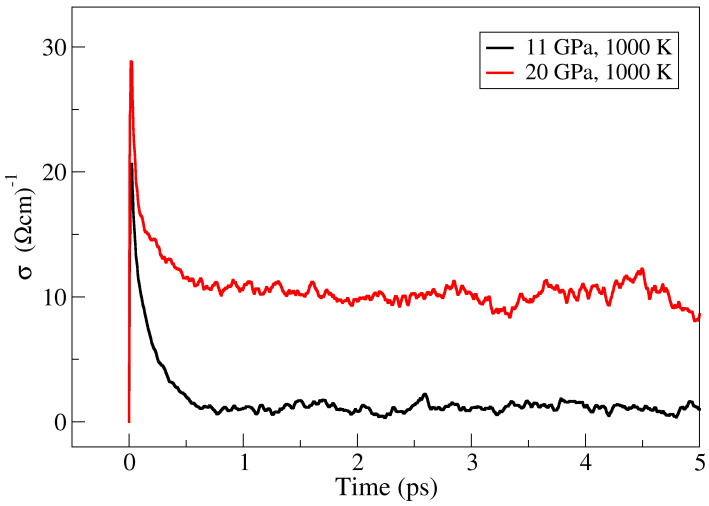

Figure 6.9: Comparison of the averages of Green-Kubo integrals for multiple partitioned segments of length 10 ps at 11 GPa and 1000 K and 20 GPa and 1000 K. The average over segments for 11 GPa, 1000 K is reported as a black curve ($\sigma \sim 1$ $(\Omega\text{cm})^{-1}$) while the average over segments for 20 GPa, 1000 K is reported as a red curve ($\sigma \sim 10$ $(\Omega\text{cm})^{-1}$)

water's ionic conductivity along the principle Hugoniot. We note that our data are on the 1000 K isotherm, while the Hugoniot includes temperatures such as 990 K at 12 GPa, and 1710 K at 22 GPa [107]; a full comparison of data from Fig. 6.10, including temperatures, is presented in Table 6.2. Our finding of an order of magnitude increase in conductivity between 11 and 20 GPa is consistent with experimental reports of orders of magnitude increases in conductivity along the Hugoniot, which were attributed to autoionization of water[107, 176]. Our estimates of σ are also consistent with computational results obtained using approximations based on Mulliken charges ($\sigma = 6 \pm 2$ $(\Omega\text{cm})^{-1}$ at 18.2 $\pm$0.2 GPa, 790 K)[97]. They are also consistent with other computational results, which computed σ using a generalized Einstein formulation for diffusion coefficients of unbound protons ($\sigma = 2 \pm 1$ $(\Omega\text{cm})^{-1}$ at ~15 GPa, 1010 K, and $\sigma = 11 \pm 4$ $(\Omega\text{cm})^{-1}$ at ~24 GPa, 1550 K)[79]. Unlike both of these computational studies, we emphasize that our estimates required no a-priori assumptions about the effective charge transported. Our findings indicate that the large

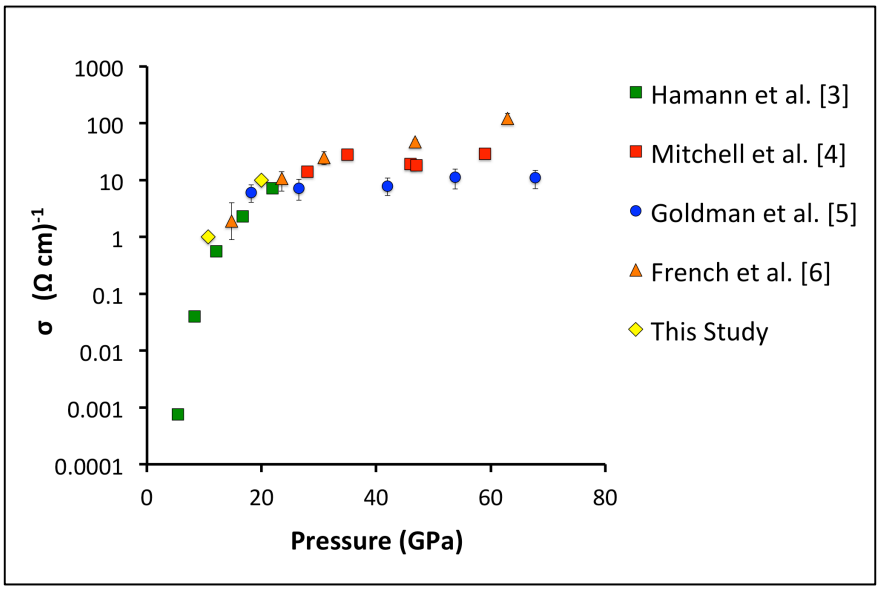

Figure 6.10: The ionic conductivities of water as a function of pressure, along the principal Hugoniot. Hamann et al. [107] and Mitchell et al. [176] reported experimental shock studies. Goldman et al. [97] reported a computational study of shocked water, using Mulliken charges, and French et al. [79] reported a computational study using diffusion coefficients of free protons. Temperatures for all data points are presented in Table 6.2
.

increase in conductivity near the melting line is related to the existence of the short-lived and fast-recombining hydroxide/hydronium and more complex ionic species that are effective charge carriers.

A strong argument against bi-molecular dissociation at high pressure, originally raised in Ref. [114], is the lack of a spectroscopic signature of hydronium in measured Raman spectra, near the O-H stretching peak at $2900\ \mathrm{cm}^{-1}$. It was later suggested that the missing signature could be due to the short lifetime of hydronium ions, leading to a broad peak, difficult to identify [237]. In order to address this controversy, we computed the Raman spectra of water at 11 and 20 GPa, explicitly searching for vibrational signatures of the short-lived ionic species identified from the analysis of our MD trajectories.

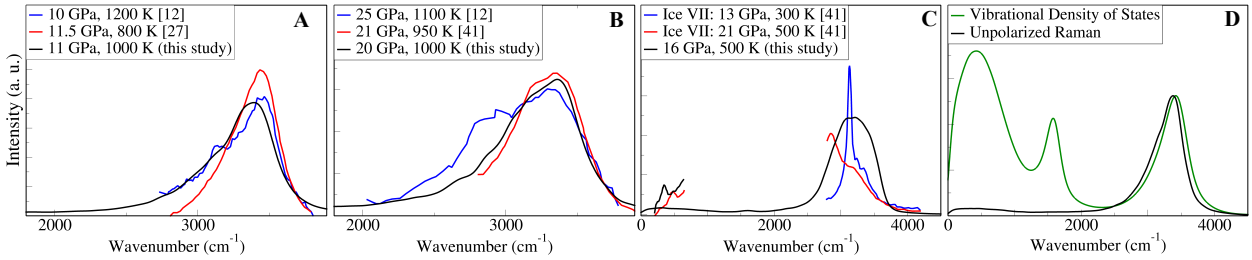

Figure 6.11: A) Computed unpolarized Raman spectrum at 11 GPa, 1000 K compared to experiment [98, 151]. B) The unpolarized Raman spectrum at 20 GPa, 1000 K compared to experiment [98, 150]. C) Computed unpolarized Raman spectrum of amorphous water at 16 GPa, 500 K compared to the experimental spectrum of ice VII [150]. D) Computed unpolarized Raman spectra at 11 GPa, 1000 K compared to the vibrational density of states.

6.3.4 Raman Spectra

Raman spectra were computed as the Fourier transforms of the time correlation function of the system's polarizabilities, obtained from density functional perturbation theory [15], as implemented in the Qbox code[275, 1]. Here we focus on unpolarized Raman spectra, for which measurements are available [114, 98, 151, 150]. Isotropic and anisotropic Raman spectra were computed using Eqs. 3.21 and 3.22. We cast the expression of the Raman intensities in terms of effective molecular polarizability using Eqs. 3.25 and 3.26 By separating $i = j$ and $i \neq j$ terms of the summation, we obtain the intramolecular and intermolecular contributions to the Raman intensity, respectively. Additional details are given in Section 3.3.3.

Our results in the O-H stretching region are compared to experiment in Fig. 6.11 and show good agreement. The low frequency part of the spectrum was omitted since the measured one is featureless. Our simulations reproduce two key trends observed under pressure: the considerable decrease in the O-H mode intensity (Fig. 6.12A, B), and a redshift of 70 cm^{-1} between 11 and 20 GPa at 1000 K. This comparison represents a crucial validation of the model of the fluid derived in our ab initio simulations. We note that the computed spectra reported in Fig. 6.11 and Fig. 6.12A, B represent the first available Raman spectra of high pressure water over the full 0-3000 cm^{-1} range, as experimental limitations prevent

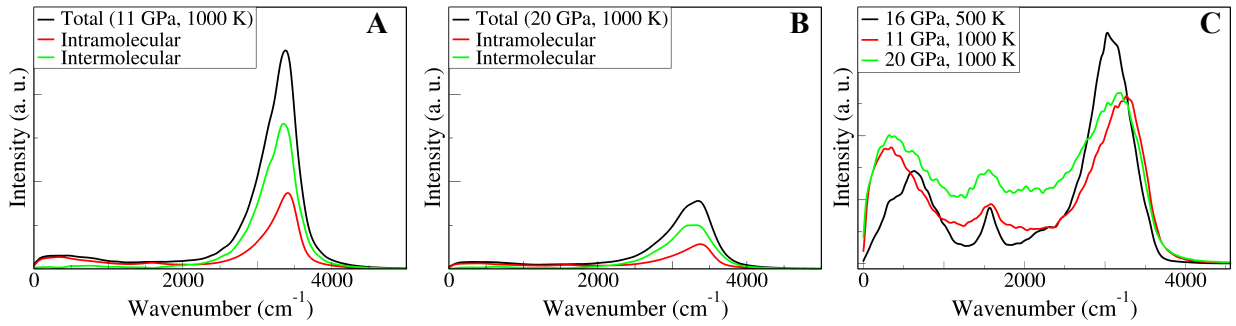

Figure 6.12: A) Computed unpolarized Raman spectrum at 11 GPa, 1000 K with inter- and intra-molecular components. B) Unpolarized Raman spectrum at 20 GPa, 1000 K with decomposition into intramolecular (red) and intermolecular (green) spectra. Both A) and B) are normalized for intensity comparison. C) Computed infrared spectra under different P,T conditions. Note the broad continuum intensity in the mid-IR region.

the measurement of frequencies between 800 cm^{-1} and 2200 cm^{-1}.

Previous computational studies have simply used the vibrational density of states (VDOS), as an approximation of the Raman spectrum [98]. Figure 4D shows that the VDOS reproduces the qualitative shape of the O-H vibrational stretching mode. However it differs from the Raman spectrum in the position of the maximum - the Raman peak is redshifted by about 50 cm^{-1} relative to the VDOS. In addition, the VDOS spectrum exhibits a peak near 1600 cm^{-1}, as well as prominent low frequency collective modes. Neither of these modes are Raman active and do not appear in the unpolarized spectrum.

Having validated our results with experiments, we proceeded to analyze them in detail. In agreement with the report of Ref. [114], we found no specific signature associated to hydronium ions, indicating that Raman spectra are not a good probe for these species in the liquid, where however they are present, as discussed above. We also observed the same asymmetry in the O-H stretching peak as reported experimentally [114]; by using a simple decomposition of the signal into two Gaussians, Holmes et al. attributed the lower- and higher-frequency shoulders of the stretching peak to hydrogen- and non-hydrogen bonded water molecules, respectively. In order to analyze the nature of this asymmetry, we decomposed the total spectrum into inter- and intra-molecular components; we followed the

procedure of Wan et al. [275] and used MLWFs to define effective molecular polarizabilies in the fluid. We found that the lower and higher frequency shoulders of the asymmetric peak correspond to inter- and intra-molecular contributions, respectively (Fig. 6.12A, B); this finding is consistent with experimental reports. However we found that the intensity of the low frequency shoulder relative to the total peak at 11 and 20 GPa is similar; this finding is contrary to the experimental claim that the lower frequency contribution (from hydrogen bonding) is substantially weakened between 11 and 20 GPa along the Hugoniot. The persistence of hydrogen bonding at high pressure was also observed in the analysis of the pair correlation functions (see Fig. 6.2).

The described asymmetry in the O-H stretching Raman peak has been used as a crucial fingerprint of melting. For example, large changes in such asymmetry combined with the absence of a low frequency translational mode have been used to identify melting of ice VII [151, 150]. The computed spectra at 11 and 20 GPa confirm these qualitative properties of the liquid phase. However the absence of low frequency modes should not be interpreted as a sufficient indication that the system is liquid. Fig. 6.11C presents a spectrum of the non-diffusive quenched phase at 16 GPa and 500 K, together with the experimental ice VII Raman spectra from Lin et. al [150]. Though both the simulated and experimental sample are non-diffusive, they display markedly different spectra. The quenched phase exhibits neither a low frequency lattice mode nor a heavy asymmetry of the O-H stretching peak. We present this case as a cautionary example that amorphous phases may display Raman features usually assigned to liquid.

6.3.5 Infrared Spectroscopy

We computed the infrared spectra intensity, $A(\omega)$, in terms of the time derivative of the sample dipole moment [265], as outlined in Section 3.3.2 and Eq. 3.14. We showed above that computed Raman spectra, similar to experimental ones, present no clear signatures of the short-lived dissociating species effectively present in our simulations. Instead we found

that such signatures are present in infrared spectra shown in Fig. 6.12C. The computed IR spectra display clear OH stretching modes centered near 3100 cm^{-1}, but unlike the Raman spectra, they also display a considerable intensity below the OH mode.

Such intensity is enhanced with pressure: we observed a roughly twofold increase in the background IR intensity in the mid IR region (400 cm^{-1} to 2500 cm^{-1}) with increasing pressure from 11 to 20 GPa along the isotherm. From an analysis of our MD trajectories, we could detect the presence of transient Zundel ions in the high pressure fluids, which are expected to be responsible, at least in part, for the broad IR band below the OH stretching peak, consistent with the hypothesis of Ref. [121]. We note that a broad, mid-IR continuum absorbance was also observed in a number of aqueous systems at ambient conditions, from protonated clusters [124] to bulk acidic solutions [264, 25, 54]. An ultrafast 2D IR study of the excess protons in aqueous hydrochloric solutions [264] ascribed the broad-band intensity to vibrational modes of the Zundel and Eigen ions. This view is consistent with that of a recent study using femtosecond spectroscopy to precisely probe the vibrational signatures of the Zundel ions in a $HClO_4$ solution [53].

6.4 Conclusions

In summary, we have investigated water under pressure at 11 and 20 GPa, along the 1000 K isotherm, using ab initio molecular dynamics. We have characterized the properties of the fluid by computing structural properties, ionic conductivities, Raman and IR vibrational spectra, and we have identified dissociation mechanisms from a detailed analysis of computed trajectories. Our results are consistent with the estimate of the ice VII melting line proposed by Lin et al. [151], with a melting temperature below 1000 K at 20 GPa. We found that along the 1000 K isotherm, liquid water is a rather complex fluid, exhibiting rapid molecular dissociation events occurring via a bi-molecular mechanism. The short-lived hydroxide, hydronium, and more complex ions present in the fluid are responsible for a conductivity which, at 11 and 20 GPa, is six and seven orders of magnitude larger than at ambient

conditions, respectively. We emphasize that the conductivity calculations reported in our work were conducted fully from first principles, without any a-priori assumption on charge carriers or ad-hoc definition of charges. In spite of frequent dissociation and re-association events occurring under pressure, hydrogen bonds persists in the fluid at least up to 20 GPa. Interestingly, while vibrational signatures of hydroxide and hydronium ions are not present in unpolarized Raman spectra, as observed experimentally, they can be identified in IR spectra at frequencies lower than those of the OH stretching band. The absence of Raman signatures of hydronium ions led to past suggestions of unimolecular dissociation in water at high P, at variance with what we observed in our simulations where free protons are transient species with lifetimes below 0.3 fs. We expect that our computed Raman and IR spectra, reported also for a quenched amorphous phase, will serve as guidance for future experiments. Finally, the interpretation of the depth dependence of the electrical conductivity in the mantle transition zone as measured by magnetotellurics is still controversial, and linked to the effect of water on mantle minerals [287]. Our findings on the high conductivity of water and the dissociation mechanism found in the liquid at (P, T) conditions relevant to the mantle transition zone may guide future models of water in mantle geochemistry.

CHAPTER 7

PROPERTIES OF SIMPLE ION SOLVATION AT THERMODYNAMIC EXTREMES

7.1 Introduction

While our study on pure water is essential to build a complete understanding at conditions of 10-20 GPa and 1000 K, pure water without impurities, ions, or various minerals, is rarely found in isolation in any geochemically relevant environment. Aqueous ion and salt solutions play a key role in many processes in the Earth's mantle, including geochemical processes such as metasomatism, magma in subduction zones, and the Earth's deep water and carbon cycles. These fluids have many impurities, with properties dependent on the ionic concentration. Despite the key role of ions in water in determining the properties of the Earths mantle, still much is unknown about the molecular level properties of such solutions, including the effect on ion solvation shells, the effect on conductivity, and the effect on dielectric constants.

At lower crustal pressure and temperatures, the presence of Na and Cl dissolved in water are thought to greatly increase the electrical conductivity of aqueous fluids while substantially decreasing the activity of water and increasing the solubility of several crustal rocks. However, first principles simulations have rarely been used to study water at these conditions. A recent study from our group studied the association of oppositely charged ions (ion-pairing) as a first step in the nucleation process of salts, which ultimately affects the conductivity of saline solution [291]. A thorough examination of ionic conductivity in aqueous ion solutions at these conditions is lacking. Another crucial quantity is the dielectric constant, which is intimately connected to mineral solubility properties [193]. The dielectric constant measures the ability of a solvent to shield oppositely charged ions in the solution from electrostatic attractions to each other. In light of this, the dielectric constant of water at elevated pressures and temperatures is a crucial input into various geochemical models such as the Deep Earth Water model[259]. Similar to the conductivity, the behavior of the

dielectric constant under the effect of ions in aqueous solutions has not been studied.

In our study, we shed light on the ionic conductivity and dielectric constant with the application of first principles molecular dynamics. As we were interested in understanding the properties of aqueous ion solutions in part of water's P/T space that is unambiguously liquid state, we chose to focus on the 1.57 g/cm^3 density at 1000 K, which corresponded to 11 GPa for pure water. We examined high pressure ion solvation in water for several ions, including Li, K, Cl, and NaCl. While these ions are geochemically relevant in their own right, they also provide a means to systematically examine the effect of ion size in water these conditions. Furthermore, given our extensive analysis of monovalent cations described in Chapter 3, there is a solid basis for comparison of effects between ambient and high pressure/temperature conditions.

In section 7.2, we discuss he computational methods in our simulations of aqueous solutions at high P/T. In section 7.3, we present the results and analysis of our simulations, including analysis of vibrational spectra, dielectric constants, and ionic conductivities. In Section 7.4 we present conclusions.

7.2 Computational Methods

Our computational approach for the high pressure aqueous ion solutions was very similar to that used for pure water, as described in Chapter 6 and Ref. [223]. We again performed ab initio MD simulations in the Born–Oppenheimer approximation with the PBE exchange-correlation functional [198] and the Qbox code [1]. The choice of the PBE functional was motivated by the previously discussed good agreement with experiment found for the fluid equation of state at high pressure as well as for direct comparison to our earlier work on pure water.

We used norm-conserving pseudopotentials [273] (http://fpmd.ucdavis.edu/potentials/), with a plane wave basis set and kinetic energy cutoff of 60 Ry. The bulk salt solutions for ions Li^+, K^+, and Cl^-, were modeled by periodic cubic cells consisting of a single ion and 63

water molecules, with the excess charge compensated by a uniform background charge. The salt concentration corresponds to 0.87 M. The densities of water were 1.57 g/cm^3, computed at 1000 K to correspond to pressures of 11 GPa. We found that in the K^+ solution, the pressure was lower (6 GPa) at this density. We also ran simulations of ion solutions of water in larger cells, consisting of 127 water molecules and one a single ion, consisting of a single ion: Li^+, K^+, with the excess charge again compensated by a uniform background charge. The salt concentration in this case corresponds to 0.44 M. We also performed simulations of 126 water molecules with two ions, Na^+ and Cl^-, both in the cell. All ion solutions in the smaller cells were initialized from the end point of the earlier pure water trajectory, where one water molecule was replaced with an ion. For the larger cells, we equilibrated 127 molecules with the single ions for 10 ns using the SPC/E potential.

We controlled the temperature with the stochastic velocity rescaling method [33]. Simulation timesteps were 10 au (0.121 fs), while the thermostat time was 121 fs. In the interest of computational time, the full computation of DFPT-based polarizabilities was performed every 25 MD steps. Trajectories were collected for ∼150 ps and ∼60 ps for the small and large simulation cells, respectively, after initial equilibration of ∼10 ps.

7.3 Results and Discussion

7.3.1 Modifications to ion solvation shells

We begin by inspecting the ion solvation shells under high pressure/temperature conditions. First we note that the solution with Li^+ contains a unique and new molecular species: H_xLiO_2 (x=2:4) 7.1A, B. The H_xLiO_2 complex is long-lived, with a lifetime on the order of 10s of picoseconds. The existence and longevity of the H_xLiO_2 complex is consistent in both the small and large simulation cells. It exhibits the Li^+ atom bound to two flanking oxygen atoms, each of which engages with the same dissociation and proton hopping as the rest of the fluid, with the total complex varying from two four hydrogens. As far as we are aware,

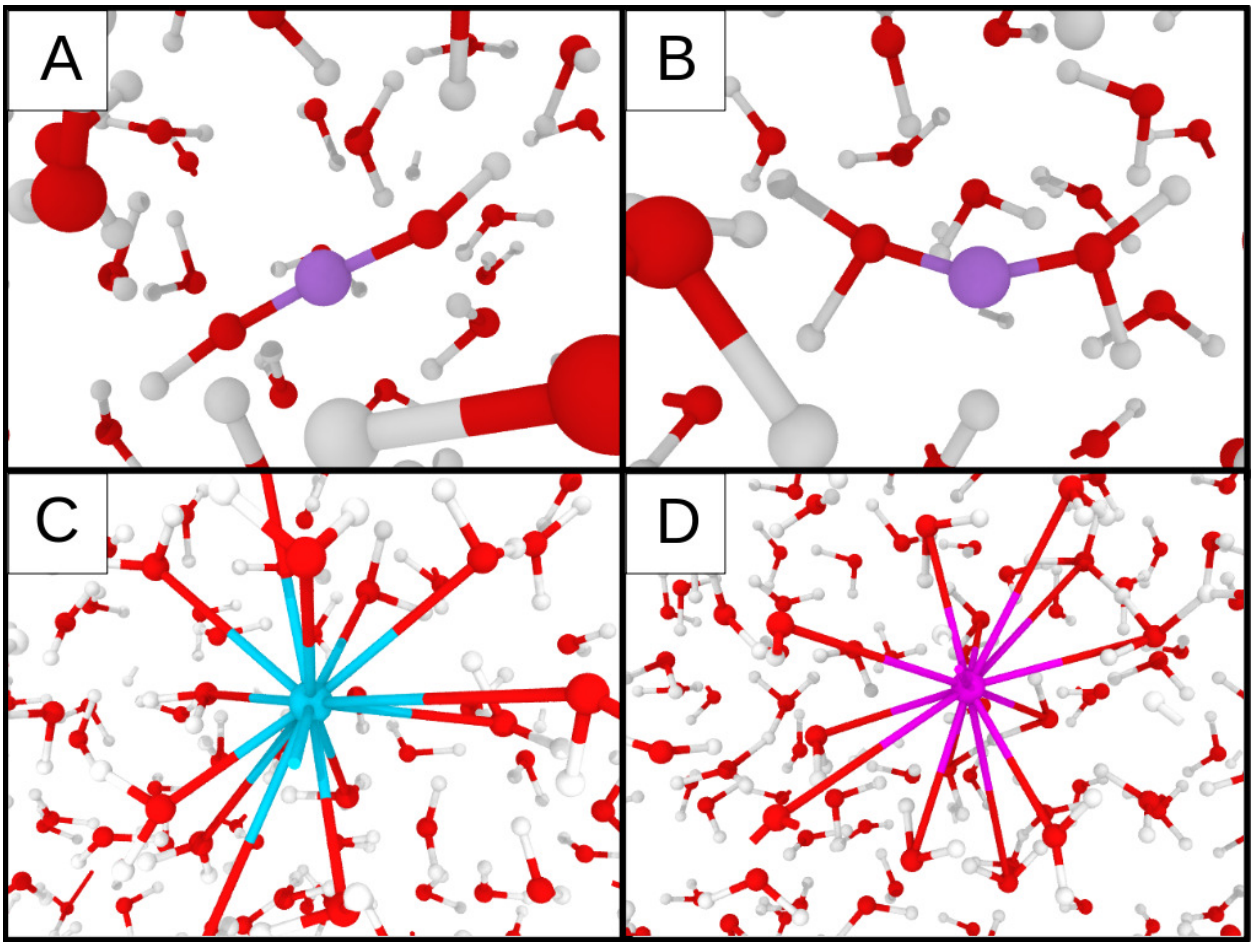

Figure 7.1: A) Lithium ion complex H_2LiO_2 B) Lithium ion complex H_4LiO_2 (x=2:4) C) K^+ ion solvation shell D) Cl^- Ion Solvation shell. In C and D, the color highlights all oxygen atoms within the first ion solvation shell, rather than a chemical bond.

this is the first prediction of such a new and long-lived ionic complex in aqueous solution at these conditions. On the other hand, the larger ions including K^+ and Cl^- exhibit no such bonding with oxygen (7.1C, D). In contrast, they maintain very large and rapidly exchanging solvation shells, similar to the behavior at ambient conditions.

Next we examine the solvation properties of the ions in the high pressure solutions using the radial distribution functions between the solvated ions and oxygen atoms of water molecules (Fig. 7.2A). At ambient conditions, we had found that the position of the RDF first maximum follows the ion size: $Li^+ < Na^+ < K^+ < Cl^-$, yielding a value of 1.97, 2.44, 2.81 and 3.10 Å for Li^+, Na^+, K^+, and Cl^-, respectively. Here we find that the trend in ion

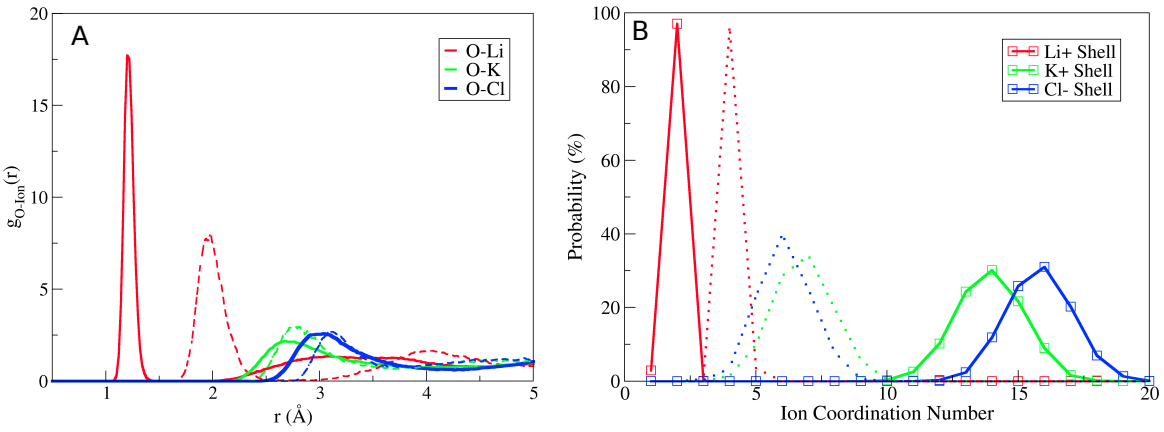

Figure 7.2: A) The O-ion radial distribution function of all high pressure ion solutions. Dotted lines indicate the reference at ambient conditions. B) The ion coordination number distributions. Dotted lines indicate the reference at ambient conditions.

solvation shells is very similar. The positions of the RDF first maximum follow the ion size, yielding values of 1.25, 2.71, and 3.0 Å for $Li^+ < K^+ <$ and Cl^- respectively. Thus, the effect of the extreme conditions is greater on the lithium solvation shell, which is reduced by 0.7 Å, than the larger ions, which are only reduced by about 0.1 Å.

We also examine the average oxygen coordination number of the ions, which is reported in Fig. 7.2B. We find that the coordination number in the first ion solvation shell changes significantly for all ions. In the Li^+ solution, we observe a decrease from 4 at ambient conditions to 2 at high pressure/temperature. This change in coordination is consistent with the observation of the new H_xLiO_2 (x=2:4) complex, where the first coordination shell is simply the new oxygen atoms that are bonded to to the Li^+ atom. We find coordination numbers of 14.2, 16.1 for K^+, Cl^-, respectively. These are increases of 8 and 10, respectively from the behavior at ambient conditions. Thus, for the larger ions, the change in the position of the first ion solvation is minimally affected despite a very large increase in coordination. We also found that oxygen-oxygen and oxygen-hydrogen RDFs (Fig. 7.3) of all solutions do not show any notable change relative to the corresponding ones of pure water, pointing to

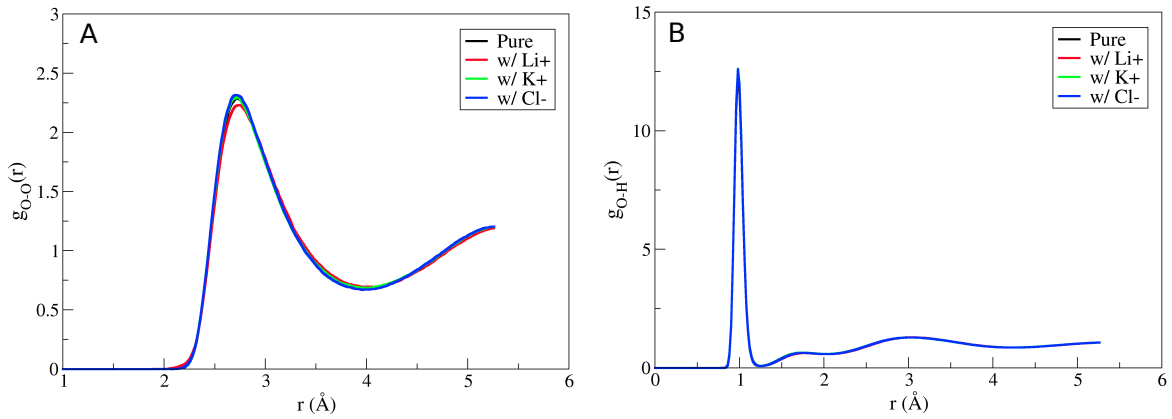

Figure 7.3: A) The O-O radial distribution function of all high pressure ion solutions. B) The O-H radial distribution function of all high pressure ion solutions.

minimal effects of the ions on the global structure of water at the concentration considered here. This result is consistent with the behavior of ion solutions at ambient conditions, where ion solutions also did not affect the global structure of water (Fig. 4.2. Finally, we also computed the pair distribution function between oxygen and the MLWF centers in the high pressure solutions, showing our result in Fig. 7.4, and again indicating no noticeable differences among ions and pure water at these conditions. Given that the first peak minimum of the O-H RDF as well as the O-M MLWF are key signatures of molecular dissociation, we notably find that that the extent of dissociation is consistent among all ion solutions.

7.3.2 Vibrational Spectra

While we found some differences in local solvation shell properties, our structural analysis found no meaningful differences on the global structure of water at these conditions among ion solutions. We move from structural analysis to examine dynamical and spectroscopic properties of the liquids.

We computed the mean squared displacements of all ion solutions, and present the reuslts in Fig. 7.5. In this case, we plot all oxygen and hydrogen atom displacements across all

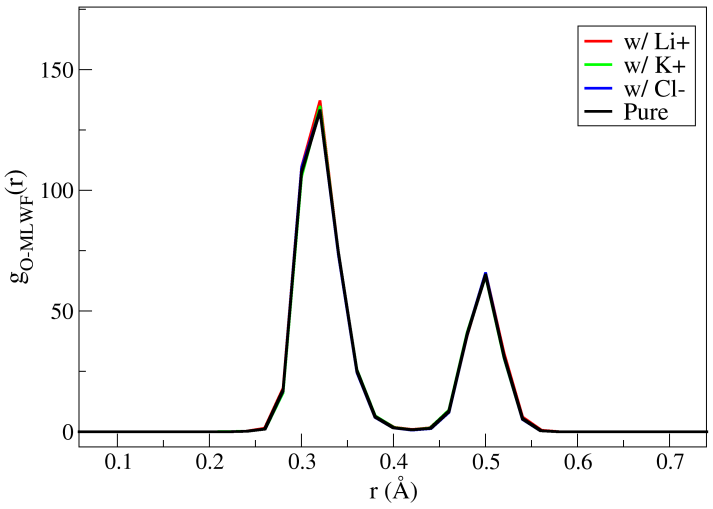

Figure 7.4: A) The O-MLWF radial distribution function of all high pressure ion solutions.

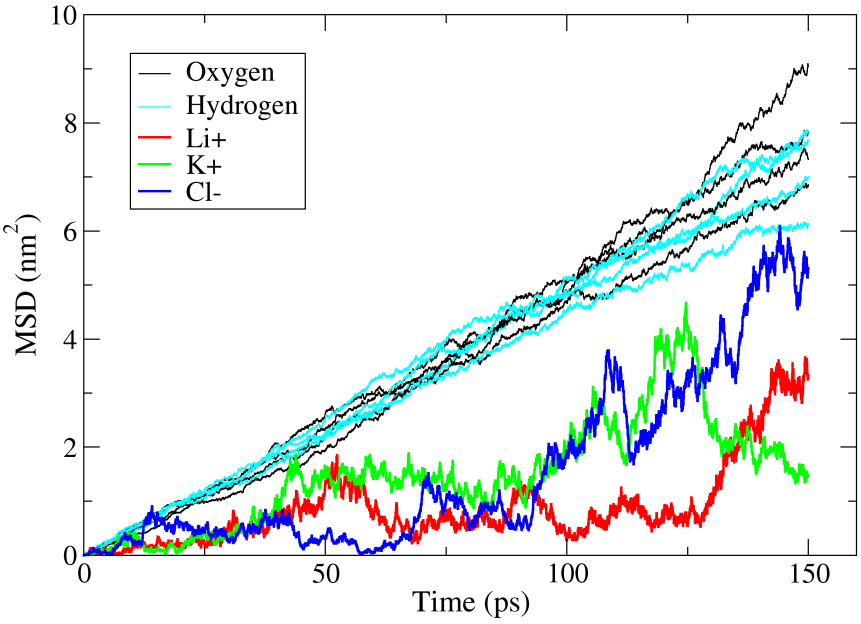

Figure 7.5: The mean squared displacement of all oxygen, hydrogen, and ions in the high pressure ion solutions, at 11 GPa, 1000 K. Oxygen and Hydrogen lines are not distinguished among ion solutions, and also contain data from pure water at these conditions.

ion solutions as well as pure water at these conditions without distinctions. While we do not have the statistical robustness that we employed in Chapter. 3 for diffusive analysis of bulk ambient water diffusion, it is clear that the range of MSD curves among the various ion solutions falls well within the level of variance that was found for multiple independent trajectories in the bulk simulations. Thus, our simulations show no evidence that any of the ion solutions exhibit global bulk water diffusion that is altered from the pure case. This is again, an instance of minimal effect of ions on water at these conditions, and a consistency with properties in the bulk. Additionally, we found all ion diffusions to diffuse slower than their surrounding water, despite very different solvation shells; the K^+ and Cl^- cases diffuse with large, floppy, and rapid exchange in the first solvaiton shell, while the Li^+ solvation shell essentially diffuses as a well-defined molecule.

In search of discriminating features among the ion solutions, we next turn to analysis of the vibrational spectra of the fluids. We computed the infrared spectra, and here we followed the same procedure as outline in Chapter 6 for the pure water simulations. Infrared spectra were computed as the Fourier transforms of the sample dipole moment, as computed using MLWFs. Our results are shown in Fig. 7.6A, where we compare all ion solutions to the infrared spectra of pure water at these same conditions, as reported in Ref. [223]. We note that there are no essential differences in either location of peak centers of the O-H stretching and bending modes or the relative intensity of peaks between all ion solutions and pure water. The same continuum frequency that was identified as a signature of the dissociative fluid in the study of pure water is present here in all aqueous solutions. The first-peak minimum of the OH rdf marks molecular dissociation, and is unchanged between ion solutions, as shown in Fig 7.1B. The similarity of the indistinguishable dissociation signatures and the indistinguishable infrared continuum further strengthens the connections between the two and our identification of the continuum as a signature of dissociative water [223]. While there may be small differences in the low-frequency collective modes, overall we emphasize that the introduction of a range of ions does not exhibit any new vibrational signatures in the

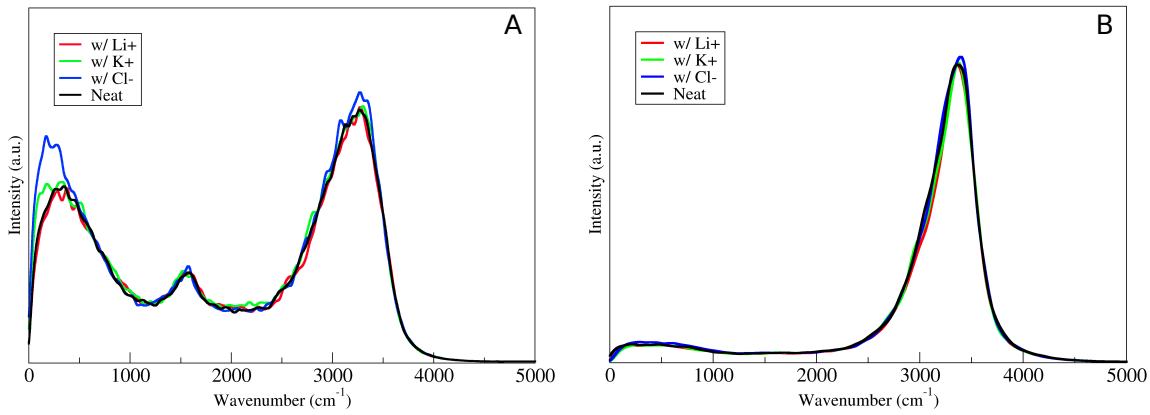

Figure 7.6: A) The infrared spectra and B) unpolarized Raman spectra of high pressure ion solutions.

infrared spectrum. We also computed the unpolarized Raman spectra, again following the earlier procedure, where spectra were computed from the correlation function of the system's polarizabilities [15]. Our results are shown in Fig. 7.6B, where again there are neither any new vibrational signatures nor differences among the ion solutions.

Our results from infrared and Raman spectra are particularly interesting when compared to the simple vibrational density of states (VDOS) that is computed for the ion solutions simply from the velocites of the atomic species. In Fig. 7.7A, we again note no differences among ionic solutions in the VDOS. However, in 7.7B we decompose the spectrum of the Li^+ solution into its constituent atomic contributions. We find that the vibrational modes of the Li^+ ion itself actually mirror the qualitative shape of the overall water spectra, but at damped frequencies. The behavior of the Li^+ spectrum may be attributed to its bonding with the two flanking oxygens in the new H_xLiO_2 (x=2:4) species. Thus, our results indicate that despite the presence of new vibrational modes in the fluid (e.g., at 2000 cm^{-1}), neither infrared nor Raman spectroscopy detect the change, which is entirely masked by the other water molecules in the cell.

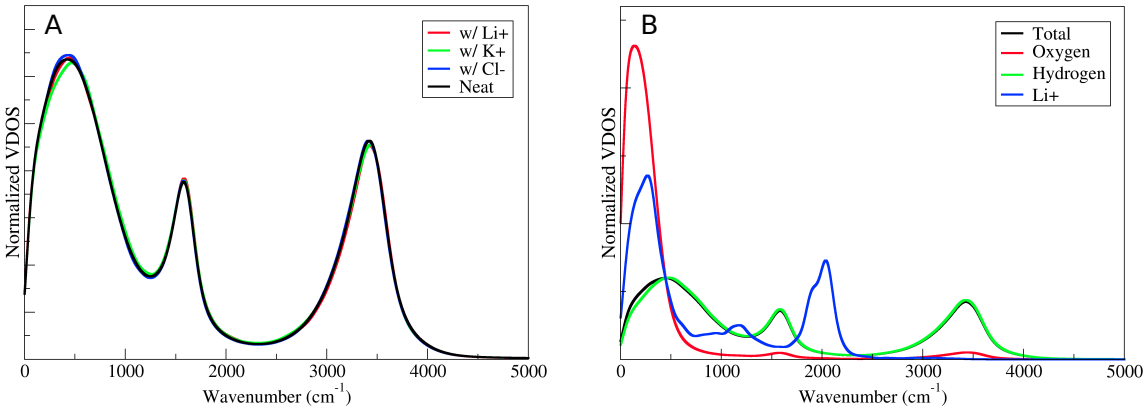

Figure 7.7: A) The total vibrational density of states (VDOS) spectra and B) VDOS breakdown by atom type for the Li^+ solution

7.3.3 Molecular Polarizability

Given the success of the molecular polarizabilities in identifiying perturbations to water structure due to ions and confinement, as described in Chap. 4 and 5, we again use the method of Ref. [195] to now examine molecular polarizability of aqueous solutions at high P/T. We present our results in Fig. 7.8, where we show a reference of bulk ion results on the left (white) and the high pressure results on the right (blue). A first observation is that all of the molecular polarizabilities under high pressure and temperature are reduced by ~10% relative to the bulk values. This result is consistent with the result of Pan et al. for pure water [195], and extends the trend to ion solutions as well. We also note that there is qualitative agreement between the ambient and high P/T conditions on the relative relation of solvation shells relative to the rest non-solvation shell contributions. Our results on molecular polarizability indicate that while there is an overall reduction relative to ambient conditions, many of the ion trends are remarkably resilient under high pressure/temperature.

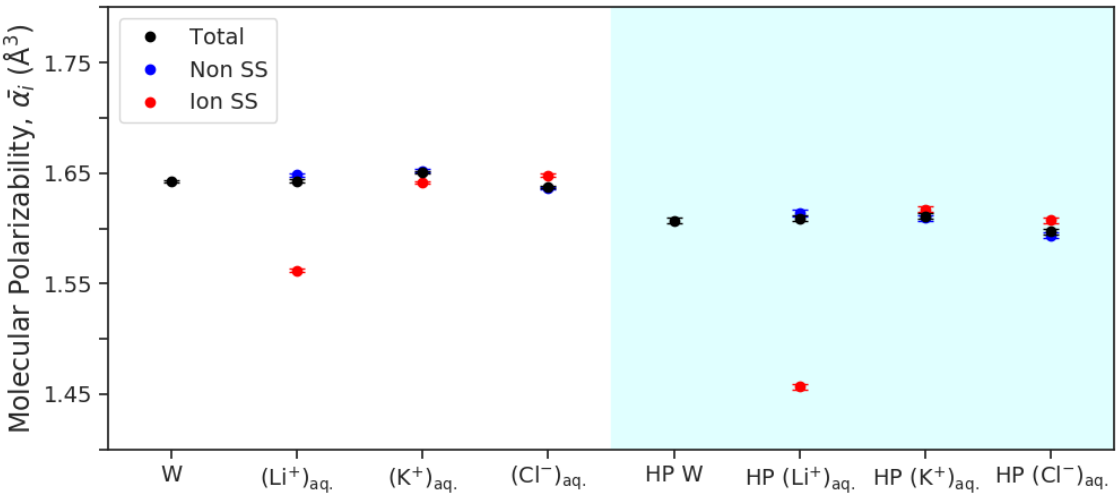

Figure 7.8: The molecular polarizability of ambient ion solutions (white background) compared to high pressure ion solutions (blue background)

7.3.4 Enhancements of Ionic Conductivity

The electrical conductivity of aqueous ion solutions is of particular relevance to the high pressure regime. In Chapter 6, we computed the ionic conductivity of pure water at 11 GPa and 20 GPa along the 1000 isotherm, confirming and explaining from first principles the elevated conductivity of dissociative water [223]. Here we turn to compute the conductivity in the solutions with water. Our results are given in Fig. 7.9, where we plot the squared displacement of the sample total dipole moment, whose slope is proportional to the ionic conductivity. Here we take advantage of analyzing simulations at two cell conditions - one with 63 water molecules, and one with 127 water molecules. The values of σ for the smaller simulation cells were 2.5 (0.2), 8.8 (0.5), and 9.0 (0.5) for the L+, K^+, and Cl^- solutions respectively. In the larger simulation cells, the values of σ were 3.8 (0.6), 4.2 (0.6), and 3.8 (0.6) for the Li^+, K^+, and NaCl solutions, respectively. Here, the uncertainties in the values of σ were computed using the cepstral analysis method, which was recently introduced to compute thermal conductivities from optimally short trajectories [70]. Our findings on σ indicate potentially large variations with simulation cell, in addition to the basic difficulty

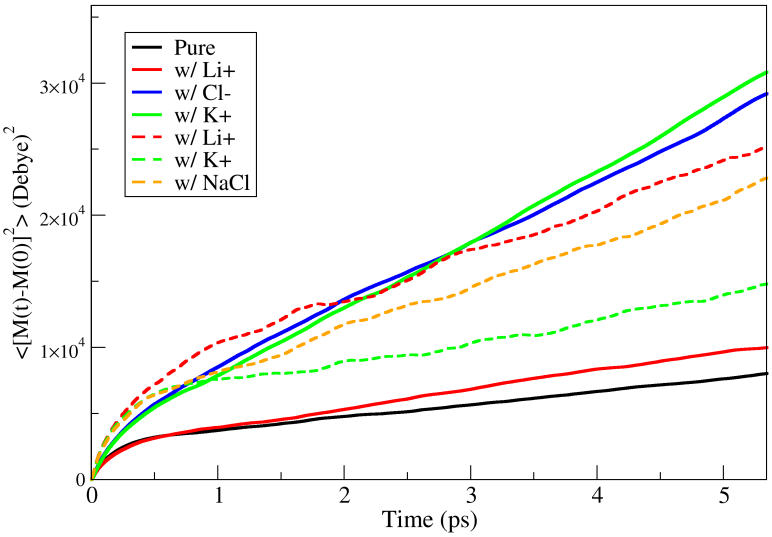

Figure 7.9: Comparison of the averages of time-averaged mean squared displacement of the total dipole moment **M** as a function of separation time for multiple partitioned segments of length 10 ps at 11 GPa and 1000 ion solutions. Solid lines indicate solutions in the smaller water boxes (63 water molecules), while dashed lines indicate solutions in larger water boxes (127 water molecules).

of good convergence of such a highly collective quantity [52]. A firm result of our analysis is that the conductivity of pure water is a lower limit of the ionic conductivity of the ion solutions. All solutions with ions increase the conductivity of the fluid, though the exact ordering of ions is difficult to determine because of the finite size effect. No enhancement is greater than a factor of 9, and the lower conductivities in the larger cells suggest that the enhancement of the solutions may be closer to a factor of 4 relative to pure water. This result is fundamentally interesting because the enhanced conductivity in pure solutions between 11 and 20 GPa was linked to the increase in dissociative water [223]. In the case of ions, we have demonstrated from structural analysis that there is not an induced additional dissociation due to the ions. Thus, the enhancement of conductivity has a different source than increased dissociation, which we speculate may be related to the increased exchange of water molecules in the solvation shells of the ions relative to the rest of the fluid.

7.3.5 Reductions of Dielectric Constant

The dielectric constant is a measure of the ability of a solvent to shield oppositely charged ions in the solution from electrostatic attractions to each other, and is crucially linked to geochemical models that determine solubility of minerals [259]. However, the effect of ions on the dielectric constant of water in these dissociative conditions is unknown. We next present our results on the dielectric constant of aqueous ion solutions at extreme conditions.

Our results are given in Fig. 7.10A and B, which give values of ϵ_0 for the small and large simulation cells, respectively. In Fig. 7.10A, the trajectory for pure water comes from our earlier work (Ref. [223]), for which we did not report ϵ_0 at the time. First, we note that our computed value of ϵ_0 for pure water is 39, which is full agreement with the earlier pioneering study of Pan et al, (Ref. [193]). The result there was computed using 128 water molecules at the same density and temperature. The correspondence with our value using only 64 molecules indicates that finite size effects on the dielectric constant of water at these conditions may be relatively modest, though the convergence time of the quantity is considerably longer for the smaller simulation cells (150 ps vs 30 ps). The aqueous ion solutions in the smaller simulation cells are also presented in Fig. 7.10A, where we see that no ion solutions exhibit values of ϵ_0 greater than that of pure water. Interestingly, it is the smaller Li^+ cation that has a larger effect on ϵ_0 than K^+, which appears to have no effect on the surrounding water. The ordering of ϵ_0 in the ion solutions, based on the last 25 ps of the converged quantity, is $K^+ > Li^+ > Cl^-$. Here, ϵ_0 of aqueous K^+ solution is nearly identical to the pure water. Li^+ and Cl^- solutions yield 5% and 10% reductions, respectively. In order to test the robustness of this result, we also examined the dielectric constant of Li^+ and K^+ in larger simulation cells, with 127 solvating water molecules. The results, given in Fig. 7.10B are compared to the earlier computed value from Ref. [193], which was computed at the same simulation cell size. Our results for the larger cells are consistent with the trends from smaller cells, as we find that K^+ solution is unaltered relative to bulk water, while Li^+ solution is reduced, in this case by 10%. The NaCl solution, for

which we do not have a counterpart at the smaller simulation size, appears to take longer to converge relative to the single monovalent ions. The reductions to ϵ_0 in the NaCl solution are 10%. The primary conclusion of our calculation on dielectric constants is that ϵ_0 of pure water is as an upper bound on ϵ_0 in solvated ion solutions. The exact extent of the reduction is difficult to quantify with certainty, but appears to be no more than 10%.

To the best of our understanding, ϵ_0 of water in aqueous ion solutions has not been computed at these conditions. Our result is particular relevant to the Helgeson-Kirkham-Flowers model for aqueous speciation, which requires Gibbs free energy of formation of an aqueous species, based on the Born function for the average Gibbs energy of solvation,

$$\Delta \bar{G}_{s,j} = \omega_j (\frac{1}{\epsilon_0} - 1) \tag{7.1}$$

where ω_j is the electrostatic Born parameter for the ion j, and ϵ_0 is the static dielectric constant of the solvating water. Our finding that ϵ_0 of pure water is an upper bound of aqueous monovalent ion solutions at high pressure and temperature, in turn implies a lower bound on $\Delta \bar{G}_{s,j}$, that may be helpful in parameterizing geochemical models such as the Deep Earth Water (DEW) model by giving bounds on the extended term of the Debye-Hückel equation [259].

7.3.6 Free energies and clustering

Given that no structural or spectroscopic signatures were found to be distinct from pure water at these cases, despite meaningful changes to ionic conductivity and dielectric constant, we chose to further interrogate the structure of water at these conditions. We chose to employ the Probabilistic Analysis of Molecular Motifs (PAMM) algorithm, which is a machine learning unsupervised clustering method for postprocessing atomic trajecotories and finding

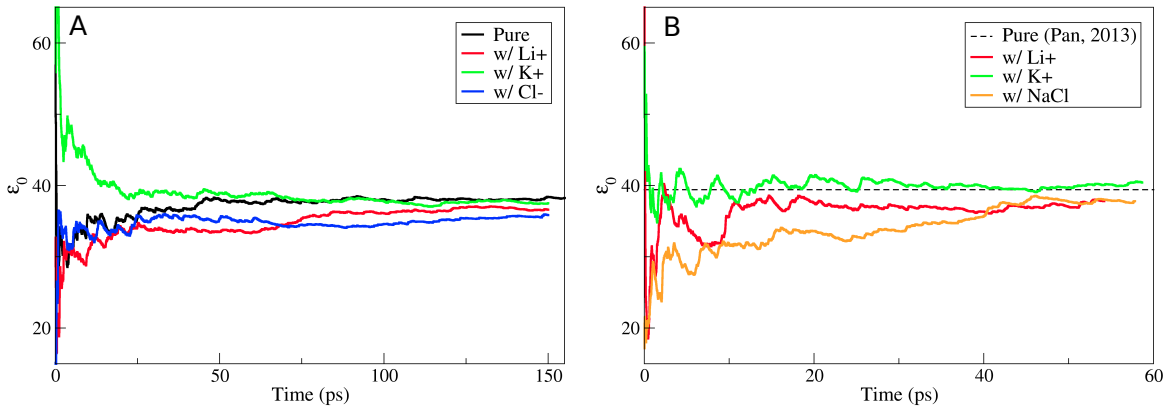

Figure 7.10: A) The static dielectric constant in 63 H2O moleculescells and B) 127 H2O molecule cells.

similarities in structural motifs [91]. The first steps in the application of PAMM are the identification of groups of atoms that should be tested for recurring patterns and the choice of structural parameters that describe the arrangement of atoms within each group. Given our study of water, an approach which focused on the presence of hydrogen bonding (HB) may well interrogate the local structure of water and any changes due to ions. We selected a parameter space defined by triplets of atoms, where on atomic species is considered as the HB donor D, one is considered as the acceptor A and hydrogen atoms that complete the HB triplet. The geometry of each of these groups is completely determined by the three distances: d(A−D), d(A−H),and d(D−H). As has been previously done in the case of studying water [91], we use combinations of these distances, namely, the proton-transfer coordinate ν=d(D−H)−d(A−H), the symmetric stretch coordinate μ=d(D−H)+d(A−H), and the acceptor-donor distance r=d(A−D) as the group descriptors. We computed these (ν, μ, r) triplets for each D-H-A group present in each snapshot extracted from the simulations, thereby obtaining the training data set that we used to run PAMM.

Before examining any clustered motifs that emerge from the training of the data, we first take advantage of the new coordinate system in order to compute free energies surfaces along

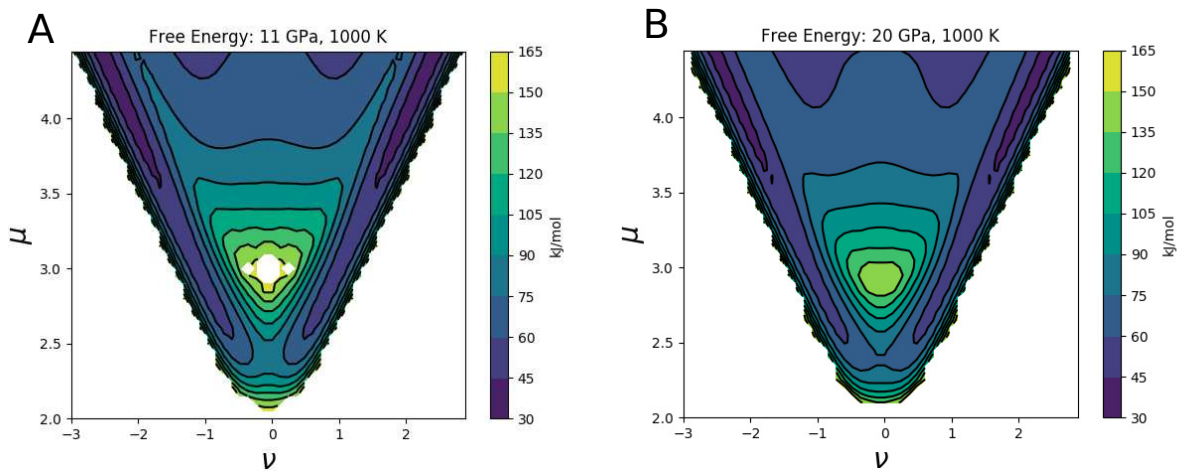

Figure 7.11: Comparison of the free energy surfaces of O-H-O triplets in water at A) 11 GPa, 1000 K and B) 20 GPa, 1000 K

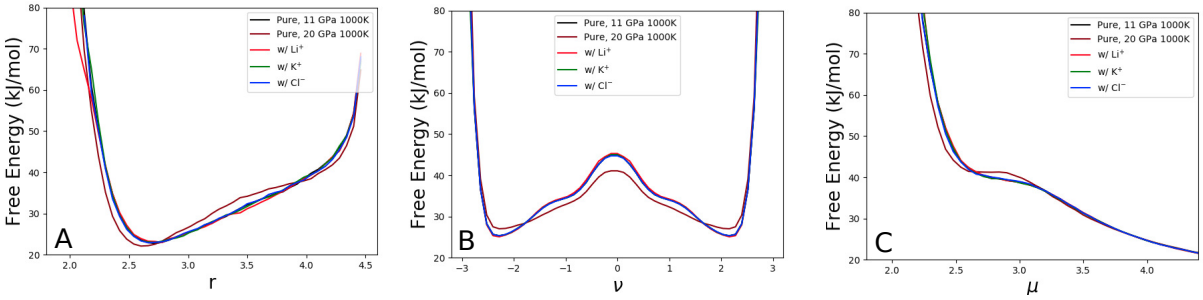

Figure 7.12: Comparison of the free energies across each variable axis for O-H-O triplets in solutions at high P/T water conditions, as defined in text.

the described variables, based on histograms of the frequency of visitation in phase space. The results for the pure water at 11 GPa and 20 GPa from Ch. 6 are given in Fig. 7.11, where a clear difference is seen in the free energy barrier of dissociation, which is lowered at higher pressure. This information is presented in 1-dimensional decompositions for all high pressure solutions in Fig. 7.12. We note that in all cases, there are noticeable differences in the free energy of the 20 GPa case relative to the 11 GPa cases. However in none of the various ion solutions across all dimensions is there a difference in free energy relative to the pure water. This is further evidence of the resilience of water to alterations from ion perturbation at high P/T, especially in the regime associated with hydrogen bonding.

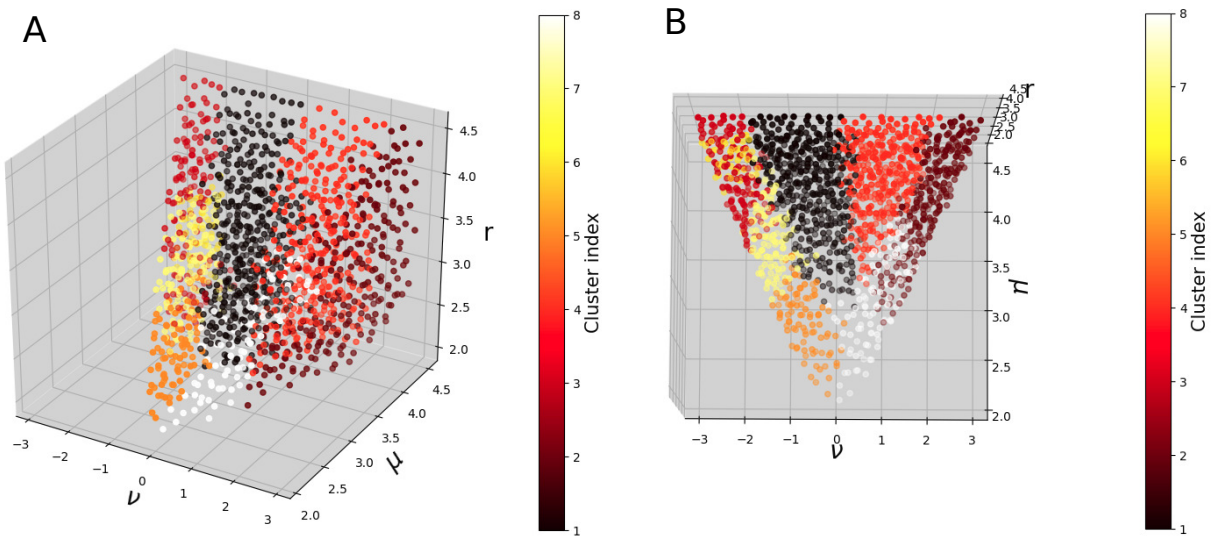

Figure 7.13: Molecular motif clusters found in the 11 GPa, 1000 K pure water, using the PAMM method. A) side view of the cluster phase space B) top view onto the μ and ν axes.

The clustering that emerges from the PAMM training is visualized in Fig. 7.13. While many clusters emerge in the high P/T regime, the clusters associated with hydrogen bonding in this coordinate space are those represented by orange and white coloring in the figure (clusters 5 and 8), which correspond to hydrogen bond accepting and hydrogen bond donating configurations. The symmetry of the motif clustering found here over the proton transfer coordinate, ν is maintained across all ion solutions where the clustering was applied. This is strong evidence that the local nature of the hydrogen bonding is still persisting in the similarly symmetric pattern also exhibited at ambient conditions. Most importantly, in our PAMM analysis across ion solutions, we did not find qualitatively different clusters in the O-H-O coordinate system in the hydrogen bonding regime. This again is evidence of the resilience of water to ion effects.

7.4 Conclusions

We presented detailed analysis of how the structure of solvation shells is altered by high P/T. Global water structure in O-O and O-H RDFs are unaffected by ions. O-MLWF structure

is also unaffected by ions. On the other hand, ion solvation shells are very different between different solutions. Li^+ forms a long-lived complex, H_xLiO_2 (x=2:4), while K^+ and Cl^- form no new bonds with waters. The Li^+ solvation shell collapses to 2 coordination because of the new arrangement, while the larger ions are greatly increased by 7 to 8. MSD shows slow diffusion among all ions, with indistinguishable effect on global oxygen and hydrogen. Furthermore, dissociation free energy analysis also supported the view of little ion effects. Thus despite large changes in solvation shell environment, the effect on water properties (structure and diffusion) is remarkably similar to ions at ambient conditions. Similarly, vibrational spectra (Raman/IR) show no new active modes as signatures of ions or high P/T ionic species despite new vibrational signatures in the VDOS spectrum of Li^+ solution. At high P/T, even when identifying new species (H_xLiO_2 (x=2:4)), the vibrational spectra of water is very resilient to ion effects.

The extent to which we found ion effects in aqueous solutions at these conditions was all in intrinsically quantum mechanical properties. The molecular polarizabilities of ion solutions are reduced across the board, with Li^+ SS exhibiting much greater relative reduction than in bulk. Molecular polarizability continues to be sensitive to perturbations. Besides the reductions to α_i caused by pressure, it is notable that the effect of ions on total polarizability is virtually identical to the behavior at ambient conditions. Again, this speaks to the resilience of water to ion effects even at extreme conditions. We found that the dielectric constant of pure water is an upper limit for solvated ion solutions at these conditions. Furthermore, the ionic conductivity, now well-constrained with cepstral analysis method, is enhanced in high P/T solutions by a factor of 4 at most.

Advanced machine-learned clustering algorithms did not return an obvious source of the enhancement in conductivity from average structural considerations. H-bond clustering analysis indicates that there are no unique alterations to clustering in the H-bonding regime of any of the ion solutions.

CHAPTER 8

CONCLUSIONS AND OUTLOOK

In this dissertation, we examined aqueous solutions of solvated ions in bulk water and "extreme conditions" corresponding to nanoconfinement and elevated pressure/temperature. We applied first principles molecular dynamics simulations based on density functional theory to analyze both structural alterations to water at these conditions as well as quantum mechanical quantities, including Raman and infrared spectra, ionic conductivity, and molecular polarizabilities.

We found in our study of alkali cations in water (Li^+, Na^+ and K^+) that the water structure is only modified locally by the presence of cations. A significant conclusion was a generalization that molecular polarizabilities are fingerprints of hydrogen bonding modifications, which occur at most up to the second solvation shell for all cations in bulk water. We also applied our simulations of solvated K^+ to isotopic fractionation of potassium. In our study of confined aqueous solutions, we studied pure water and LiCl and KCl solutions under confinement within carbon nanotubes (CNT) of small diameter (1.1-1.5 nm). We concluded that the molecular polarizability is a much more sensitive probe of water perturbations than, e.g., the molecular dipole moment. The molecular polarizability of water molecules near the surface is determined by the balance of two effects: the presence of broken hydrogen bonds at the surface leads to a decrease of the polarizabilities of water molecules, while the interaction with the CNT enhances polarizabilities. The confinement effects on water molecular polarizabilities and dipole moments are more pronounced in the case of the 1.1 nm CNT, and were further amplified by the presence of ions.

Our examination of water at extreme thermodynamic conditions began with a study of pure water between 11 and 20 GPa. Our results support lower estimates of the ice VII melting line in this region. We found that liquid water in this regime is rapidly dissociating and recombining and forming exotic short-lived ionic species, which are sufficient to support the experimentally measured increase in conductivity, contrary to some arguments in the

literature. Ionic conductivity calculations were performed entirely from first principles, with no a-priori assumptions on the nature of charge carriers. Finally, we also computed the first ab initio Raman spectra, which are in excellent agreement with experiment, however show no distinctive signatures of dissociation. Rather, we found that the infrared spectra are more useful to this end, with a broad continuum intensity associated with increased dissociation in water. Our extension of this study to water with ions was the first to characterize basic ion solvation properties at these conditions, notably finding new long-lived ionic species in Li^+ solution. Nevertheless, we found essentially no alterations to any structural or free energetic characteristics of water due to the ion presence. In this way, water even in such a highly dissociative state displayed remarkable resilience in its similarity in ion effects to ambient conditions. We did, however, find moderate reductions to the dielectric constant as well as enhancements to the ionic conductivity, which might be attributed to dynamical properties of the fluid.

A central question in the study of condensed matter is to determine which quantities are sensitive probes of chemical environments and therefore worth measuring or computing in various systems. Across our various studies, the molecular polarizability has emerged as a very effective means to track alterations to water structure, from ion solvation to confinement, to high pressure/temperature. Experimentally, the molecular polarizability is only known with certainty in the gas phase [92]. In the condensed phase, the molecular polarizability is typically estimated from the refraction index, along employing the Lorentz-Lorenz relation. Our results should inspire further studies on water in various environments to focus on this quantity both experimentally and computationally.

Our results also point towards a remarkable resilience of water across various extreme conditions. Even with such large changes as total disruption of hydrogen bonding combined with interfacial effects in a carbon nanotube, the alterations to the dipole moments and polarizabilities were modest. Similarly, the changes of polarizability due to extreme conditions were also modest, with the addition of no spectroscopically distinct changes despite

the dissociative state or addition of ions. The point was further strengthened in that even at extremely high pressure and temperature, most of the properties of ion solvation were either directly analogous to bulk solvation or only moderately modified. Our results demonstrate a broad resilience of water's hydrogen bonding network over a range of extreme conditions.

Some very interesting and clear extensions of our work would be firstly to study other ions at these conditions. We chose to focus on monovalent ions in part due to their simplicity as a means to understand ion size trends. Divalent ions might exhibit a very different balance of properties both under confinement and thermodynamic extremes. Another clear extension of our work would be more comprehensive studies under various confining environments, geometries, and materials in order to test the generality of our results for systems under confinement. Finally, the study of several carbon and silicate compounds mixed with water at conditions relevant to the Earth mantle would be very important for geochemical modeling.

REFERENCES

[1] Qbox code: http://www.qboxcode.org.

[2] Kumar Varoon Agrawal, Steven Shimizu, Lee W Drahushuk, Daniel Kilcoyne, and Michael S Strano. Observation of extreme phase transition temperatures of water confined inside isolated carbon nanotubes. *Nature nanotechnology*, 12(3):267, 2017.

[3] Andrés Aguado and Paul A Madden. Ewald summation of electrostatic multipole interactions up to the quadrupolar level. *J. Chem. Phys.*, 119(14):7471–7483, 2003.

[4] M. Ahart, A. Karandikar, S. Gramsch, R. Boehler, and R. Hemley. High p-t brillouin scattering study of H2O melting to 26 GPa. *High Pressure Research*, 34:327, 2014.

[5] CM O'D Alexander, JN Grossman, Jingyuan Wang, B Zanda, M Bourot-Denise, and RH Hewins. The lack of potassium-isotopic fractionation in bishunpur chondrules. *Meteoritics & Planetary Science*, 35(4):859–868, 2000.

[6] D. Alfe and M. Gillan. First-principles calculation of transport coefficients. *Phys. Rev. Lett.*, 81:5161–5164, 1998.

[7] Edward Anders and Nicolas Grevesse. Abundances of the elements: Meteoritic and solar. *Geochimica et Cosmochimica acta*, 53(1):197–214, 1989.

[8] J. Aragones and C. Vega. The phase diagram of water at high pressures as obtained by computer simulations of the tip4p/2005 model: the appearance of a plastic crystal phase. *J. Chem. Phys.*, 130:244504, 2009.

[9] Volodymyr Babin, Claude Leforestier, and Francesco Paesani. Development of a "first principles" water potential with flexible monomers: Dimer potential energy surface, vrt spectrum, and second virial coefficient. *J. Chem. Theor. Comput.*, 9(12):5395–5403, 2013.

[10] Volodymyr Babin, Gregory R Medders, and Francesco Paesani. Development of a "first principles" water potential with flexible monomers. ii: Trimer potential energy surface, third virial coefficient, and small clusters. *J. Chem. Theor. Comput.*, 10(4):1599–1607, 2014.

[11] J. Bader and B. Berne. Quantum and classical relaxation rates from classical simulations. *J. Chem. Phys.*, 100:8359, 1994.

[12] Philip Ball. Water—an enduring mystery. *Nature*, 452(7185):291–292, 2008.

[13] Arindam Bankura, Vincenzo Carnevale, and Michael L Klein. Hydration structure of salt solutions from ab initio molecular dynamics. *J. Chem. Phys.*, 138(1):014501, 2013.

[14] A Barati Farimani and Narayana R Aluru. Spatial diffusion of water in carbon nanotubes: from fickian to ballistic motion. *J. Phys. Chem. B*, 115(42):12145–12149, 2011.

[15] Stefano Baroni, Stefano De Gironcoli, Andrea Dal Corso, and Paolo Giannozzi. Phonons and related crystal properties from density-functional perturbation theory. *Reviews of Modern Physics*, 73(2):515, 2001.

[16] Axel D Becke. Density-functional exchange-energy approximation with correct asymptotic behavior. *Physical review A*, 38(6):3098, 1988.

[17] Axel D Becke. A new mixing of hartree–fock and local density-functional theories. *J. Chem. Phys.*, 98(2):1372–1377, 1993.

[18] Axel D Becke and Marc R Roussel. Exchange holes in inhomogeneous systems: A coordinate-space model. *Physical Review A*, 39(8):3761, 1989.

[19] Arieh Y Ben-Naim. *Statistical thermodynamics for chemists and biochemists*. Springer Science & Business Media, 2013.

[20] HJC Berendsen, JR Grigera, and TP Straatsma. The missing term in effective pair potentials. *Journal of Physical Chemistry*, 91(24):6269–6271, 1987.

[21] HJC Berendsen, JPM Postma, WF Van Gunsteren, and AJ Hermans. Intermolecular forces, 1981.

[22] John D Bernal and Ralph H Fowler. A theory of water and ionic solution, with particular reference to hydrogen and hydroxyl ions. *J. Chem. Phys.*, 1(8):515–548, 1933.

[23] Jacob Bigeleisen and Maria Goeppert Mayer. Calculation of equilibrium constants for isotopic exchange reactions. *J. Chem. Phys.*, 15(5):261–267, 1947.

[24] C. Bina and A. Navrotsky. Possible presence of high-pressure ice in cold subducting slabs. *Nature*, 408:844, 2000.

[25] R. Biswas, W. Carpenter, J. Fournier, G. Voth, and A. Tokmakoff. Ir spectral assignments for the hydrated excess proton in liquid water. *J. Chem. Phys*, 146:154507, 2017.

[26] Marc Blanchard, Etienne Balan, and Edwin A Schauble. Equilibrium fractionation of non-traditional isotopes: a molecular modeling perspective. *Reviews in Mineralogy and Geochemistry*, 82(1):27–63, 2017.

[27] Salman Bloch and James L Bischoff. The effect of low-temperature alteration of basalt on the oceanic budget of potassium. *Geology*, 7(4):193–196, 1979.

[28] Lydéric Bocquet and Elisabeth Charlaix. Nanofluidics, from bulk to interfaces. *Chemical Society Reviews*, 39(3):1073–1095, 2010.

[29] L. Bove, S. Klotz, Th. Strässle, M. Koza, J. Teixeira, and A. M. Saitta. Translational and rotational diffusion in water in the gigapascal range. *Phys. Rev. Lett.*, 111:185901, 2013.

[30] Emiliano Brini, Christopher J Fennell, Marivi Fernandez-Serra, Barbara Hribar-Lee, Miha Luksic, and Ken A Dill. How water's properties are encoded in its molecular structure and energies. *Chemical reviews*, 117(19):12385–12414, 2017.

[31] Ivan Brovchenko and Alla Oleinikova. Multiple phases of liquid water. *ChemPhysChem*, 9(18):2660–2675, 2008.

[32] Andrei Buin and Radu Iftimie. Molecular polarizabilities in aqueous proton transfer reactions. *J. Chem. Phys.*, 131(23):234507, 2009.

[33] G. Bussi, D. Donadio, and M. Parrinello. Canonical sampling through velocity rescaling. *J. Chem. Phys.*, 126:14101, 2007.

[34] Marcos F Calegari Andrade, Hsin-Yu Ko, Roberto Car, and Annabella Selloni. Structure, polarization, and sum frequency generation spectrum of interfacial water on anatase Tio2. *J. Phys. Chem. Lett.*, 9(23):6716–6721, 2018.

[35] Richard Car and Mark Parrinello. Unified approach for molecular dynamics and density-functional theory. *Phys. Rev. Lett.*, 55(22):2471, 1985.

[36] Richard W Carlson. *The Mantle and Core: Treatise on Geochemistry, Volume 2*, volume 2. Elsevier, 2005.

[37] C. Cavazzoni, G. L. Chiarotti, S. Scandolo, E. Tosatti, M. Bernasconi, and M. Parrinello. Superionic and metallic states of water and ammonia at giant planet conditions. *Science*, 283:44, 1999.

[38] David M Ceperley and Berni J Alder. Ground state of the electron gas by a stochastic method. *Phys. Rev. Lett.*, 45(7):566, 1980.

[39] Michele Ceriotti, Wei Fang, Peter G Kusalik, Ross H McKenzie, Angelos Michaelides, Miguel A Morales, and Thomas E Markland. Nuclear quantum effects in water and aqueous systems: Experiment, theory, and current challenges. *Chemical reviews*, 116(13):7529–7550, 2016.

[40] M. Cerrioti, J. More, and D. Manolopoulos. i-pi: A python interface for ab initio path integral molecular dynamics simulations. *Comput. Phys. Commun.*, 185:1019–1026, 2014.

[41] Jeng-Da Chai and Martin Head-Gordon. Systematic optimization of long-range corrected hybrid density functionals. *J. Chem. Phys.*, 128(8):084106, 2008.

[42] Sudip Chakraborty, Hemant Kumar, Chandan Dasgupta, and Prabal K Maiti. Confined water: Structure, dynamics, and thermodynamics. *Accounts of chemical research*, 50(9):2139–2146, 2017.

[43] Jayaraman Chandrasekhar and William L Jorgensen. The nature of dilute solutions of sodium ion in water, methanol, and tetrahydrofuran. *J. Chem. Phys.*, 77(10):5080–5089, 1982.

[44] Jayaraman Chandrasekhar, David C Spellmeyer, and William L Jorgensen. Energy component analysis for dilute aqueous solutions of lithium (1+), sodium (1+), fluoride (1-), and chloride (1-) ions. *J. Am. Chem. Soc.*, 106(4):903–910, 1984.

[45] Heng Chen, Zhen Tian, Brenna Tuller-Ross, Randy L Korotev, and Kun Wang. High-precision potassium isotopic analysis by mc-icp-ms: an inter-laboratory comparison and refined k atomic weight. *Journal of Analytical Atomic Spectrometry*, 34(1):160–171, 2019.

[46] Ji Chen, Andrea Zen, Jan Gerit Brandenburg, Dario Alfè, and Angelos Michaelides. Evidence for stable square ice from quantum monte carlo. *Physical Review B*, 94(22):220102, 2016.

[47] Mohan Chen, Hsin-Yu Ko, Richard C Remsing, Marcos F Calegari Andrade, Biswajit Santra, Zhaoru Sun, Annabella Selloni, Roberto Car, Michael L Klein, John P Perdew, et al. Ab initio theory and modeling of water. *Proc. Natl. Acad. Sci. U.S.A.*, 114(41):10846–10851, 2017.

[48] Yixing Chen, Halil I Okur, Nikolaos Gomopoulos, Carlos Macias-Romero, Paul S Cremer, Poul B Petersen, Gabriele Tocci, David M Wilkins, Chungwen Liang, Michele Ceriotti, et al. Electrolytes induce long-range orientational order and free energy changes in the h-bond network of bulk water. *Science advances*, 2(4):e1501891, 2016.

[49] Giancarlo Cicero, Jeffrey C Grossman, Eric Schwegler, Francois Gygi, and Giulia Galli. Water confined in nanotubes and between graphene sheets: A first principle study. *J. Am. Chem. Soc.*, 130(6):1871–1878, 2008.

[50] Gerardo Andrés Cisneros, Kjartan Thor Wikfeldt, Lars Ojamae, Jibao Lu, Yao Xu, Hedieh Torabifard, Albert P Bartók, Gábor Csányi, Valeria Molinero, and Francesco Paesani. Modeling molecular interactions in water: From pairwise to many-body potential energy functions. *Chemical reviews*, 116(13):7501–7528, 2016.

[51] J Kirk Cochran, Henry J Bokuniewicz, and Patricia L Yager. *Encyclopedia of Ocean Sciences*. Academic Press, 2019.

[52] D. Corradini, F. Coudert, and R. Vuilleumier. Insight into the Li2CO3–K2CO3 eutectic mixture from classical molecular dynamics: Thermodynamics, structure, and dynamics. *J. Chem. Phys.*, 144:104507, 2016.

[53] F. Dahms, R. Costard, E. Pines, B. Fingerhut, E. Nibbering, and T Elsaesser. The hydrated excess proton in the zundel cation H5O2+: The role of ultrafast solvent fluctuations. *Ang. Chem. Int. Ed.*, 55:10600, 2016.

[54] C. Daly, L. Streacker, Y. Sun, S. Pattenaude, A. Hassanali, P. Petersen, S. Corcelli, and D. Ben-Amotz. Decomposition of the experimental raman and infrared spectra of acidic water into proton, special pair, and counterion contributions. *J. Phys. Chem. Lett.*, 8:5246, 2017.

[55] Liem X Dang, Gregory K Schenter, Vassiliki-Alexandra Glezakou, and John L Fulton. Molecular simulation analysis and x-ray absorption measurement of Ca2+, K+ and Cl- ions in solution, 2006.

[56] F. Datchi, P. Loubeyre, and R. LeToullec. Extended and accurate determination of the melting curves of argon, helium, ice (H2O), and hydrogen (H2). *Phys. Rev. B*, 61:6535, 2000.

[57] Nicolas Dauphas, Mathieu Roskosz, EE Alp, DC Golden, CK Sio, FLH Tissot, MY Hu, J Zhao, L Gao, and RV Morris. A general moment NRIXS approach to the determination of equilibrium Fe isotopic fractionation factors: application to goethite and jarosite. *Geochimica et Cosmochimica Acta*, 94:254–275, 2012.

[58] William Dawson and François Gygi. Equilibration and analysis of first-principles molecular dynamics simulations of water. *J. Chem. Phys.*, 148(12):124501, 2018.

[59] Pablo G Debenedetti, Francesco Sciortino, and Gül H Zerze. Second critical point in two realistic models of water. *Science*, 369(6501):289–292, 2020.

[60] C. Dellago, P. Geissler, D. Chandler, J. Hutter, and M. Parrinello. Comment on "Dissociation of Water under Pressure". *Phys. Rev. Lett.*, 89:199601, 2002.

[61] Robert V Demicco, Tim K Lowenstein, Lawrence A Hardie, and Ronald J Spencer. Model of seawater composition for the phanerozoic. *Geology*, 33(11):877–880, 2005.

[62] Ken A Dill, Thomas M Truskett, Vojko Vlachy, and Barbara Hribar-Lee. Modeling water, the hydrophobic effect, and ion solvation. *Annu. Rev. Biophys. Biomol. Struct.*, 34:173–199, 2005.

[63] Yun Ding, Ali A Hassanali, and Michele Parrinello. Anomalous water diffusion in salt solutions. *Proc. Natl. Acad. Sci. U.S.A.*, 111(9):3310–3315, 2014.

[64] Max Dion, Henrik Rydberg, Elsebeth Schröder, David C Langreth, and Bengt I Lundqvist. Van der Waals density functional for general geometries. *Phys. Rev. Lett.*, 92(24):246401, 2004.

[65] N. Dubrovinskaia and L. Dubrovinsky. Whole-cell heater for the diamond anvil cell. *Rev. Sci. Instrum.*, 74:3433, 2003.

[66] L. Dubrovinsky and N. Dubrovinskaia. Melting of ice VII and new high-pressure, high-temperature amorphous ice. *Geol. Soc. Am. Spec. Pap.*, 421:105, 2007.

[67] Manoj Ducher, Marc Blanchard, and Etienne Balan. Equilibrium isotopic fractionation between aqueous Zn and minerals from first-principles calculations. *Chemical Geology*, 483:342–350, 2018.

[68] A. Dunaeva, D. Antsyshkin, and O. Kuskov. Phase diagraom of h2o: Thermodynamic functions of the phase transitions of high-pressure ices. *Solar System Research*, 44:202, 2010.

[69] David Eisenberg, Walter Kauzmann, and Walter Kauzmann. *The structure and properties of water*. Oxford University Press on Demand, 2005.

[70] Loris Ercole, Aris Marcolongo, and Stefano Baroni. Accurate thermal conductivities from optimally short molecular dynamics simulations. *Scientific reports*, 7(1):1–11, 2017.

[71] Kerstin Falk, Felix Sedlmeier, Laurent Joly, Roland R Netz, and Lydéric Bocquet. Molecular origin of fast water transport in carbon nanotube membranes: superlubricity versus curvature dependent friction. *Nano letters*, 10(10):4067–4073, 2010.

[72] Samuel Faucher, Narayana Aluru, Martin Z Bazant, Daniel Blankschtein, Alexandra H Brozena, John Cumings, J Pedro de Souza, Menachem Elimelech, Razi Epsztein, John T Fourkas, et al. Critical knowledge gaps in mass transport through single-digit nanopores: a review and perspective. *J. Phys. Chem. C*, 123(35):21309–21326, 2019.

[73] Dionysis I Foustoukos. On the ionic strength and electrical conductivity of crustal brines. *Chemical Geology*, 447:183–190, 2016.

[74] M. Frank, Y. Fei, and J. Hu. Constraining the equation of state of fluid H2O to 80 GPa using the melting curve, bulk modulus, and thermal expansivity of ice vii. *Geochim. Cosmochim. Ac.*, 68:2781, 2004.

[75] F Franks. Water: a comprehensive treatise. volume 1. the physics and physical chemistry of water. 1972.

[76] Felix Franks. *Water: a matrix of life*. Royal Society of Chemistry, 2007.

[77] Felix Franks. *The physics and physical chemistry of water*, volume 1. Springer Science & Business Media, 2012.

[78] M. French, S. Hamel, and R. Redmer. Dynamical screening and ionic conductivity in water from ab initio simulations. *Phys. Rev. Lett.*, 107:185901, 2011.

[79] M. French, T. Mattsson, and R. Redmer. Diffusion and electrical conductivity in water at ultrahigh pressures. *Phys. Rev. B.*, 82:174108, 2010.

[80] M. French and R. Redmer. Estimating the quantum effects from molecular vibrations of water under high pressures and temperatures. *J. Phys. Condens. Mat.*, 21:6059, 2009.

[81] Martin French, Michael P Desjarlais, and Ronald Redmer. Ab initio calculation of thermodynamic potentials and entropies for superionic water. *Physical Review E*, 93(2):022140, 2016.

[82] O Fuchs, M Zharnikov, L Weinhardt, M Blum, M Weigand, Y Zubavichus, M Bär, F Maier, JD Denlinger, C Heske, et al. Isotope and temperature effects in liquid water probed by x-ray absorption and resonant x-ray emission spectroscopy. *Phys. Rev. Lett.*, 100(2):027801, 2008.

[83] Laura Fumagalli, Ali Esfandiar, Rene Fabregas, S Hu, Pablo Ares, Amritha Janardanan, Q Yang, Boya Radha, Takashi Taniguchi, K Watanabe, et al. Anomalously low dielectric constant of confined water. *Science*, 360(6395):1339–1342, 2018.

[84] Stefan Funkner, Gudrun Niehues, Diedrich A Schmidt, Matthias Heyden, Gerhard Schwaab, Karen M Callahan, Douglas J Tobias, and Martina Havenith. Watching the low-frequency motions in aqueous salt solutions: The terahertz vibrational signatures of hydrated ions. *J. Am. Chem. Soc.*, 134(2):1030–1035, 2011.

[85] Alex P Gaiduk and Giulia Galli. Local and global effects of dissolved sodium chloride on the structure of water. *J. Phys. Chem. Lett.*, 8(7):1496–1502, 2017.

[86] Alex P Gaiduk, Jeffrey Gustafson, Francois Gygi, and Giulia Galli. First-principles simulations of liquid water using a dielectric-dependent hybrid functional. *J. Phys. Chem. Lett.*, 9(11):3068–3073, 2018.

[87] Alex P Gaiduk, Tuan Anh Pham, Marco Govoni, Francesco Paesani, and Giulia Galli. Electron affinity of liquid water. *Nature communications*, 9(1):247, 2018.

[88] Alex P Gaiduk, Cui Zhang, François Gygi, and Giulia Galli. Structural and electronic properties of aqueous NaCl solutions from ab initio molecular dynamics simulations with hybrid density functionals. *Chemical Physics Letters*, 604:89–96, 2014.

[89] Matthieu E Galvez, Craig E Manning, James AD Connolly, and Douglas Rumble. The solubility of rocks in metamorphic fluids: A model for rock-dominated conditions to upper mantle pressure and temperature. *Earth and Planetary Science Letters*, 430:486–498, 2015.

[90] V Garbuio, M Cascella, L Reining, R Del Sole, and O Pulci. Ab initio calculation of optical spectra of liquids: many-body effects in the electronic excitations of water. *Phys. Rev. Lett.*, 97(13):137402, 2006.

[91] Piero Gasparotto and Michele Ceriotti. Recognizing molecular patterns by machine learning: An agnostic structural definition of the hydrogen bond. *J. Chem. Phys.*, 141(17):174110, 2014.

[92] Xiaochuan Ge and Deyu Lu. Molecular polarizability of water from local dielectric response theory. *Physical Review B*, 96(7):075114, 2017.

[93] Paolo Giannozzi, Stefano Baroni, Nicola Bonini, Matteo Calandra, Roberto Car, Carlo Cavazzoni, Davide Ceresoli, Guido L Chiarotti, Matteo Cococcioni, Ismaila Dabo, et al. Quantum espresso: a modular and open-source software project for quantum simulations of materials. *Journal of physics: Condensed matter*, 21(39):395502, 2009.

[94] F. Giberti and A. Hassanali. The excess proton at the air-water interface: The role of instantaneous liquid interfaces. *J. Chem. Phys.*, 146:244703, 2017.

[95] Michael J Gillan, Dario Alfè, and Angelos Michaelides. Perspective: How good is dft for water? *J. Chem. Phys.*, 144(13):130901, 2016.

[96] Vassiliki-Alexandra Glezakou, Yongsheng Chen, John L Fulton, Gregory K Schenter, and Liem X Dang. Electronic structure, statistical mechanical simulations, and exafs spectroscopy of aqueous potassium. *Theoretical Chemistry Accounts*, 115(2-3):86–99, 2006.

[97] N. Goldman, E. Reed, L. Kuo, L. Fried, C. Mundy, and A. Curioni. Ab initio simulation of the equation of state and kinetics of shocked water. *J. Chem. Phys.*, 130:124517, 2009.

[98] A. Goncharov, N. Goldman, L. Fried, J. Crowhurst, I. Kuo, C. Mundy, and J. Zaug. Dynamic ionization of water under extreme conditions. *Phys. Rev. Lett.*, 94:125508, 2005.

[99] A. Goncharov, C. Sanloup, N. Goldman, J. Crowhurst, S. Bastea, W. Howard, L. Fried, N. Guignot, M. Mezouar, and Y. Meng. Dissociative melting of ice vii at high pressure. *J. Chem. Phys.*, 130:124514, 2009.

[100] N Grevesse and AJ Sauval. Standard solar composition. *Space Science Reviews*, 85(1-2):161–174, 1998.

[101] Ronald Wilfrid Gurney and Ronald W Gurney. Ionic processes in solution. 1953.

[102] M. Guthrie, R. Boehler, C. Tulk, J. Molaison, A. dos Santos, and R. Hemley. Neutron diffraction observations of interstitial protons in dense ice. *P. Natl. Acad. Sci. USA*, 110:10552, 2013.

[103] F. Gygi, J-L. Fattebert, and E. Schwegler. Computation of maximally localized wannier functions using a simultaneous diagonalization algorithm. *Comput. Phys. Commun.*, 155:1–6, 2003.

[104] Francois Gygi. Architecture of qbox: A scalable first-principles molecular dynamics code. *IBM Journal of Research and Development*, 52(1.2):137–144, 2008.

[105] François Gygi, Jean-Luc Fattebert, and Eric Schwegler. Computation of maximally localized wannier functions using a simultaneous diagonalization algorithm. *Computer physics communications*, 155(1):1–6, 2003.

[106] Scott Habershon, George S Fanourgakis, and David E Manolopoulos. Comparison of path integral molecular dynamics methods for the infrared absorption spectrum of liquid water. *J. Chem. Phys.*, 129(7):074501, 2008.

[107] D. Hamann, M. Schluter, and C. Chiang. Norm-conserving pseudopotentials. *Phys. Rev. Lett.*, 43:1494, 1979.

[108] Ali A Hassanali, Jérôme Cuny, Vincenzo Verdolino, and Michele Parrinello. Aqueous solutions: state of the art in ab initio molecular dynamics. *Philosophical Transactions of the Royal Society A: Mathematical, Physical and Engineering Sciences*, 372(2011):20120482, 2014.

[109] Zhongjin He, Jian Zhou, Xiaohua Lu, and Ben Corry. Ice-like water structure in carbon nanotube (8, 8) induces cationic hydration enhancement. *J. Phys. Chem. C*, 117(21):11412–11420, 2013.

[110] Robert J Heaton, Paul A Madden, Stewart J Clark, and Sandro Jahn. Condensed phase ionic polarizabilities from plane wave density functional theory calculations. *J. Chem. Phys.*, 125(14):144104, 2006.

[111] Jochen Heyd, Gustavo E Scuseria, and Matthias Ernzerhof. Hybrid functionals based on a screened coulomb potential. *J. Chem. Phys.*, 118(18):8207–8215, 2003.

[112] H. Hirai, H. Kadobayashi, T. Matsuoka, Y. Ohishi, and Y. Yamamoto. High pressure x-ray diffraction and raman spectroscopic studies of the phase change of D2O ice VII at approximately 11 GPa. *High Pressure Research*, 34:289, 2014.

[113] Pierre Hohenberg and Walter Kohn. Inhomogeneous electron gas. *Physical review*, 136(3B):B864, 1964.

[114] N. Holmes, W. Nellis, W. Graham, and G. Walrafen. Spontaneous raman scattering from shocked water. *Phys. Rev. Lett.*, 55:2433, 1985.

[115] Yan Hu, Xin-Yang Chen, Ying-Kui Xu, and Fang-Zhen Teng. High-precision analysis of potassium isotopes by hr-mc-icpms. *Chemical Geology*, 493:100–108, 2018.

[116] F Huang, P Chakraborty, CC Lundstrom, C Holmden, JJG Glessner, SW Kieffer, and CE Lesher. Isotope fractionation in silicate melts by thermal diffusion. *Nature*, 464(7287):396–400, 2010.

[117] W. B. Hubbard, W. J. Nellis, A. C. Mitchell, N. C. Holmes, S. S. Limaye, and P. C. McCandless. Interior structure of neptune: Comparison with uranus. *Science*, 253:648, 1991.

[118] Munir Humayun and Robert N Clayton. Potassium isotope cosmochemistry: Genetic implications of volatile element depletion. *Geochimica et Cosmochimica Acta*, 59(10):2131–2148, 1995.

[119] M Ichiki, K Baba, H Toh, and K Fuji-Ta. An overview of electrical conductivity structures of the crust and upper mantle beneath the northwestern pacific, the japanese islands, and continental east asia. *Gondwana Research*, 16(3-4):545–562, 2009.

[120] Sumio Iijima. Helical microtubules of graphitic carbon. *nature*, 354(6348):56–58, 1991.

[121] T. Ikeda. Infrared absorption and raman scattering spectra of water under pressure via first principles molecular dynamics. *J. Chem. Phys.*, 141:44501, 2014.

[122] T. Ikeda, Y. Katayama, H. Saitoh, and K. Aoki. High temperature water under pressure. *J. Chem. Phys.*, 132:121102, 2010.

[123] Takashi Ikeda, Mauro Boero, and Kiyoyuki Terakura. Hydration of alkali ions from first principles molecular dynamics revisited. *J. Chem. Phys.*, 126(3):01B611, 2007.

[124] R. Janoschek, E. Weidemann, and G. Zundel. Calculated frequencies and intensities associated with coupling of the proton motion with the hydrogen bond stretching vibration in a double minimum potential surface. *J. Chem. Soc., Faraday Trans. 2.*, 69:505, 1972.

[125] William L Jorgensen. Quantum and statistical mechanical studies of liquids. 10. transferable intermolecular potential functions for water, alcohols, and ethers. application to liquid water. *J. Am. Chem. Soc.*, 103(2):335–340, 1981.

[126] Iina Juurinen, Tuomas Pylkkanen, Kari O Ruotsalainen, Christoph J Sahle, Giulio Monaco, Keijo Hamalainen, Simo Huotari, and Mikko Hakala. Saturation behavior in x-ray raman scattering spectra of aqueous licl. *J. Phys. Chem. B*, 117(51):16506–16511, 2013.

[127] ZR Kann and JL Skinner. A scaled-ionic-charge simulation model that reproduces enhanced and suppressed water diffusion in aqueous salt solutions. *J. Chem. Phys.*, 141(10):104507, 2014.

[128] P. Kelemen and C. Manning. Reevaluating carbon fluxes in subduction zones, what goes down mostly comes up. *P. Natl. Acad. Sci. USA*, 112:3997, 2015.

[129] Sharif Md Khan, Sharifa Faraezi, Yoshifumi Oya, Kenji Hata, and Tomonori Ohba. Anomalous changes of intermolecular distance in aqueous electrolytes in narrow pores of carbon nanotubes. *Adsorption*, pages 1–8, 2019.

[130] Jun Soo Kim, Zhe Wu, Andrew R Morrow, Anand Yethiraj, and Arun Yethiraj. Self-diffusion and viscosity in electrolyte solutions. *J. Phys. Chem. B*, 116(39):12007–12013, 2012.

[131] Jun Soo Kim and Arun Yethiraj. A diffusive anomaly of water in aqueous sodium chloride solutions at low temperatures. *J. Phys. Chem. B*, 112(6):1729–1735, 2008.

[132] T. Kimura, Y. Kuwayama, and T. Yagi. Melting temperatures of H2O up to 72 GPa measured in a diamond anvil cell using CO2 laser heating technique. *J. Chem. Phys.*, 140:074501, 2014.

[133] Kenichiro Koga, GT Gao, Hideki Tanaka, and Xiao Cheng Zeng. Formation of ordered ice nanotubes inside carbon nanotubes. *Nature*, 412(6849):802, 2001.

[134] Mateus H Köhler, José R Bordin, Carolina F de Matos, and Marcia C Barbosa. Water in nanotubes: The surface effect. *Chemical Engineering Science*, 2019.

[135] Walter Kohn and Lu Jeu Sham. Self-consistent equations including exchange and correlation effects. *Physical review*, 140(4A):A1133, 1965.

[136] Peter A Kollman and Leland C Allen. Theory of the hydrogen bond. *Chemical Reviews*, 72(3):283–303, 1972.

[137] Masato Kondoh, Yasuhiro Ohshima, and Masaaki Tsubouchi. Ion effects on the structure of water studied by terahertz time-domain spectroscopy. *Chemical Physics Letters*, 591:317–322, 2014.

[138] Gennadii Alekseevich Krestov. *Thermodynamics of solvation*. Ellis Horwood, 1991.

[139] BI Kronberg. Weathering dynamics and geosphere mixing with reference to the potassium cycle. *Physics of the earth and planetary interiors*, 41(2-3):125–132, 1985.

[140] Heather J Kulik, Eric Schwegler, and Giulia Galli. Probing the structure of salt water under confinement with first-principles molecular dynamics and theoretical x-ray absorption spectroscopy. *J. Phys. Chem. Lett.*, 3(18):2653–2658, 2012.

[141] Michael D LaCount and François Gygi. Ensemble first-principles molecular dynamics simulations of water using the scan meta-gga density functional. *J. Chem. Phys.*, 151(16):164101, 2019.

[142] Teodoro Laino and Jürg Hutter. Notes on "ewald summation of electrostatic multipole interactions up to quadrupolar level"[J. Chem. Phys. 119, 7471 (2003)]. *J. Chem. Phys.*, 129(7):074102, 2008.

[143] Guillaume Lamoureux, Alexander D MacKerell Jr, and Benoıt Roux. A simple polarizable model of water based on classical drude oscillators. *J. Chem. Phys.*, 119(10):5185–5197, 2003.

[144] Kyuho Lee, Éamonn D Murray, Lingzhu Kong, Bengt I Lundqvist, and David C Langreth. Higher-accuracy van der Waals density functional. *Physical Review B*, 82(8):081101, 2010.

[145] Shilei Li, Weiqiang Li, Brian L Beard, Maureen E Raymo, Xiaomin Wang, Yang Chen, and Jun Chen. K isotopes as a tracer for continental weathering and geological k cycling. *Proc. Natl. Acad. Sci. U.S.A.*, 116(18):8740–8745, 2019.

[146] Weiqiang Li, Brian L Beard, and Shilei Li. Precise measurement of stable potassium isotope ratios using a single focusing collision cell multi-collector icp-ms. *Journal of Analytical Atomic Spectrometry*, 31(4):1023–1029, 2016.

[147] Weiqiang Li, Kideok D Kwon, Shilei Li, and Brian L Beard. Potassium isotope fractionation between k-salts and saturated aqueous solutions at room temperature: Laboratory experiments and theoretical calculations. *Geochimica et Cosmochimica Acta*, 214:1–13, 2017.

[148] David R Lide. *CRC handbook of chemistry and physics: a ready-reference book of chemical and physical data*. CRC press, 1995.

[149] T. Light, S. Licht, A. Bevilacqua, and K. Morash. The fundamental conductivity and resistivity of water. *Electrochem. Solid-State Lett.*, 8:E16, 2005.

[150] J. Lin, E. Gregoryanz, V. Struzhkin, M. Somayazulu, H. Mao, and R. Hemley. Melting behavior of h2o at high pressures and temperatures. *Geophysical Research Letters*, 32:11306, 2005.

[151] J. Lin, B. Militzer, V. Struzhkin, E. Gregoryanz, R. Hemley, and H. Mao. High pressure-temperature Raman measurements of H2O melting to 22 GPa and 900 K. *J. Chem. Phys*, 121:8423, 2004.

[152] Jian Liu, Richard S Andino, Christina M Miller, Xin Chen, David M Wilkins, Michele Ceriotti, and David E Manolopoulos. A surface-specific isotope effect in mixtures of light and heavy water. *J. Phys. Chem. C*, 117(6):2944–2951, 2013.

[153] Katharina Lodders. Solar system abundances and condensation temperatures of the elements. *The Astrophysical Journal*, 591(2):1220, 2003.

[154] D. Long. *The Raman Effect: A Unified Treatment of the Theory of Raman Scattering by Molecules*. John Wiley Sons, New York, 2002.

[155] A. Luzar and D. Chandler. Hydrogen-bond kinetics in liquid water. *Nature.*, 379:55, 1996.

[156] Alenka Luzar and David Chandler. Effect of environment on hydrogen bond dynamics in liquid water. *Phys. Rev. Lett.*, 76(6):928, 1996.

[157] G. Lyzenga, Thomas J. Ahrens, W. J. Nellis, and A. C. Mitchell. The temperature of shock-compressed water. *J. Chem. Phys.*, 76:6282–6286, 1982.

[158] GD Mahan. Modified sternheimer equation for polarizability. *Physical Review A*, 22(5):1780, 1980.

[159] Mainak Majumder, Nitin Chopra, Rodney Andrews, and Bruce J Hinds. Nanoscale hydrodynamics: enhanced flow in carbon nanotubes. *Nature*, 438(7064):44, 2005.

[160] R Mancinelli, A Botti, F Bruni, MA Ricci, and AK Soper. Hydration of sodium, potassium, and chloride ions in solution and the concept of structure maker/breaker. *J. Phys. Chem. B*, 111(48):13570–13577, 2007.

[161] R Mancinelli, A Botti, F Bruni, MA Ricci, and AK Soper. Perturbation of water structure due to monovalent ions in solution. *Physical Chemistry Chemical Physics*, 9(23):2959–2967, 2007.

[162] Manoel Manghi, John Palmeri, Khadija Yazda, François Henn, and Vincent Jourdain. Role of charge regulation and flow slip in the ionic conductance of nanopores: An analytical approach. *Physical Review E*, 98(1):012605, 2018.

[163] David J Mann and Mathew D Halls. Water alignment and proton conduction inside carbon nanotubes. *Phys. Rev. Lett.*, 90(19):195503, 2003.

[164] Craig E Manning. Fluids of the lower crust: deep is different. *Annual Review of Earth and Planetary Sciences*, 46:67–97, 2018.

[165] Yizhak Marcus. Effect of ions on the structure of water: structure making and breaking. *Chemical reviews*, 109(3):1346–1370, 2009.

[166] Thomas E Markland and Michele Ceriotti. Nuclear quantum effects enter the mainstream. *Nature Reviews Chemistry*, 2(3):1–14, 2018.

[167] Ondrej Marsalek and Thomas E Markland. Ab initio molecular dynamics with nuclear quantum effects at classical cost: Ring polymer contraction for density functional theory. *J. Chem. Phys.*, 144(5):054112, 2016.

[168] Ondrej Marsalek and Thomas E Markland. Quantum dynamics and spectroscopy of ab initio liquid water: The interplay of nuclear and electronic quantum effects. *J. Phys. Chem. Lett.*, 8(7):1545–1551, 2017.

[169] Dominik Marx and Jürg Hutter. *Ab initio molecular dynamics: basic theory and advanced methods*. Cambridge University Press, 2009.

[170] N. Marzari and D. Vanderbilt. Maximally localized generalized wannier functions for composite energy bands. *Phys. Rev. B.*, 56:12847–12865, 1997.

[171] Nicola Marzari, Arash A Mostofi, Jonathan R Yates, Ivo Souza, and David Vanderbilt. Maximally localized wannier functions: Theory and applications. *Reviews of Modern Physics*, 84(4):1419, 2012.

[172] T. Mattsson and M. Desjarlais. Phase diagram and electrical conductivity of high energy-density water from density functional theory. *Phys. Rev. Lett.*, 97:017801, 2006.

[173] R Shane McGary, Rob L Evans, Philip E Wannamaker, Jimmy Elsenbeck, and Stéphane Rondenay. Pathway from subducting slab to surface for melt and fluids beneath mount rainier. *Nature*, 511(7509):338–340, 2014.

[174] D McQuarrie. A., 1976, Statistical Mechanics.

[175] Marius Millot, Sebastien Hamel, J Ryan Rygg, Peter M Celliers, Gilbert W Collins, Federica Coppari, Dayne E Fratanduono, Raymond Jeanloz, Damian C Swift, and Jon H Eggert. Experimental evidence for superionic water ice using shock compression. *Nature Physics*, 14(3):297–302, 2018.

[176] A. Mitchell and W. Nellis. Equation of state and electrical conductivity of water and ammonia shocked to the 100 GPa (1 Mbar) pressure range. *J. Chem. Phys.*, 76:6273, 1982.

[177] John J Molina, Sébastien Lectez, Sami Tazi, Mathieu Salanne, Jean-François Dufrêche, Jérôme Roques, Eric Simoni, Paul A Madden, and Pierre Turq. Ions in solutions: Determining their polarizabilities from first-principles. *J. Chem. Phys.*, 134(1):014511, 2011.

[178] Sayantan Mondal and Biman Bagchi. Water in carbon nanotubes: Pronounced anisotropy in dielectric dispersion and its microscopic origin. *J. Phys. Chem. Lett.*, 10(20):6287–6292, 2019.

[179] F Moučka, S Zamfir, D Bratko, and A Luzar. Molecular polarizability in open ensemble simulations of aqueous nanoconfinements under electric field. *J. Chem. Phys.*, 150(16):164702, 2019.

[180] KJ Müller and HG Hertz. A parameter as an indicator for water- water association in solutions of strong electrolytes. *J. Phys. Chem-US*, 100(4):1256–1265, 1996.

[181] Lars-Åke Näslund, David C Edwards, Philippe Wernet, Uwe Bergmann, Hirohito Ogasawara, Lars GM Pettersson, Satish Myneni, and Anders Nilsson. X-ray absorption spectroscopy study of the hydrogen bond network in the bulk water of aqueous solutions. *J. Phys. Chem. A*, 109(27):5995–6002, 2005.

[182] M. Nishi, T. Irifune, J. Tsuchiya, Y. Tange, Y. Nishihara, K. Fujino, and Y. Higo. Stability of hydrous silicate at high pressures and water transport to the deep lower mantle. *Nat. Geosci.*, 7:224, 2014.

[183] Abraham Nitzan. *Chemical dynamics in condensed phases: relaxation, transfer and reactions in condensed molecular systems*. Oxford University Press, 2006.

[184] Thomas M Nymand and Per Linse. Ewald summation and reaction field methods for potentials with atomic charges, dipoles, and polarizabilities. *J. Chem. Phys.*, 112(14):6152–6160, 2000.

[185] Tomonori Ohba, Kenji Hata, and Hirofumi Kanoh. Significant hydration shell formation instead of hydrogen bonds in nanoconfined aqueous electrolyte solutions. *J. Am. Chem. Soc.*, 134(43):17850–17853, 2012.

[186] Hitoshi Ohtaki and Tamas Radnai. Structure and dynamics of hydrated ions. *Chemical Reviews*, 93(3):1157–1204, 1993.

[187] T. Okada, T. Iitaka, T. Yagi, and K. Aoki. Electrical conductivity of ice vii. *Scientific Reports*, 4:5778, 2014.

[188] Anne Willem Omta, Michel F Kropman, Sander Woutersen, and Huib J Bakker. Negligible effect of ions on the hydrogen-bond structure in liquid water. *Science*, 301(5631):347–349, 2003.

[189] Jeremy T O'Brien, James S Prell, Matthew F Bush, and Evan R Williams. Sulfate ion patterns water at long distance. *J. Am. Chem. Soc.*, 132(24):8248–8249, 2010.

[190] Francesco Paesani and Gregory A Voth. The properties of water: Insights from quantum simulations. *J. Phys. Chem. B*, 113(17):5702–5719, 2009.

[191] Francesco Paesani, Sotiris S Xantheas, and Gregory A Voth. Infrared spectroscopy and hydrogen-bond dynamics of liquid water from centroid molecular dynamics with an ab initio-based force field. *J. Phys. Chem. B*, 113(39):13118–13130, 2009.

[192] D. Pan and G. Galli. The fate of carbon dioxide in water-rich fluids in the earth's mantle. *Sci. Adv.*, 2:1601278, 2016.

[193] D. Pan, L. Spanu, B. Harrison, D. Sverjensky, and G. Galli. Dielectric properties of water under extreme conditions and transport of carbonates in the deep earth. *P. Natl. Acad. Sci. USA*, 110:6646, 2013.

[194] D. Pan, Q. Wan, and G. Galli. The refractive index and electronic gap of water and ice increase with increasing pressure. *Nat. Commun.*, 5:3919, 2014.

[195] Ding Pan, Marco Govoni, and Giulia Galli. Communication: Dielectric properties of condensed systems composed of fragments. *J. Chem. Phys.*, 149(5):051101, 2018.

[196] Christopher A Parendo, Stein B Jacobsen, and Kun Wang. K isotopes as a tracer of seafloor hydrothermal alteration. *Proc. Natl. Acad. Sci. U.S.A.*, 114(8):1827–1831, 2017.

[197] Dietmar Paschek and Ralf Ludwig. Specific ion effects on water structure and dynamics beyond the first hydration shell. *Angewandte Chemie International Edition*, 50(2):352–353, 2011.

[198] J. Perdew, K. Burke, and M. Ernzerhof. Generalized gradient approximation made simple. *Phys. Rev. Lett.*, 77:3865, 1999.

[199] John P Perdew, Kieron Burke, and Matthias Ernzerhof. Generalized gradient approximation made simple. *Phys. Rev. Lett.*, 77(18):3865, 1996.

[200] John P Perdew, Matthias Ernzerhof, and Kieron Burke. Rationale for mixing exact exchange with density functional approximations. *J. Chem. Phys.*, 105(22):9982–9985, 1996.

[201] John P Perdew and Yue Wang. Accurate and simple analytic representation of the electron-gas correlation energy. *Physical review B*, 45(23):13244, 1992.

[202] Lars Gunnar Moody Pettersson, Richard Humfry Henchman, and Anders Nilsson. Water the most anomalous liquid, 2016.

[203] T Anh Pham, Cui Zhang, Eric Schwegler, and Giulia Galli. Probing the electronic structure of liquid water with many-body perturbation theory. *Physical Review B*, 89(6):060202, 2014.

[204] Tuan Anh Pham, SM Golam Mortuza, Brandon C Wood, Edmond Y Lau, Tadashi Ogitsu, Steven F Buchsbaum, Zuzanna S Siwy, Francesco Fornasiero, and Eric Schwegler. Salt solutions in carbon nanotubes: The role of cation- π interactions. *J. Phys. Chem. C*, 120(13):7332–7338, 2016.

[205] VB Polyakov, SD Mineev, RN Clayton, G Hu, VM Gurevich, DA Khramov, KS Gavrichev, VE Gorbunov, and LN Golushina. Oxygen isotope fractionation factors involving cassiterite (sno2): I. calculation of reduced partition function ratios from heat capacity and x-ray resonant studies. *Geochimica et cosmochimica acta*, 69(5):1287–1300, 2005.

[206] John Anthony Pople. Molecular association in liquids ii. a theory of the structure of water. *Proceedings of the Royal Society of London. Series A. Mathematical and Physical Sciences*, 205(1081):163–178, 1951.

[207] David Prendergast and Giulia Galli. X-ray absorption spectra of water from first principles calculations. *Phys. Rev. Lett.*, 96(21):215502, 2006.

[208] Ph Pruzan. Pressure effects on the hydrogen bond in ice up to 80 GPa. *Journal of molecular structure*, 322:279–286, 1994.

[209] A. Putrino and M. Parrinello. Anharmonic raman spectra in high-pressure ice from ab initio simulations. *Phys. Rev. Lett.*, 88:176401, 2002.

[210] Tuomas Pylkkanen, Arto Sakko, Mikko Hakala, Keijo Hamalainen, Giulio Monaco, and Simo Huotari. Temperature dependence of the near-edge spectrum of water. *J. Phys. Chem. B*, 115(49):14544–14550, 2011.

[211] Wenpeng Qi, Jige Chen, Junwei Yang, Xiaoling Lei, Bo Song, and Haiping Fang. Anisotropic dielectric relaxation of the water confined in nanotubes for terahertz spectroscopy studied by molecular dynamics simulations. *J. Phys. Chem. B*, 117(26):7967–7971, 2013.

[212] Wenpeng Qi and Hongwei Zhao. Hydrogen bond network in the hydration layer of the water confined in nanotubes increasing the dielectric constant parallel along the nanotube axis. *J. Chem. Phys.*, 143(11):114708, 2015.

[213] Aneesur Rahman and Frank H Stillinger. Molecular dynamics study of liquid water. *J. Chem. Phys.*, 55(7):3336–3359, 1971.

[214] Muralikrishna Raju, Adri Van Duin, and Matthias Ihme. Phase transitions of ordered ice in graphene nanocapillaries and carbon nanotubes. *Scientific reports*, 8(1):3851, 2018.

[215] R. Ramierez, T. Lopez-Ciudad, P. Kumar, and D. Marx. Quantum corrections to classical time-correlation functions: hydrogen bonding and anharmonic floppy modes. *J. Chem. Phys.*, 121:3973, 2004.

[216] Danielle P Santiago Ramos, Leah E Morgan, Nicholas S Lloyd, and John A Higgins. Reverse weathering in marine sediments and the geochemical cycle of potassium in seawater: Insights from the k isotopic composition (41k/39k) of deep-sea pore-fluids. *Geochimica et Cosmochimica Acta*, 236:99–120, 2018.

[217] Sandeep K Reddy, Shelby C Straight, Pushp Bajaj, C Huy Pham, Marc Riera, Daniel R Moberg, Miguel A Morales, Chris Knight, Andreas W Götz, and Francesco Paesani. On the accuracy of the mb-pol many-body potential for water: Interaction energies, vibrational frequencies, and classical thermodynamic and dynamical properties from clusters to liquid water and ice. *J. Chem. Phys.*, 145(19):194504, 2016.

[218] Ronald Redmer, Thomas R Mattsson, Nadine Nettelmann, and Martin French. The phase diagram of water and the magnetic fields of uranus and neptune. *Icarus*, 211(1):798–803, 2011.

[219] Pengyu Ren and Jay W Ponder. Polarizable atomic multipole water model for molecular mechanics simulation. *J. Phys. Chem. B*, 107(24):5933–5947, 2003.

[220] Richard Renou, A Szymczyk, and Aziz Ghoufi. Tunable dielectric constant of water at the nanoscale. *Physical Review E*, 91(3):032411, 2015.

[221] Raffaele Resta. Macroscopic polarization in crystalline dielectrics: the geometric phase approach. *Reviews of modern physics*, 66(3):899, 1994.

[222] Wilhelm Conrad Röntgen. Ueber die constitution des flüssigen wassers. *Annalen der Physik*, 281(1):91–97, 1892.

[223] Viktor Rozsa, Ding Pan, Federico Giberti, and Giulia Galli. Ab initio spectroscopy and ionic conductivity of water under earth mantle conditions. *Proc. Natl. Acad. Sci. U.S.A.*, 115(27):6952–6957, 2018.

[224] RL Rudnick and S Gao. Composition of the continental crust. *The crust*, 3:1–64, 2003.

[225] F Rull. Structural investigation of water and aqueous solutions by raman spectroscopy. *Pure and applied chemistry*, 74(10):1859–1870, 2002.

[226] Subin Sahu, Massimiliano Di Ventra, and Michael Zwolak. Dehydration as a universal mechanism for ion selectivity in graphene and other atomically thin pores. *Nano letters*, 17(8):4719–4724, 2017.

[227] Subin Sahu and Michael Zwolak. Ionic selectivity and filtration from fragmented dehydration in multilayer graphene nanopores. *Nanoscale*, 9(32):11424–11428, 2017.

[228] Hiroshi Sakuma and Masahiro Ichiki. Electrical conductivity of NaCl-H2O fluid in the crust. *Journal of Geophysical Research: Solid Earth*, 121(2):577–594, 2016.

[229] Mathieu Salanne, Rodolphe Vuilleumier, Paul A Madden, Christian Simon, Pierre Turq, and Bertrand Guillot. Polarizabilities of individual molecules and ions in liquids from first principles. *Journal of Physics: Condensed Matter*, 20(49):494207, 2008.

[230] Christian Schaaf and Stephan Gekle. Spatially resolved dielectric constant of confined water and its connection to the non-local nature of bulk water. *J. Chem. Phys.*, 145(8):084901, 2016.

[231] Diedrich A Schmidt, Roberto Scipioni, and Mauro Boero. Water solvation properties: an experimental and theoretical investigation of salt solutions at finite dilution. *J. Phys. Chem. A*, 113(27):7725–7729, 2009.

[232] Christoph Schran, Ondrej Marsalek, and Thomas E Markland. Unravelling the influence of quantum proton delocalization on electronic charge transfer through the hydrogen bond. *Chemical Physics Letters*, 678:289–295, 2017.

[233] Simon Schreck, Martin Beye, Jonas A Sellberg, Trevor McQueen, Hartawan Laksmono, Brian Kennedy, Sebastian Eckert, Daniel Schlesinger, Dennis Nordlund, Hirohito Ogasawara, et al. Reabsorption of soft x-ray emission at high x-ray free-electron laser fluences. *Phys. Rev. Lett.*, 113(15):153002, 2014.

[234] B. Schwager and R. Boehler. H2o: another ice phase and its melting curve. *High Pressure Res.*, 28:431, 2008.

[235] B. Schwager, L. Chudinovskikh, A. Gavriliuk, and R. Boehler. Melting curve of H2O to 90 GPa measured in laser-heated diamond cell. *J. Phys. Condens. Matt.*, 16:S1177, 2004.

[236] E. Schwegler, G. Galli, and F. Gygi. Water under pressure. *Phys. Rev. Lett.*, 84:2429, 2000.

[237] E. Schwegler, G. Galli, F. Gygi, and R. Hood. Dissociation of water under pressure. *Phys. Rev. Lett.*, 87:265501, 2001.

[238] E. Schwegler, M. Sharma, F. Gygi, and G. Galli. Melting of ice under pressure. *P. Natl. Acad. Sci. USA*, 105:14779, 2008.

[239] Eric Schwegler, Jeffrey C Grossman, François Gygi, and Giulia Galli. Towards an assessment of the accuracy of density functional theory for first principles simulations of water. ii. *J. Chem. Phys.*, 121(11):5400–5409, 2004.

[240] Jonas A Sellberg, C Huang, Trevor A McQueen, ND Loh, H Laksmono, Daniel Schlesinger, RG Sierra, D Nordlund, CY Hampton, Dmitri Starodub, et al. Ultrafast x-ray probing of water structure below the homogeneous ice nucleation temperature. *Nature*, 510(7505):381–384, 2014.

[241] Farzaneh Shayeganfar, Javad Beheshtian, and Rouzbeh Shahsavari. First-principles study of water nanotubes captured inside carbon/boron nitride nanotubes. *Langmuir*, 34(37):11176–11187, 2018.

[242] Pier Luigi Silvestrelli, Nicola Marzari, David Vanderbilt, and Michele Parrinello. Maximally-localized wannier functions for disordered systems: Application to amorphous silicon. *Solid State Communications*, 107(1):7–11, 1998.

[243] Pier Luigi Silvestrelli and Michele Parrinello. Structural, electronic, and bonding properties of liquid water from first principles. *J. Chem. Phys.*, 111(8):3572–3580, 1999.

[244] Pier Luigi Silvestrelli and Michele Parrinello. Water molecule dipole in the gas and in the liquid phase. *Phys. Rev. Lett.*, 82(16):3308, 1999.

[245] James L Skinner. Following the motions of water molecules in aqueous solutions. *Science*, 328(5981):985–986, 2010.

[246] Lawrie B Skinner, Congcong Huang, Daniel Schlesinger, Lars GM Pettersson, Anders Nilsson, and Chris J Benmore. Benchmark oxygen-oxygen pair-distribution function of ambient water from x-ray diffraction measurements with a wide q-range. *J. Chem. Phys.*, 138(7):074506, 2013.

[247] Jared D Smith, Christopher D Cappa, Kevin R Wilson, Benjamin M Messer, Ronald C Cohen, and Richard J Saykally. Energetics of hydrogen bond network rearrangements in liquid water. *Science*, 306(5697):851–853, 2004.

[248] Jared D Smith, Richard J Saykally, and Phillip L Geissler. The effects of dissolved halide anions on hydrogen bonding in liquid water. *J. Am. Chem. Soc.*, 129(45):13847–13856, 2007.

[249] Alan K Soper and Kristian Weckström. Ion solvation and water structure in potassium halide aqueous solutions. *Biophysical chemistry*, 124(3):180–191, 2006.

[250] Hubert Staudigel and Stanley R Hart. Alteration of basaltic glass: Mechanisms and significance for the oceanic crust-seawater budget. *Geochimica et Cosmochimica Acta*, 47(3):337–350, 1983.

[251] RM Sternheimer. Electronic polarizabilities of ions from the hartree-fock wave functions. *Physical Review*, 96(4):951, 1954.

[252] Frank H Stillinger and Aneesur Rahman. Improved simulation of liquid water by molecular dynamics. *J. Chem. Phys.*, 60(4):1545–1557, 1974.

[253] Guillaume Stirnemann, Erik Wernersson, Pavel Jungwirth, and Damien Laage. Mechanisms of acceleration and retardation of water dynamics by ions. *J. Am. Chem. Soc.*, 135(32):11824–11831, 2013.

[254] Alberto Striolo, Angelos Michaelides, and Laurent Joly. The carbon-water interface: modeling challenges and opportunities for the water-energy nexus. *Annual review of chemical and biomolecular engineering*, 7:533–556, 2016.

[255] Emiko Sugimura, Tetsuya Komabayashi, Kenji Ohta, Kei Hirose, Yasuo Ohishi, and Leonid S Dubrovinsky. Experimental evidence of superionic conduction in H2O ice. *J. Chem. Phys.*, 137(19):194505, 2012.

[256] Chang Q Sun and Yi Sun. The attribute of water. *Springer Series in Chemical Physics*, 13:365–368, 2016.

[257] Jianwei Sun, Adrienn Ruzsinszky, and John P Perdew. Strongly constrained and appropriately normed semilocal density functional. *Phys. Rev. Lett.*, 115(3):036402, 2015.

[258] SS Sun and WF McDonough. The composition of the earth. *Chemical Geology*, 120(3-4):223–253, 1995.

[259] Dimitri A Sverjensky. Thermodynamic modelling of fluids from surficial to mantle conditions. *Journal of the Geological Society*, 176(2):348–374, 2019.

[260] Daisuke Takaiwa, Itaru Hatano, Kenichiro Koga, and Hideki Tanaka. Phase diagram of water in carbon nanotubes. *Proc. Natl. Acad. Sci. U.S.A.*, 105(1):39–43, 2008.

[261] Y. Takii, K. Koga, and H. Tanaka. A plastic phase of water from computer simulation. *J. Chem. Phys.*, 128:204501, 2008.

[262] Jianmin Tao, John P Perdew, Viktor N Staroverov, and Gustavo E Scuseria. Climbing the density functional ladder: Nonempirical meta–generalized gradient approximation designed for molecules and solids. *Phys. Rev. Lett.*, 91(14):146401, 2003.

[263] Susan Taylor, J Delaney, P Ma, GF Herzog, C Engrand, et al. Isotopic fractionation of iron, potassium, and oxygen in stony cosmic spherules: Implications for heating histories and sources. *Geochimica et Cosmochimica Acta*, 69(10):2647–2662, 2005.

[264] M. Thamer, L. De Marco, K. Ramasesha, A. Mandal, and A. Tokmakoff. Ultrafast 2d ir spectroscopy of the excess proton in liquid water. *Science.*, 350:78, 2015.

[265] M. Thomas, M. Brehm, R. Fligg, P. Vohringer, and B. Kirschner. Computing vibrational spectra from ab initio molecular dynamics. *Phys. Chem. Chem. Phys.*, 15:6608, 2013.

[266] Michael Thomas and Ben Corry. A computational assessment of the permeability and salt rejection of carbon nanotube membranes and their application to water desalination. *Philosophical Transactions of the Royal Society A: Mathematical, Physical and Engineering Sciences*, 374(2060):20150020, 2016.

[267] KJ Tielrooij, N Garcia-Araez, M Bonn, and HJ Bakker. Cooperativity in ion hydration. *Science*, 328(5981):1006–1009, 2010.

[268] Alexandre Tkatchenko and Matthias Scheffler. Accurate molecular van der waals interactions from ground-state electron density and free-atom reference data. *Phys. Rev. Lett.*, 102(7):073005, 2009.

[269] Takashi Tokushima, Yoshihisa Harada, Osamu Takahashi, Yasunori Senba, Haruhiko Ohashi, Lars GM Pettersson, Anders Nilsson, and Shik Shin. High resolution x-ray emission spectroscopy of liquid water: The observation of two structural motifs. *Chemical Physics Letters*, 460(4-6):387–400, 2008.

[270] Hajime Torii. Extended dipole-induced dipole mechanism for generating raman and optical kerr effect intensities of low-frequency dynamics in liquids. *Chemical physics letters*, 353(5-6):431–438, 2002.

[271] O. Tschauner, S. Huang, E. Greenberg, V. Prakapenka, C. Ma, G. Rossman, A. Shen, D. Zhang, M. Newville, A. Lanzirotti, and K. Tait. Ice-vii inclusions in diamonds: Evidence for aqueous fluid in earth's deep mantle. *Science*, 359:1136–1139, 2018.

[272] Harold C Urey. The thermodynamic properties of isotopic substances. *Journal of the Chemical Society (Resumed)*, pages 562–581, 1947.

[273] D. Vanderbilt. Optimally smooth norm-conserving pseudopotentials. *Phys. Rev. B. Condens. Matter*, 32:8412, 1979.

[274] Loup Verlet. Computer "experiments" on classical fluids. i. thermodynamical properties of lennard-jones molecules. *Physical review*, 159(1):98, 1967.

[275] Q. Wan, L. Spanu, G. Galli, and F. Gygi. Raman spectra of liquid water from ab initio molecular dynamics: Vibrational signatures of charge fluctuations in the hydrogen bond network. *J. Chem. Theory. Comput.*, 9:4124, 2013.

[276] Kun Wang and Stein B Jacobsen. An estimate of the bulk silicate earth potassium isotopic composition based on mc-icpms measurements of basalts. *Geochimica et Cosmochimica Acta*, 178:223–232, 2016.

[277] Kun Wang and Stein B Jacobsen. Potassium isotopic evidence for a high-energy giant impact origin of the moon. *Nature*, 538(7626):487–490, 2016.

[278] Lu Wang, Jijun Zhao, Fengyu Li, Haiping Fang, and Jian Ping Lu. First-principles study of water chains encapsulated in single-walled carbon nanotube. *J. Phys. Chem. C*, 113(14):5368–5375, 2009.

[279] Wenzhong Wang, Chen Zhou, Yun Liu, Zhongqing Wu, and Fang Huang. Equilibrium mg isotope fractionation among aqueous Mg2+, carbonates, brucite and lizardite: Insights from first-principles molecular dynamics simulations. *Geochimica et Cosmochimica Acta*, 250:117–129, 2019.

[280] G. H. Wannier. The structure of electronic excitation levels in insulating crystals. *Phys. Rev.*, 52:191–197, 1937.

[281] K Hans Wedepohl. The composition of the continental crust. *Geochimica et cosmochimica Acta*, 59(7):1217–1232, 1995.

[282] Ph Wernet, D Nordlund, Uwe Bergmann, M Cavalleri, M Odelius, H Ogasawara, Lars-Åke Näslund, TK Hirsch, Lars Ojamäe, P Glatzel, et al. The structure of the first coordination shell in liquid water. *Science*, 304(5673):995–999, 2004.

[283] Jody A White, Eric Schwegler, Giulia Galli, and François Gygi. The solvation of Na+ in water: First-principles simulations. *J. Chem. Phys.*, 113(11):4668–4673, 2000.

[284] Collin D Wick, I-Feng W Kuo, Christopher J Mundy, and Liem X Dang. The effect of polarizability for understanding the molecular structure of aqueous interfaces. *J. Chem. Theor. Comput.*, 3(6):2002–2010, 2007.

[285] C. Wu, L. Fried, L. Yang, N. Goldman, and S. Bastea. Catalytic behaviour of dense hot water. *Nat. Chem.*, 1:57, 2009.

[286] Y. Yoshimura, S. Stewart, M. Somayazulu, H. Mao, and R. Hemley. Convergent raman features in high density amorphous ice, ice vii, and ice viii under pressure. *J. Phys. Chem. B.*, 115:3756, 2011.

[287] T. Yoshino and T. Katsura. Electrical conductivity of mantle minerals: Role of water in conductivity anomalies. *Annu. Rev. Earth Planet. Sci.*, 41:605, 2013.

[288] Hao Zeng, Viktor F Rozsa, Nicole Xike Nie, Zhe Zhang, Tuan Anh Pham, Giulia Galli, and Nicolas Dauphas. Ab initio calculation of equilibrium isotopic fractionations of potassium and rubidium in minerals and water. *ACS Earth and Space Chemistry*, 3(11):2601–2612, 2019.

[289] Cui Zhang, Francois Gygi, and Giulia Galli. Strongly anisotropic dielectric relaxation of water at the nanoscale. *J. Phys. Chem. Lett.*, 4(15):2477–2481, 2013.

[290] Cui Zhang, Tuan Anh Pham, François Gygi, and Giulia Galli. Communication: Electronic structure of the solvated chloride anion from first principles molecular dynamics, 2013.

[291] Cunzhi Zhang, Federico Giberti, Emre Sevgen, Juan J de Pablo, Francois Gygi, and Giulia Galli. Dissociation of salts in water under pressure. *Nature communications*, 11(1):1–9, 2020.

[292] Haochen Zhu, Aziz Ghoufi, Anthony Szymczyk, Béatrice Balannec, and Denis Morineau. Anomalous dielectric behavior of nanoconfined electrolytic solutions. *Phys. Rev. Lett.*, 109(10):107801, 2012.